

AN ABSTRACT OF THE DISSERTATION OF

Joshua A. Robinson for the degree of Doctor of Philosophy in Nuclear Engineering
Presented on July 13, 2012.

Title: Design, Construction, and Characterization of a Neutron Depth Profiling Facility at the Oregon State University TRIGA® Reactor with an Advanced Digital Spectroscopy System

Abstract approved:

Jack F. Higginbotham

In this work, Neutron Depth Profiling (NDP) analysis capability has been added to the Oregon State University TRIGA® Reactor Prompt Gamma Neutron Activation Analysis Facility (PGNAA). This system has been implemented with an advanced digital spectroscopy system and is capable of rise time pulse shape analysis as well as coincidence measurements from multiple detectors. The digital spectroscopy system utilizes a high-speed multichannel digitizer with speeds up to 200 Megasamples/second (MS/s) with advanced hardware trigger and time stamping capabilities. These additions allow the facility to conduct simultaneous NDP and PGNAA combined measurements, which also enables cross calibration. The digital pulse processing is implemented with software programmed rise time pulse shape analysis capabilities for the analysis of the detector responses on a pulse-by-pulse basis to distinguish between different interactions in the detector. The advanced trigger capabilities of the digitizer were configured to accurately measure and correct for dead time effects from pulse pile up and preamplifier decay time.

©Copyright by Joshua A. Robinson
July 13, 2012
All Rights Reserved

Design, Construction, and Characterization of a Neutron Depth Profiling Facility at
the Oregon State University TRIGA® Reactor with an Advanced Digital Spectroscopy
System

by
Joshua A. Robinson

A DISSERTATION

Submitted to
Oregon State University

in partial fulfillment of
the requirements for the
degree of

Doctor of Philosophy

Presented July 13, 2012
Commencement June 2013

Doctor of Philosophy dissertation of Joshua A. Robinson
presented on July 13, 2012.

APPROVED:

Major Professor, representing Nuclear Engineering

Head of the Department of Nuclear Engineering and Radiation Health Physics

Dean of the Graduate School

I understand that my dissertation will become part of the permanent collection of Oregon State University libraries. My signature below authorizes release of my dissertation to any reader upon request.

Joshua A. Robinson, Author

ACKNOWLEDGMENTS

First, I thank Dr. Higginbotham for advising and working with me on this project. It has been a privilege to work under his direction. His insight and expertise in radiation spectroscopy has been of great assistance. In addition, Dr. Higginbotham made extraordinary personal, professional, and economic sacrifices. Without these sacrifices, I would not have been able to complete this research. Dr. Higginbotham's honesty, integrity, and willingness to risk his career standing against wrongs perpetrated by other faculty members is truly commendable. I would also like to thank the thousands of other supporters who stood behind Dr. Higginbotham.

I thank Dr. Hartman, my mentor on this project, for his advice and help in the design and construction of the facility; Manfred Dittrich for his assistance and encouragement in the machine shop; and the reactor operators for working with us and providing the necessary reactor time to make improvements and characterization of the facility.

I thank Dr. Downing for his support and assistance with the development of the Neutron Depth Profiling instrument as well as providing samples, detectors, and equipment needed for this project.

I also am very thankful for my wife, Fama, who has cared for our four small children (Joseph, Jonathan, Daniel, and Caleb) and encouraged me while I have been working on this project.

Lastly I thank my Dad, and my brothers and sisters (Zachary, Noah, Arynne, Bethany, and Matthew) for their support and encouragement.

TABLE OF CONTENTS

	<u>Page</u>
1. Introduction.....	1
2. Neutron Depth Profiling Review.....	8
3. Prompt Gamma Neutron Activation Analysis.....	16
4. Facility Description.....	18
4.1 Reactor and Beam Port #4.....	18
4.2 Prompt Gamma Neutron Activation Analysis Facility (PGNAA).....	22
4.3 Neutron Depth Profiling Components	28
4.4 Preamplifiers.....	31
5. Signal Processing.....	38
5.1 ORTEC DSPEC Pro.....	41
5.2 High Speed Digitizer for Digital Data Acquisition.....	43
5.3 Pulse Shape Discrimination	51
5.4 Digital Signal Processing	54
5.4.1 Pulse Acquisition	59
5.4.2 Pulse Amplitude Measurements.	61
5.4.3 Rise Time Measurements with Wavelet De-noising	65
5.4.4 Dead Time Correction	76
6. Results and Data Analysis	82

TABLE OF CONTENTS (Continued)

	<u>Page</u>
6.1 Energy Calibration	82
6.2 NDP-PGNAA Measurements	88
6.3 Rise-Time Analysis	93
6.4 Coincidence Measurements with LiF Film	106
6.5 NDP Analysis With Wavelet Smoothing	111
7. Additional Facility Modifications	113
PGNAA Fast Shutter System	113
8. Conclusions and Future Work	116
9. Appendix.....	120
9.1 Data Acquisition Code for GaGe Digitizer	120
9.2 Dead-Time Measurement Function.....	132
9.2 Rise-Time Measurement Function	133
9.3 Peak Amplitude Measurement Function	135
9.4 Haar Wavelet De-noising Code Generated with Matlab Wavelet Package	136
10. Bibliography	142

LIST OF FIGURES

<u>Figure</u>	<u>Page</u>
Figure 1: Horizontal section of the OSTR	19
Figure 2: HEU core configuration.....	20
Figure 3: LEU core configuration	21
Figure 4: Schematic illustration of PGNAA facility.....	22
Figure 5: Cross sectional illustration of PGAA collimator with internal components	23
Figure 6: Beam profile at sample location, reactor power 10 kW	25
Figure 7: Radiograph beam profile at sample location, reactor power 10 kW and shutter opened for approximately 25 seconds.....	25
Figure 8: PGNAA/NDP Facility	26
Figure 9: PGNAA/NDP Facility	27
Figure 10: NDP ultralow vacuum system	29
Figure 11: Preamplifiers used for NDP charged particle spectroscopy	35
Figure 12: NDP Cremat preamplifier configuration	35
Figure 13: Pu-239 spectrum (Preamplifier comparison).....	36
Figure 14: Preamplifier pulse comparison	37
Figure 15: Basic components of a standard analog radiation detection system.....	38
Figure 16: Basic components of a digital radiation detection system.....	39
Figure 17: ATS9462 digitizer board	47
Figure 18: GaGe Razor Compuscope CS1622 digitizer board	49
Figure 19: FEMPTO (DHPVA-200) Voltage-Amplifier.....	54
Figure 20: Digitized pulse for a single alpha interaction from the NDP surface barrier detector (Data taken with GaGe digitizer).....	59

LIST OF FIGURES (Continued)

<u>Figure</u>	<u>Page</u>
Figure 21: Trapezoidal filter. The filter generates a trapezoidal shape with a height that matches the step change in the data, and filters out random fluctuations.....	62
Figure 22: Example of pileup events separated using a trapezoidal filter.	63
Figure 23: De-noised digitized pulse using polynomials.....	66
Figure 24: Data smoothing with cubic splines	67
Figure 25: Graphical depiction of wavelet transform. Red arrows denote a subtraction, while blue arrows denote an addition.....	71
Figure 26: De-noised digitized pulse using level 8 Haar Wavelets with hard thresholds optimized to remove random noise.....	73
Figure 27: Rise time measurement.....	75
Figure 28: Dead time verification using Pu check source (Real time was 400 s)	79
Figure 29: Dead time verification using boron implanted silicon wafer (Real time was 400 s).....	81
Figure 30: Energy distribution for a single charged particle energy emitted uniformly throughout a thick sample.....	84
Figure 31: NIST Reference Standard 93a NDP spectrum taken with the OSTR NDP Facility (Real time 10800 s).....	85
Figure 32: Approximated derivative of wavelet smoothed data from Figure 31	86
Figure 33: NDP energy calibration obtained from NIST 93a reference standard.....	86
Figure 34: PGNAA boron standard calibration	89
Figure 35: Helium in silicon stopping power data (calculated with SRIM 2012)....	90
Figure 36: Boron implanted silicon NDP measurement. Measurement was performed at the NIST NDP facility and the OSTR NDP/PGNAA facility.....	91
Figure 37: Rise time measurements from Pu source for detector TP-50-50-15-NH operating at 35 V, 100 measurements were taken for each side of detector.....	94

LIST OF FIGURES (Continued)

<u>Figure</u>	<u>Page</u>
Figure 38: Pulse rise time measurement for surface barrier detector. This data was taken with Ra source facing the front side of the detector and Am source facing the back side of the detector.....	96
Figure 39: Pulse height histogram for surface barrier detector with rise time discrimination. This data was taken with Ra source facing the front side of the detector and Am source facing the back side of the detector.....	97
Figure 40: Rise time measurements for boron implanted silicon wafer with surface barrier detector TP-50-50-15-NH.....	98
Figure 41: Rise times discrimination of boron implanted silicon wafer with surface barrier detector TP-50-50-15-NH.....	99
Figure 42: Pulse rise time measurements of boron implanted silicon with detector .	101
Figure 43: Rise time discrimination of boron implanted silicon energy spectrum with detector FD 50-14-300 RG.....	102
Figure 44: Pulse rise time discrimination of boron implanted silicon energy spectrum with.....	102
Figure 45: Rise time measurements of LiF film with detector FD 50-14-300 RG....	103
Figure 46: Rise time discrimination of LiF film energy spectrum with detector.....	103
Figure 47: Comparison of OSTR NDP facility with PIPS detector to NIST NDP facility with surface barrier detector. Sample is boron a boron implanted silicon wafer.....	105
Figure 48: LiF film mounted in Teflon sample holder. Detectors are setup for coincidence NDP measurements.....	106
Figure 49: Raw spectrum from channel 1 and channel 2 with detectors on opposite sides of LiF film with the trigger set to channel 1.....	107
Figure 50: Coincidence measurements of LiF film. Energy level discriminator on channel 1 was set to accept only the pulse from detector channel 2 if the energy was within the triton peak.....	108

LIST OF FIGURES (Continued)

<u>Figure</u>	<u>Page</u>
Figure 51: Coincidence measurements of LiF film. Energy level discriminator on channel 1 was set to accept only the pulse from detector channel 2 if the energy was within the alpha peak.....	109
Figure 52: Helium in LiF stopping power data (Calculated with SRIM 2012)	110
Figure 53: NDP measurement of LiF film thickness6	110
Figure 54: Wavelet de-noising applied to NDP spectroscopy. The wavelet de-noised data collected with the OSTR NDP facility is compared to a spectrum of the same sample analyzed with the NIST NDP facility.....	111
Figure 55: PGNAA Facility with sample chamber shutter beam tube.....	114
Figure 56: PGNAA Facility with sample chamber shutter beam tube replaced with aluminum-thin-window to accommodate the Fast Shutter for PNNL experiments..	114
Figure 57: PGNAA/NDP Fast shutter system shutter open and close transit time ...	115
Figure 58: PGNAA Fast Shutter (Designed for PNNL experiments).....	115

LIST OF TABLES

<u>Table</u>	<u>Page</u>
Table 1: NDP Surface Barrier Detector Specifications.....	29
Table 2: NDP Preamplifier Specifications	34
Table 3: NDP Suggested Resistor Values	35
Table 4: Voltage Amplifier Operating Specifications	55

1. Introduction

To expand the experimental capabilities of the Prompt Gamma Neutron Activation Analysis (PGNAA) facility at the Oregon State University TRIGA® Reactor, Neutron Depth Profiling (NDP) with an advanced digitizer based digital spectroscopy system and pulse shape analysis capabilities has been added. This new NDP capability is integral to the previously existing PGNAA facility. As a result both systems utilize the same beam and sample location, allowing both analyses to be performed simultaneously on the same sample. The thermal neutron beam intensity for this facility is $2.81 \times 10^7 \pm 5.13 \times 10^5 \text{ cm}^{-2}\text{s}^{-1}$.

NDP is a near-surface nondestructive technique used for the analysis of depth profiles of specific light isotopes. NDP is based on charged particles that are emitted from thermal neutron absorption by specific isotopes. There are only a few isotopes that can be measured using neutron depth profiling, including $^{10}_5\text{B}$ and $^{6}_3\text{Li}$, which are of interest for semiconductor materials and lithium ion batteries. NDP was pioneered by Ziegler et al. [1] for the analysis of boron. Since then, neutron depth has been used extensively, particularly for the measurement of boron distribution in semiconductor materials [2]. Boron is of importance because of its effect on the electronic properties of semiconductors. However, in recent years NDP has gained new interest in the analysis of lithium, mainly for the analysis of and characterization of lithium ion battery materials [3-5].

Lithium ion batteries have a much higher storage capacity and energy output than conventional battery types such as lead acid or nickel cadmium. They also can withstand up to several thousand charging cycles, depending on the anode and cathode materials. The life-span of lithium ion battery types is dependent on the material composition and structure of the battery cathode and anode. Because of the nondestructive nature of NDP it is ideal for better understanding the processes that lead to aging of lithium ion batteries. It is also useful in other areas of materials research involving charged-particle emitting isotopes.

Since NDP will likely play a significant role in the development of lithium ion batteries and materials development, this facility has been designed with these applications in mind.

The unique features in this facility, which have not previously been extant in other NDP or PGNAA facilities, are its digital spectroscopy system and its capability to perform both NDP and PGNAA analysis simultaneously.

Depending on the type of sample, it may be necessary to perform a NDP analysis for the near surface regions of an isotope, as well as a PGNAA analysis to determine the total concentration of the isotope within the sample. This type of analysis could be valuable for diffusion experiments and experiments for which knowledge of a bulk sample composition is necessary in order to accurately calculate stopping powers for the NDP analysis. In addition, the capability of cross-calibrating the NDP spectroscopy system with the PGNAA spectroscopy system can decrease the

possibility of calibration error and provide a simple and accurate means to calibrate the NDP facility.

Current NDP facilities, such as the one at the National Institute of Standards and Technology (NIST), use surface barrier detectors to measure the energy of charged particles emitted from the sample to determine the depth profile of the isotope of interest. The signal output from the detector is analyzed through a standard analog detection system and multichannel analyzer to create a histogram of the measured energy distributions. This type of system has the restriction that it is difficult and often impossible to perform the necessary calculations of the detector response to obtain the necessary data.

For NDP, this is of interest because of possible differences in the detector response depending on particle interaction with the detector as well as coincident techniques that can be used to improve detection capabilities. For similar reasons, many data acquisition systems are shifting over to digital technology. Digital data acquisition has many advantages over analog systems, and modern digitizers have reached sufficient speed and resolution that they can often replace analog systems without sacrificing resolution. Also, due to the nature of the data processing for spectroscopy applications, they can handle considerably higher count rates with decreased system dead times.

For this work the digital signal processing capability has been implemented with a multichannel high-speed digitizer with trigger time-stamp capabilities and complex hardware trigger capabilities. The digitizer digitizes the output signal from the preamplifier and uses the hardware trigger system to detect and measure pulse decay

dead-time effects. Following each trigger event, the pulses are saved to the computer and processed with mathematical algorithms to extract the necessary data. This system proved able to conduct pulse height analysis as well as rise-time measurements on the data. The pulse height analysis is necessary in order to determine the energy deposition in the detector, and the rise-time analyses can be used to differentiate between particles of differing mass.

There is a high background count rate in the low-energy range of the spectra because of the nuclear and atomic interactions taking place during a NDP acquisition. This is primarily due to gamma and beta interactions within the detector. There are several methods by which this background can be reduced using digital signal processing. Probably the best of these methods are rise-time discrimination and coincident counting techniques.

Rise-time discrimination depends on the differences in surface barrier detector response based on the type of interacting particle. For heavy charged particles the time it takes for the electron-hole pairs created within the detector to move across the detector is slower than it is for the electron-hole pairs created by particles of lighter mass, such as from gamma or beta radiation. This is due to the so called “Plasma Effect.” The plasma effect is caused by a localized reduction in the potential across a reverse biased detector. This effect occurs because heavy charged particles deposit most of their energy over a very short range as opposed to gamma or beta radiation, in which energy is deposited over much longer ranges. In the case of heavy charged particles interacting in a semiconductor detector, this leads to a very high density of electron-hole pairs created in a localized region of the detector. Momentarily as the

electron-hole pairs start to move across the detector, the potential in this region is reduced, leading to longer collection times and therefore longer rise times in the detector response. Depending on the bias voltage of the detector and which side of the detector the particle enters from, the rise-time response can vary several fold depending on the type of interacting particle. Rise-time discrimination using analog systems has been implemented successfully with many improvements over the years [6], and has been shown to significantly reduce the background in the low-energy range while using PIN diode detectors for NDP [7]. However in NDP these techniques have not received much attention due to the restrictions and complexity of implementation using the available analog systems. In this work these rise-time measurements have been implemented with software programming and applied to the NDP system.

In addition to rise-time measurements, the multichannel digitizer is configured for coincidence measurements, which have been demonstrated with an ultra-thin sample of LiF.

For NDP this capability is valuable because gamma rays, which cause a considerable portion of the low energy background, pass through the detector and deposit only a small portion of their energy. Therefore, if a second detector is placed on the opposite side of the sample from the first detector and coincident events are measured, the majority of this background could be discarded as non-meaningful. On the other hand, for the case of neutron capture in ^6Li , an alpha particle and a triton are emitted from the nucleus.



The triton and the alpha particle have energies of 2,727 and 2,055 keV respectively, and are emitted at an angle of 180° to each other with no motion of their center of mass. Thus for thin samples, if detectors are placed on both sides of the sample, a coincident event will be observed, providing the particles are emitted within the solid angle of both detectors. Events without a coincidence in the opposite detector would be excluded. This would decrease background interference for the lithium measurement. Also, if the sample thickness is known, the energy of the emitted alpha particle, which corresponds to the distance traveled within the sample, should correspond to the energy of the triton traveling through the remainder of the sample. In other words, the distance traveled by the alpha particle plus the distance traveled by the triton should equal the sample thickness, providing the particles exit the sample normal to the sample surface. If the particles do not exit normal to the sample surface, the distance traveled by both particles will be greater than the sample thickness. The overall distance can then be used to calculate the angle at which the particles exited the sample, and from this the depth at which the interaction took place normal to the sample surface can be calculated. This also can increase the resolution, since the angle at which the particle exits the sample would be known; counting efficiency can also be increased by bringing the detector closer to the sample [8].

For most NDP applications the detectors were placed far enough from the sample so that the solid angle subtended by the sample at the detector was very small and therefore considered insignificant. With this system the coincident capabilities eliminate the need for this restriction.

Also, because of the time stamp capabilities, the time can be recorded for every detector pulse. This enables real-time measurement of changes in concentration. This capability can be used to monitor lithium migration while charging and discharging lithium ion batteries. These types of measurements have recently been successfully conducted with specially fabricated batteries that have very thin packing to allow for the escape of the charged particles [9]. These measurements are usually conducted by stopping and restarting the data acquisition repeatedly for a fixed amount of time while saving the data each time. The advantage of this digital spectroscopy system is that since the time is recorded for each pulse, the data can be discretized into any time scale of interest after the analysis on a pulse-by-pulse basis. This can greatly improve the value and accuracy of these types of measurements.

2. Neutron Depth Profiling Review

The measurement of isotope concentrations in substrates is important for the development and analysis of many materials. For example, the determination of boron concentration and distribution in semiconductor materials is important in advancing their development. Boron can be accurately measured with only a few analysis techniques. In the forefront of these techniques is Neutron Depth Profiling (NDP).

NDP was pioneered by Ziegler, Cole, and Baglin [1] for the study of boron diffusion in boron-implanted intrinsic silicon and arsenic-doped silicon. These early measurements were conducted at Brookhaven National Laboratory using the neutron source from the Brookhaven National Laboratory high flux reactor (HFBR) beam port H-1. This neutron beam had a flux of 2.3×10^8 neutrons $\text{cm}^{-2}\text{s}^{-1}$ and was mostly contained within the evacuated beam tubes in and around the sample chamber. (The Brookhaven reactor has since been decommissioned.[10])

The samples in this facility were oriented at a 45° angle to the incoming neutron beam, similar to that of current NDP facilities. This allows the detectors to face the sample without being placed in the path of the neutron beam. Semiconductor particle detectors were used to measure the energy of the charged particles emitted from the samples.

The method got its name Neutron Depth Profiling (NDP) from Greg Downing and Ronald Fleming during early developments of the method at the National Bureau of Standards (now known as the National Institute of Standards and Technology (NIST))

[11]. During this work they profiled boron, nitrogen, lithium, and helium. These measurements demonstrated the effectiveness of NDP for elemental profiles, film thickness measurements, diffusion experiments as well as many other applications. Since then NDP has been utilized successfully for many materials science applications in the United States at NIST as well as other facilities in the US such as University of Michigan, Texas A&M, University of Texas-Austin and North Carolina State University. NDP has also been implemented in many other countries such as France, Czech Republic, Canada, Germany, and Japan [12].

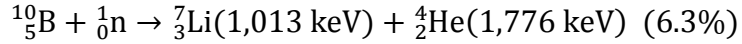
One of the most recent neutron beam facilities which was designed with NDP in mind has been built at Ohio State University [13]. This facility has a neutron flux of $(8.55 \pm 0.19) \times 10^6 \text{ cm}^{-2}\text{s}^{-1}$.

The NDP Technique is very similar to Rutherford Backscattering (RBS) in that both methods are based on measuring the energy loss of charged particles in materials [14]. The difference is that NDP relies on charged particles emitted from neutron absorption by the isotopes of interest, and RBS relies on charged particles scattering off the sample from an external charged particle source. Even though RBS is capable of measuring a much wider range of elements, it has poor resolution for light elements due to the physics of charged particles scattering of light elements such as boron and lithium, both of which can be measured with excellent resolution with NDP.

The interaction process for NDP is neutron absorption. When a nucleus absorbs a neutron, a compound nucleus is formed, with excitation energy equal to the kinetic energy of the incoming neutron plus the binding energy of the neutron. The compound

nucleus decays almost instantaneously (~ 10 fs) and emits decay radiation characteristic of the isotope and the reaction type.

For a few isotopes this radiation takes the form of charged particles, which are emitted at discrete energies, the kinetic energy of the absorbed neutron contributing very little to the reaction. One example is neutron capture by $^{10}_5\text{B}$ in which a α particle and a ^7_3Li ion are emitted. For this reaction the particles have two possible energies since the ^7_3Li can be formed in either the excited state or the ground state. The equations for this reaction are listed below.



The range of these particles within the materials is generally 5-10 microns, depending on the energy and type of the emitted particles and the stopping power of the material. The energy of the emitted particles measured by the detector is strongly dependent on the depth at which the reaction takes place. For a NDP analysis, if the emitted particle starts at a depth of x within a sample and is emitted at an angle θ to the surface normal to the sample, distance d traveled through the sample and the distance x to the surface of the sample are related to the angle θ by Equation 3.1.

$$\frac{x}{d} = \cos \theta \quad (3.1)$$

The energy of the particle after traveling a distance d is directly proportional to the stopping power of the material. This is shown by Equation 3.2.

$$E_o - E_f = d S(E_o - E_f) \quad (3.2)$$

E_o and E_f are the initial and final energies of the emitted particles, and $S(E_o - E_f)$ is the stopping power of the material for an energy loss of $E_o - E_f$. Therefore the emitted energy of a particle will be related to the depth at which it was produced as shown in Equation 3.3.

$$x = \cos \theta \frac{(E_o - E_f)}{S(E_o - E_f)} \quad (3.3)$$

Since the stopping power is related to the energy of the particle, this equation becomes

$$x = \cos \theta \int_{E_f}^{E_o} S(E) dE \quad (3.4)$$

Knowing the correct stopping power as a function of energy for the substrate material is essential in the calculation of the depth profile. These stopping power functions can be determined from first principles as well as experimentally. The main components that contribute to the stopping power of charged particles are the projectile particles (charged particles) and the target atoms (and/or compounds). The stopping power is generally broken down into two categories: the electron stopping power and the nuclear stopping power. A detailed analysis of the nuclear and electron cross sections for ions can be found in “The Stopping and Ranges of Ions in Matter” [15]. These cross-sections are calculated for individual elements.

The individual element cross sections can be combined for compounds using Bragg’s Rule, which states that the stopping power of compounds is approximately

equal to a linear combination of the elements in the compound [16]. This approximation ignores the effect of the orbital and excitation structure, which may be different for the individual elemental materials and the same elemental materials in the form of a compound.

For the case of carbon, the bonding structure can affect the stopping power by as much as an order of magnitude. Both et al. [17] concluded that this effect was due to the confinement of the electron distribution of the individual molecules to a finite volume and developed a method based on the chemical bonding to make a correction to the stopping power. This correction is referred to as the Core and Bond (CAB) and it divides each target atom into two parts, the electrons which are unaffected by the bonding and the bonding electrons. Based on experimental data and by analyzing the stopping power of many different materials, the contributions to the cores and the bonds are then determined.

All the necessary stopping powers used in NDP can be obtained through the Stopping and Range of Ions in Matter (SRIM) program developed by Ziegler, which calculates the stopping power of ions in matter [18]. SRIM uses Bragg's rule along with the Core and Bond approach to correct for the stopping power of ions in compounds consisting of light elements; for compounds made of heavy elements the compound structure effect is insignificant and there is no significant deviation from Bragg's Rule.

The charged particle and bulk material composition are input into SRIM, which produces discretized range tables of energy loss as a function of distance. Thus, if the

bulk composition of the sample and the energy of the charged particles emitted during a NDP measurement are both known, the concentration as a function of depth for the isotope of interest can be calculated.

There are many factors that limit the resolution and sensitivity of an NDP analysis. These include both electronic and hardware limitations in addition to limitations due to the physics of the NDP analysis.

The detectors and signal processing chain can lead to considerable noise in the output signal from the detector response. For NDP, some of the most common sources of noise are feedback from ground loops, excessive detector leakage currents, and induced noise from other equipment such as the turbo vacuum pump.

Ground loops, which can cause considerable annoyance in setting up the system, can be eliminated by making sure all the components of the facility are solidly connected to a common ground.

Excessive leakage currents are generally only a problem with older detectors that have been subjected to long periods of high-intensity radiation bombardment, and replacement of the detector will often eliminate them. However, for some cases in which a detailed analysis of the detector response characteristics is performed, such as pulse-shape analysis, lower detector leakage rates may be desirable. For these cases, cooling the detector will significantly reduce the leakage current and may be of some benefit [19].

Induced noise from the mechanical equipment, especially the turbo pump, is a common problem for NDP systems. This is because of the need to position the turbo

pump close to the chamber to achieve the desired vacuum levels. This problem is usually addressed by electrically separating the turbo pump from the sample chamber and is sufficient for most NDP analysis. However, a much better method, which has been implemented in this facility, involves placing the preamplifier inside the sample chamber. Since a majority of the noise introduced from the mechanical systems is introduced before the preamplifier and consequently is then amplified by the preamplifier, placing the preamplifier inside the sample vacuum chamber, which provides much better shielding, can significantly reduce this component of the noise.

Other contributing factors that limit resolution and sensitivity are caused by nuclear reactions taking place in and around the sample chamber. As has been shown [20], there are very high-intensity neutron and gamma fields produced during the irradiation. The neutrons are mostly due to scattering of beam neutrons off the sample, and the gamma rays are produced from the de-excitation energy of nuclei after excitation from neutron interactions.

For the PGNAA facility, a tradeoff was made in the counting efficiency versus the background radiation exposed to the detector. This was done by moving the detector away from the sample to allow for large amounts of gamma and neutron shielding to be placed around the detector. Unfortunately, with NDP, due to the intensity of the charged particles, moving the detectors very far from the sample leads to unacceptable losses in efficiency. This results in very high neutron and gamma fluxes incident on the detector.

Since the charged particle detectors used for NDP are very thin, full energy depositions within the detector are very unlikely and there is only partial energy transfer for neutrons and gammas incident on the detector. As a result, the energy transfer to the detector is typically very small, resulting in a low energy detector response. However, due to the intensity of the gamma and neutron fluxes incident on the detector, this generates a very high intensity, low energy background count rate. In NDP analysis of isotopes that require measurements of protons in the 500-600 keV range, three of which are $^{3}_{2}\text{He}$, $^{35}_{17}\text{Cl}$, and $^{14}_{7}\text{N}$, this interference results in a significant decrease in the resolution and sensitivity of measurements.

3. Prompt Gamma Neutron Activation Analysis

The mechanism for prompt gamma neutron activation is similar to NDP in that when a nucleus absorbs a neutron, a compound nucleus is formed with excitation energy equal to the binding energy (BE_n) of the neutron plus the kinetic energy of the neutron (K_n).

$$E_x = K_n + BE_n \quad (3.5)$$

For about 80% of the stable nuclei the binding energy ranges from 6-10 MeV. The excitation energy is rapidly shared among the nucleons followed by almost instantaneous decay ($\sim 10^{-13}$ to 10^{-14} s), with the following possible reactions.

- 1) Inelastic scattering in which the neutron is emitted along with one or more gammas.
- 2) Radiative capture (n,γ) in which one or more capture gammas are emitted.
- 3) Particle emission, e.g., (n,α) , (n,p) , (n,d) , ..., $(n,2n)$.
- 4) Fission, or if enough energy, spallation or evaporation [21].

Of the four processes, radiative capture is the most common form of decay for the compound nuclei formed by the absorption of a thermal neutron, and it is the fundamental process for PGNAA. Similar to atomic theory for the atoms, the nucleus has discrete energy levels. When the nucleus is in an excited state, the excitation energy is shared among several of the nucleons within the nucleus. These nucleons almost instantaneously go through a series of discrete energy transitions to relax back to the ground state. The high-energy transitions starting at the capture state are called

primary transitions, lower-energy transitions following the primary are called secondary transitions, and the final transitions reaching the ground state are called ground-state transitions. For each transition a gamma ray is released with energy equal to the energy of the transition (E_T) minus the recoil-energy (E_R) of the nucleus.

$$E_\gamma = E_T - E_R \quad (3.6)$$

For radiative capture the recoil energy can be as high as several keV for light elements, but is typically less than 0.1% of the transition energy for most elements [22]. Thus, as the nucleons return to the ground state, the energy released is discrete and characteristic of the nuclear energy levels within the nucleus. Since the energy levels of the nuclei are characteristically different for different elements, the gammas released from radiative capture, which range from 50 keV to greater than 10 MeV, are distinct for differing elements.

For PGNAA, it is important to consider radiative capture of both thermal neutrons and epithermal neutrons. For thermal neutrons, the energies of the capture states are very sharply defined due to low kinetic energy of the neutrons. Thus, the probability of decay through various transitions is essentially independent of neutron energy and hence also the distribution of the gammas produced. This is important for determining information such as quantities of elements through PGNAA.

For epithermal neutrons ($E \approx 1\text{eV}$ to 10 keV), the increased kinetic energy of the neutrons results in greater excitation energy of the compound nucleus. For these higher excited states the transition to the ground state tends to be less well-defined, often resulting in an increase or change in the number of different energy gammas released due to de-excitation through different discrete energy levels of the nucleus.

4. Facility Description

4.1 Reactor and Beam Port #4

The Oregon State University reactor is a natural convection cooled 1 MW (licensed 1.1-MW) TRIGA® pool reactor. Prior to August 2008, the reactor core was fueled with 70% enriched uranium/zirconium hydride fuel elements (HEU). In August 2008, the reactor was refueled with 20% enriched uranium/zirconium hydride fuel (LEU). The core of the reactor is surrounded by a 30 cm graphite reflector and is located near the bottom of a water-filled aluminum tank, 2 m in diameter and 6.25 m deep, which is shielded radially by over 2.5 m of concrete, 0.5 m of water, 5 cm of lead and 26 cm of graphite.

The reactor is equipped with four beam ports, which penetrate the reactor bioshield and reactor tank to the reflector region of the core. Beam ports #1 and #2 are radial beam ports, which terminate at the outer edge of the graphite reflector. Beam port #3 is tangential to the outer edge of the core and is dedicated to a neutron radiography facility. Beam port #4 is a radial piercing beam port, which penetrates through the graphite reflector and terminates at the outer edge of the reactor core as illustrated in Figure 1.

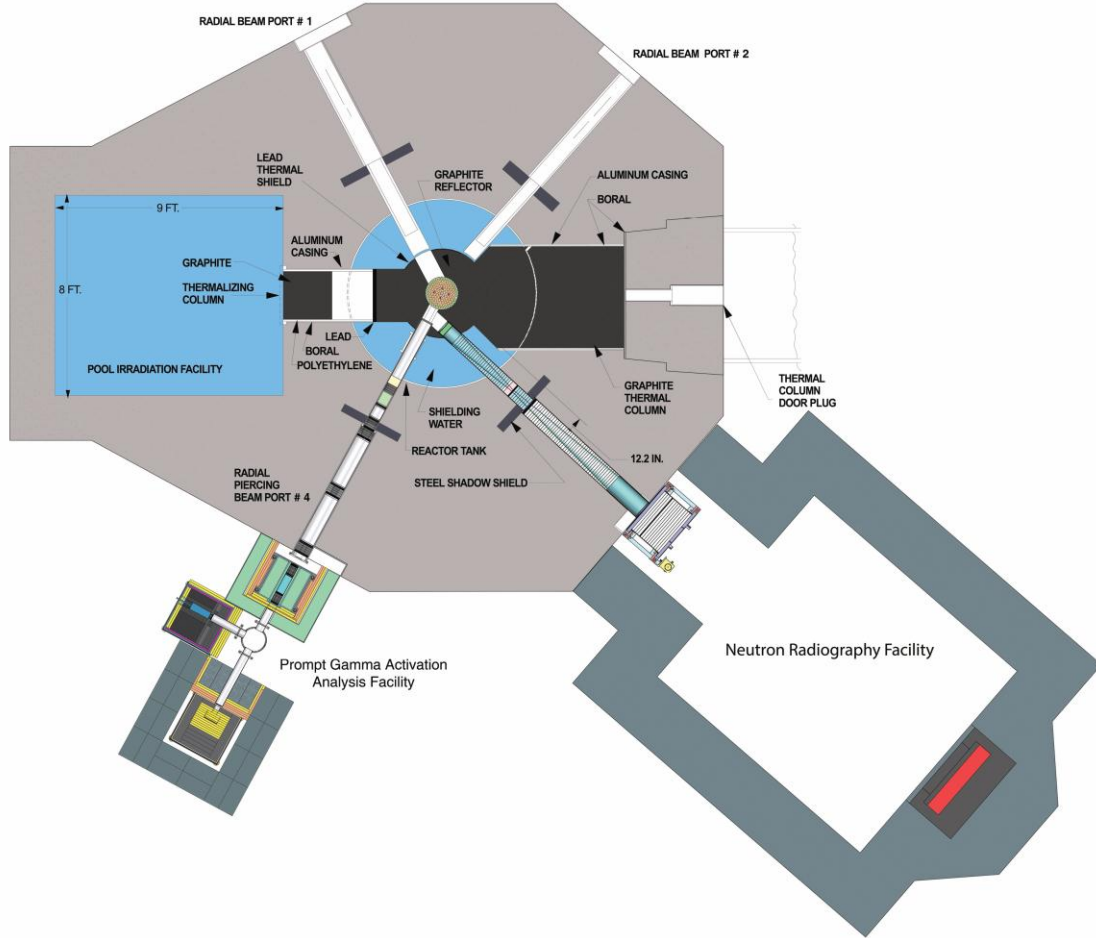


Figure 1: Horizontal section of the OSTR

Due to water leakage within the graphite reflector, beam ports #1 and #2 have a reduced flux, leaving beam port #4 as the only available beam port suitable for the PGNAA Facility. As described above, beam port #4 is a piercing beam port, which looks directly at the core. Beam port #4 is situated directly in front of element locations G-12 and G-13. Before the fuel change, these locations were occupied by fuel elements, as shown in Figure 2. However, during the fuel change these elements were replaced with graphite elements, as shown in Figure 3. The advantage of this beam port is that it has a very high thermal flux due to its proximity to the core.

However, since it is situated directly in front of the core it also has a very high fast neutron and gamma component streaming down the beam port as well. Thus, it was important to include appropriate beam filtering to minimize the fast neutrons and gammas while still maintaining a high thermal flux.

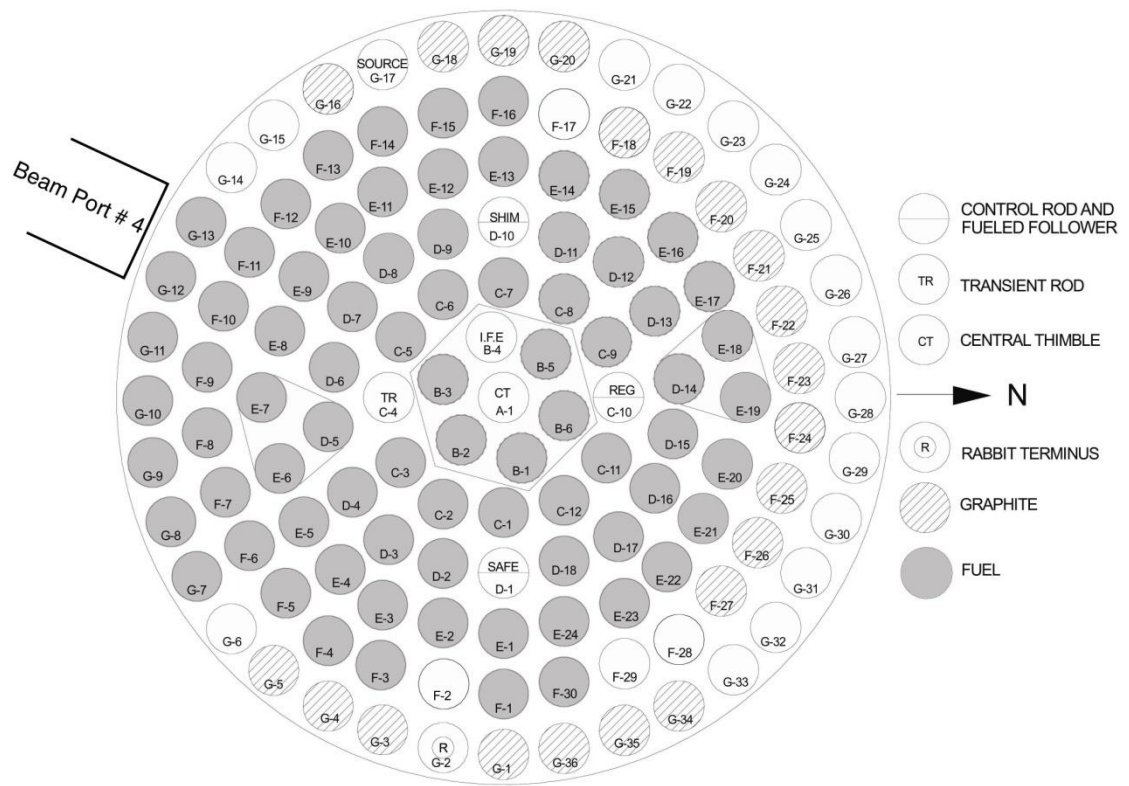


Figure 2: HEU core configuration

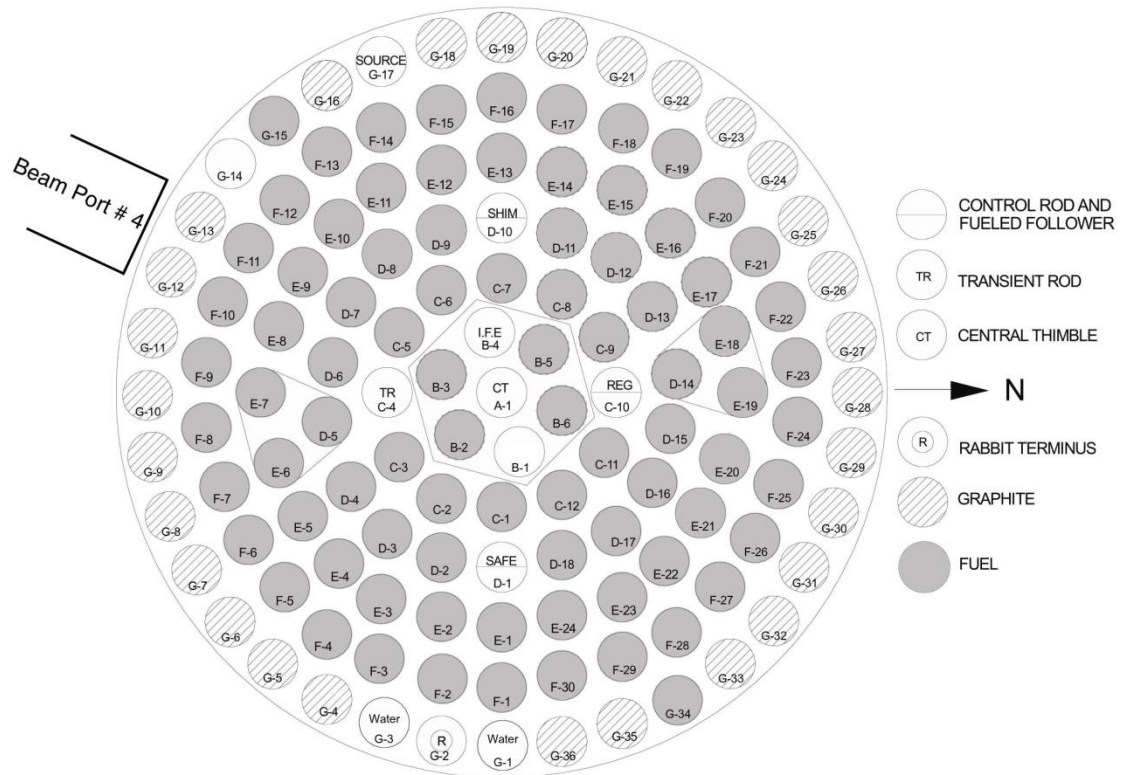


Figure 3: LEU core configuration

4.2 Prompt Gamma Neutron Activation Analysis Facility (PGNAA)

The Oregon State TRIGA Reactor Prompt Gamma Neutron Activation Analysis Facility was designed and built by Robinson and Hartman in 2009 [23]. It was designed with the eventual goal of adapting the facility to NDP experiments as well as PGNAA.

The main components of the OSTR PGNAA facility are the collimator, shutter, sample chamber, beam stop, high purity germanium detector and fixed biological shielding for the reduction of background radiation. A schematic illustration of these components is presented in Figure 4.

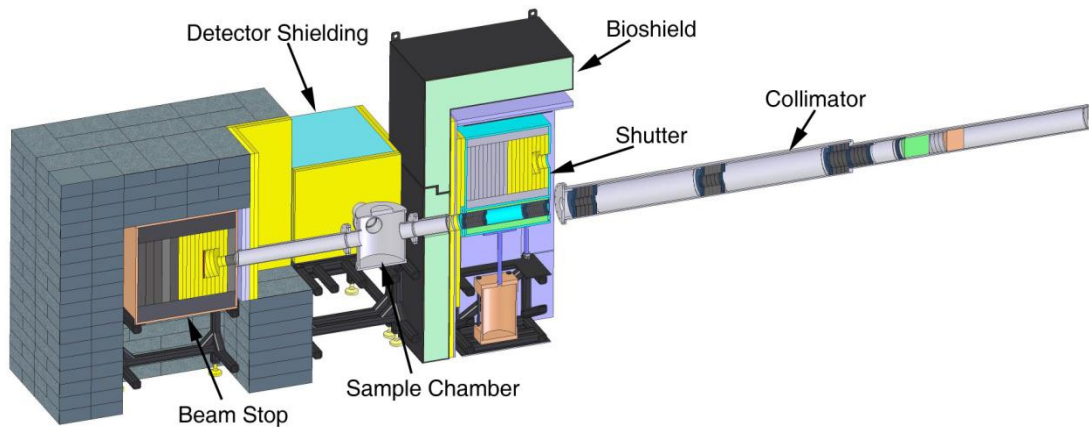


Figure 4: Schematic illustration of PGNAA facility

The collimator, which is installed in beam port #4 of the OSTR, serves to collimate the neutron beam to a diameter of 2 cm and reduce the fast neutron and gamma components. The collimator is contained within a welded aluminum tubing shell,

which is designed to slide into the beam port. Within this shell is a series of lead and boral rings to collimate the neutron beam streaming from the core of the reactor to the desired diameter at the sample location.

Further down the shell are bismuth and sapphire filters to reduce the gamma and fast neutron component of the beam. Aluminum thin-windows are placed on both ends of the collimator to allow it to be evacuated or backfilled with an inert gas such as helium. This reduces gamma production from neutron interactions with the constituents of air within the collimator, such as nitrogen, and therefore lowers background radiation levels in and around the facility. This increases the detector signal-to-noise ratio.

The aluminum thin-window on the reactor side is welded in place and the aluminum thin-window on the exit side is bolted on with an O-ring sealed flange, allowing easy access to the materials within the collimator. The internal components of the collimator are shown in Figure 5.

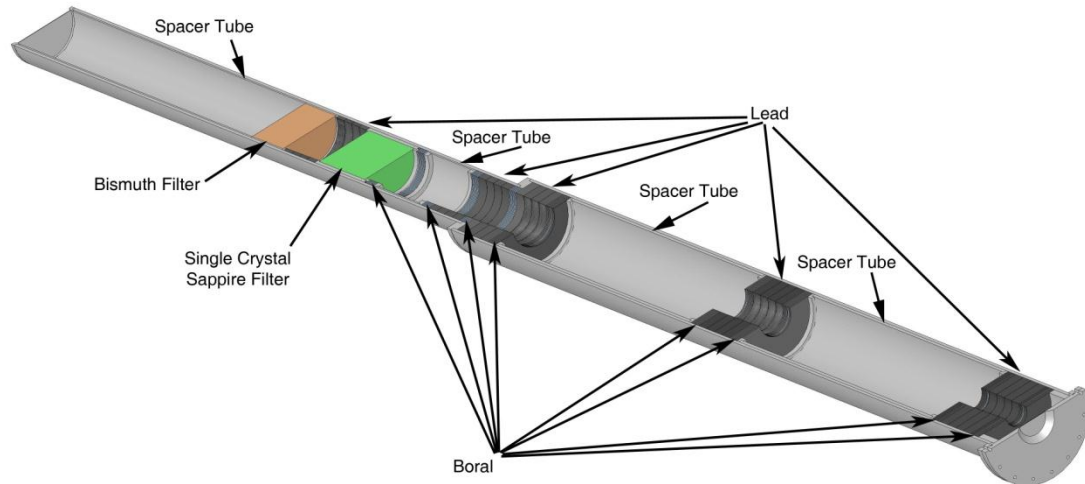


Figure 5: Cross sectional illustration of PGAA collimator with internal components

Following the collimator is a shutter and biological shield. The shutter consists of a large movable beam stop mounted on an air cylinder, which prevents the neutron beam from entering the sample chamber when samples are being loaded or when the facility is not in use. This shutter is equipped with several safety interlocks, which ensure safe operation of the facility. The shutter also has a beam flight tube incorporated into it, which aligns with the beam to add additional collimation when the shutter is open. This leads to a precisely collimated neutron beam with a minimal overall beam diameter outside the main focused portion of the beam; this is important for both PGNAA and NDP.

For PGNAA it is important to minimize neutron interactions within the support structure and electronics in the sample chamber; this minimizes prompt gamma emission that would lead to higher background interference. For NDP this is also important, but even more important is the ability to place the charged-particle detectors close to the sample without them interacting with the neutron beam. A radiograph image and a profile spectrum of the neutron beam at the sample location are presented in Figure 6 and 7.

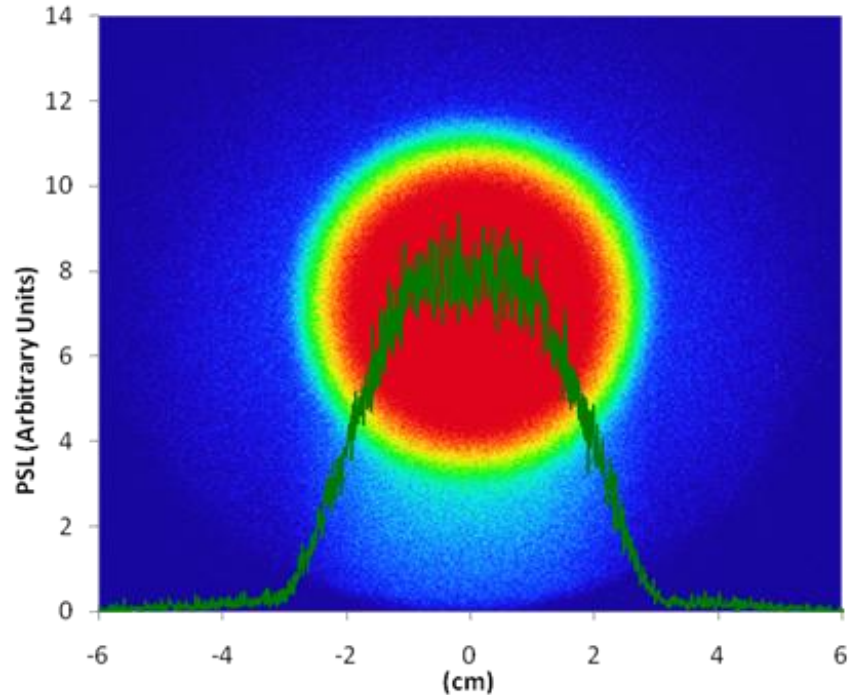


Figure 6: Beam profile at sample location, reactor power 10 kW

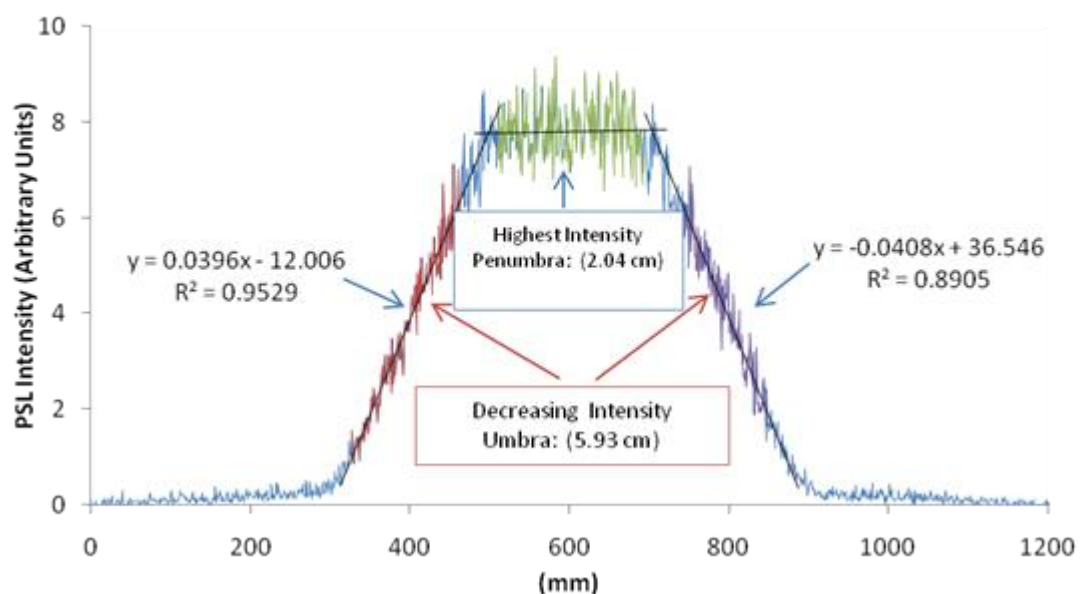


Figure 7: Radiograph beam profile at sample location, reactor power 10 kW and shutter opened for approximately 25 seconds

The sample chamber in the facility is made of aluminum and has a diameter of 30 cm and a depth of 33 cm. This provides sufficient room for the samples, a sample and detector rotation stage, and surface barrier detectors for NDP. The sample chamber is also designed to be evacuated or backfilled with helium.

The high-purity germanium detector is placed approximately 60 cm from and at a 90° angle to the beam. It is surrounded with a borated polyethylene and lead shield to protect it from radiation other than the capture photons released from the sample.

Following the sample chamber is the beam stop to capture the beam when the shutter is open. Photos of the facility are presented in Figures 8 and 9.



Figure 8: PGNAA/NDP Facility



Figure 9: PGNAA/NDP Facility

4.3 Neutron Depth Profiling Components

Since the NDP facility and PGNAA use the same irradiation facility, many of the components are integral to both. However, in order to accommodate NDP measurements many modifications had to be added to the facility. These additions included a low vacuum system, charged particle detectors, and the necessary supporting electronics and hardware.

The low vacuum system is necessary to reduce the concentration of air in the chamber to the point that there is not an appreciable decrease in the energy of the charged particles emitted by the sample before they reach the detector. This system consists of an Edwards XDS-5 roughing pump and an EXT75DX turbo pump, which provides vacuum levels in the range of 10^{-5} torr during operation. A control system is used to ramp up the turbo pump after appropriate vacuum levels have been achieved by the roughing pump. The control system was supplied by Edwards Vacuum, Inc. and includes the vacuum gauges and sensors to monitor the system. This system is necessary for preventing overloading and possible damage to the turbo pump during start up. The turbo vacuum system is shown in Figure 10.

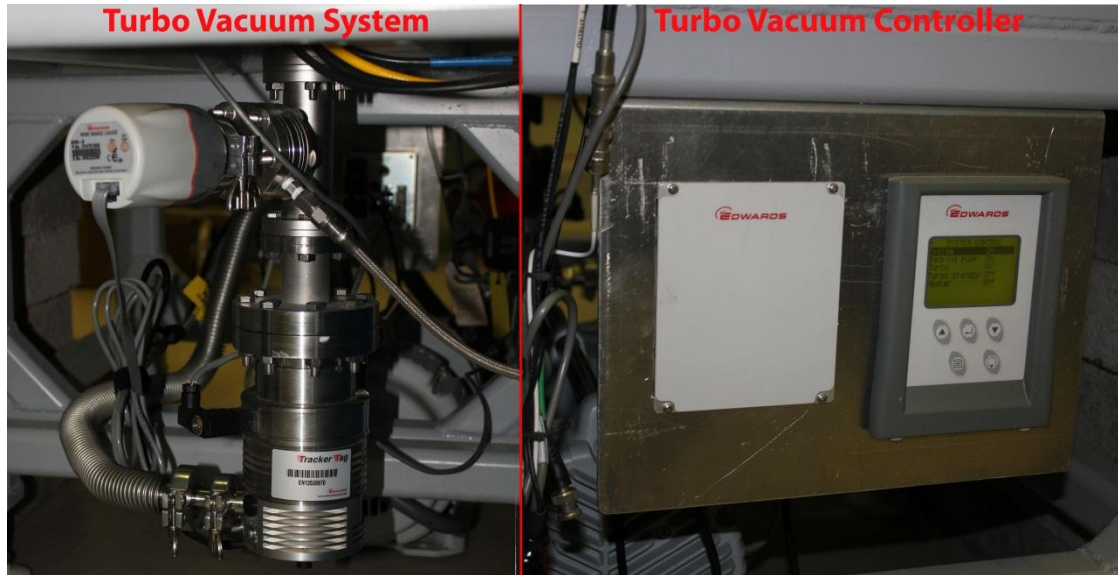


Figure 10: NDP ultralow vacuum system

The charged particle detectors implemented in the facility are surface barrier detectors fabricated by Advanced Measurement Technology, Inc. (AMETEK) and Tennelec (now a division of Canberra). The Tennelec detectors were provided by Greg Downing at the National Institute of Standards and Technology (NIST) for the initial characterization of the facility. These detectors are dedicated to the facility and provide a range of different operating characteristics. The active area of the detectors ranges from 50 to 150 mm², and they have depletion depths of approximately 50 to 100 μm at full operating potential. The detectors are listed in Table 1.

Table 1: NDP Surface Barrier Detector Specifications

Detector	Active Area [mm ²]	Sensitive Depth [microns]	Bias [V]	Alpha Resolution [keV] FWHM	Noise [keV] FWHM
AD-015-050-100	50	85.2	55	15	7.8
AD-025-150-100	150	87.9	110	17.8	12.6
TP-50-50-15-NH	50	57.3	35	NA	NA

For standard NDP measurements the smaller active area and minimum depletion depths are ideal for detectors that are relatively close to the sample. A smaller active area helps minimize the solid angle of the sample at the detector to reduce broadening of the spectrum, and a minimum depletion depth reduces the gamma and neutron interactions in the detector that contribute to low energy background.

There are two signal processing systems implemented on the NDP facility. Both signal processing systems rely on a Cermet CR-110 preamplifier installed on a CR-150 evaluation board.

The first signal processing system is a DSPEC Pro designed by ORTEC. This system is an excellent spectrometer for recording the energy dependent response from the detector.

The second signal processing system consists of a GaGe Express Razor CompuScope 16 bit 200 MS/s digitizer. For this system the signal from the output of the preamplifier is digitized with the high-speed digitizer and processed through software programming. This system provides advanced signal processing and data acquisition such as waveform pulse shape analysis and more advanced coincident counting capabilities, which are not available with the DSPEC Pro.

4.4 Preamplifiers

The preamplifiers used for the NDP charged-particle detection system are standard charge-sensitive preamplifiers. These charge-sensitive preamplifiers are used to collect the current flow from the detector and convert it to an amplified voltage signal, which is proportional to the current flow from the detector. For a reverse-biased surface barrier detector there is a small amount of leakage current flowing across the detector [19]. This small amount of leakage current can result in a steady DC offset in the output from the preamplifier as well as an increase in baseline noise.

When a charged particle deposits energy in a surface barrier detector it results in a burst of current flow across the detector. This current flow is due to the migration of the electron-hole pairs created when the particles deposit energy in the detector and is proportional to the energy deposited in the detector. Consequently there is an increase in voltage at the output of the preamplifier, which is proportional to the energy deposition within the detector. The rate of voltage increase is also proportional to the electron-hole pair collection time, which is determined by the electron-hole pair drift velocities as well as the location of interaction within the detector. Depending on the required response from the preamplifier, these characteristics are important considerations in determining the preamplifier that is best suited to the application.

The rise time, decay time, and noise characteristics were the main parameters used in selecting the preamplifier for the NDP facility. One of the standard preamplifiers traditionally used for charged particle spectroscopy and one that has been

implemented for most NDP applications is the ORTEC 142A Preamplifier. This preamplifier has a relatively fast rise time and good noise characteristics.

In the past for NDP applications, including the NDP facility at NIST, the ORTEC 142A preamplifier was placed as close to the detector as possible. However, due to the size constraints of the NDP chamber as well as the increased number of necessary electrical feedthroughs into the high vacuum chamber, this preamplifier was placed outside the irradiation chamber. The problem with this type of installation is that the preamplifier ideally should be placed closer to the detector with minimum length of cables to reduce capacitance loading and noise introduced into the signal before the amplification.

For NDP systems noise is commonly induced into the signal from the turbo pump used for the ultra-low vacuum system. If this noise is induced before the preamplifier it will be amplified by the preamplifier and can significantly reduce the resolution of the detection system. This is commonly the case for preamplifiers installed outside the sample chamber. In the past NDP facilities such as the one at NIST have electrically isolated the turbo pump from the chamber to reduce this noise contribution as much as possible. If the system is correctly isolated it can reduce much of the induced noise, although usually with some compromise of the signal integrity.

The initial setup of the spectroscopy system for the OSTR NDP facility was similar to what had been done in the past: an ORTEC 142A preamplifier mounted outside the sample chamber, and the turbo pump electrically isolated from the chamber with an O-ring flange and a Teflon gasket. This setup resulted in significant noise fluctuations

when the turbo pump was operating, which could be somewhat reduced by making sure that the preamplifier cables were routed as far away from the turbo pump as possible.

There was also noise that was intermittent and varying in intensity. This may have been from pumps and other mechanical devices associated with the reactor operation. In addition, the output response from the preamplifier had significant overshoot, which was likely due to capacitance loading associated with the cabling and connections used in routing the signal outside the sample chamber. This setup generated inconsistent results with poor energy resolution.

In an attempt to increase the signal-to-noise ratio the preamplifier was placed inside the sample chamber. This positioned it closer to the detector and provided it with additional shielding from external sources.

Because of the size of the ORTEC 142A preamplifier it was not well suited for use inside the sample chamber. Instead a preamplifier from Cremat, Inc., was utilized. The preamplifier from Cremat, Inc., was a CR-110 with similar operational and noise specifications to that of the ORTEC 142A. The specifications of the two preamplifiers are given in Table 2. The advantage of this preamplifier is that it is very small and has all of its components sealed in hard plastic, making it suitable for operation in ultra-low vacuum conditions.

Table 2: NDP Preamplifier Specifications

Preamp	Rise Time at 0[pF] *	Decay Time	Noise (FWHM)(Si)
	[ns]	[μs]	[keV]
Ortec 142A	5	500	1.6
Cremat CR-110	7	140	1.7

* $R_{t\text{total}} = R_t(\text{preamp}) + 0.11(Cd[\text{pF}])$

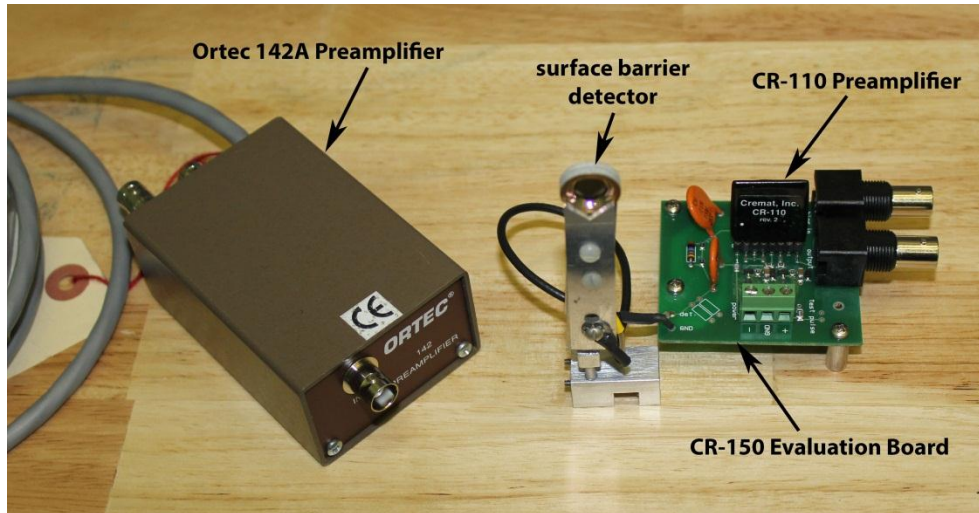
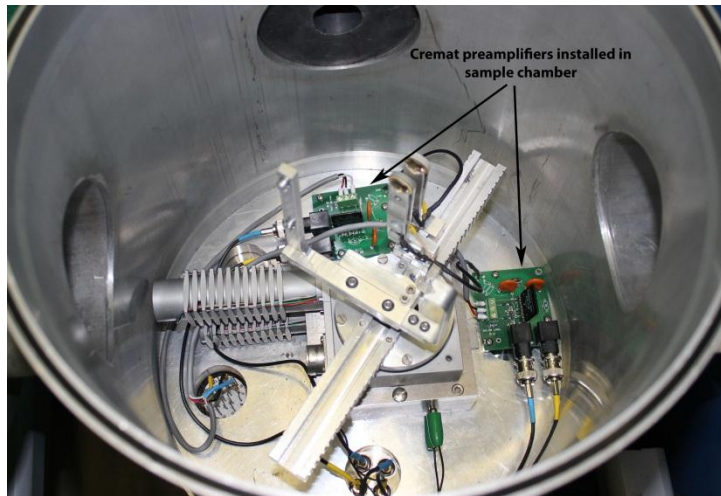
The CR-110 does not have a power supply regulation circuit or the components necessary to apply and filter the high voltage bias to the detector. These additional components were provided by using a CR-150 evaluation board also from Cremat, Inc., which provided AC coupling between the detector and the preamplifier. The CR-150 comes equipped with a bias filter resistor value of $10 \text{ M}\Omega$ and a bias resistor value of $200 \text{ M}\Omega$. These values are appropriate for detector leakage currents in the range of 0-10 nA.

For leakage currents greater than 10 nA there will be a significant voltage drop across the detector, resulting in incomplete depletion across the detector. The leakage currents of the surface barrier detectors used for the NDP facility according to the manufacturer [24] are in the range of 10-50 nA, and for some of the older detectors that have neutron damage from many hours of use for NDP measurements it is higher than this. Considering the detectors that were implemented in the facility and the suggested values from Cremat shown in Table 3, a $10 \text{ M}\Omega$ shunt resistor was added to the evaluation board.

Table 3: NDP Suggested Resistor Values

Leakage current range	R1	R2	R2
0-10 nA	(left Open)	(left Open)	(left Open)
30-100 nA	(left Open)	(left Open)	22 MΩ
100-300 nA	(left Open)	(left Open)	10 MΩ
300 nA-1 μA	3.3 MΩ	3.3 MΩ	3.3 MΩ
1-3 μA	1 MΩ	1 MΩ	1 MΩ
3-10 μA	330kΩ	330kΩ	330kΩ
10-30 μA	100kΩ	100kΩ	100kΩ

Ref. [25]

**Figure 11: Preamplifiers used for NDP charged particle spectroscopy****Figure 12: NDP Cremat preamplifier configuration**

In order to evaluate the new CR-110 preamplifiers relative to the 142A a series of spectra were taken for both preamplifier configurations. In addition the waveform output signals were evaluated using a high-frequency digital oscilloscope. These results demonstrated considerable improvements in detector resolution as well as improved sensitivity in the low-energy regions for the Cremat preamplifier installed inside the sample chamber. In addition the overshoot, which was absorbed in the response from the 142A preamplifier, did not occur for the CR-110 preamplifier. A graphical representation of the results from these experiments is presented in Figure 13 and Figure 14.

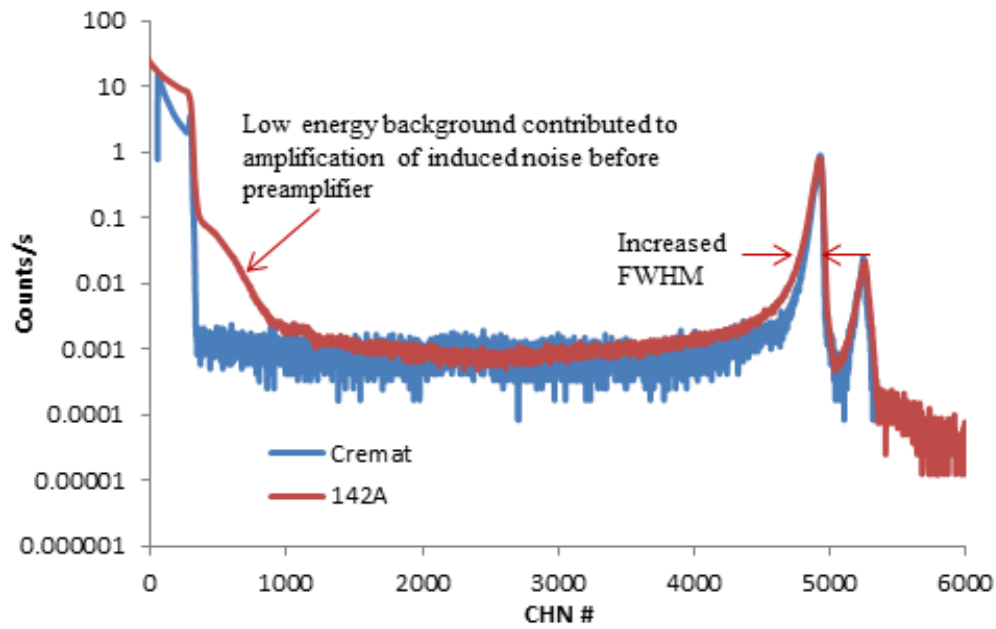


Figure 13: Pu-239 spectrum (Preamplifier comparison)

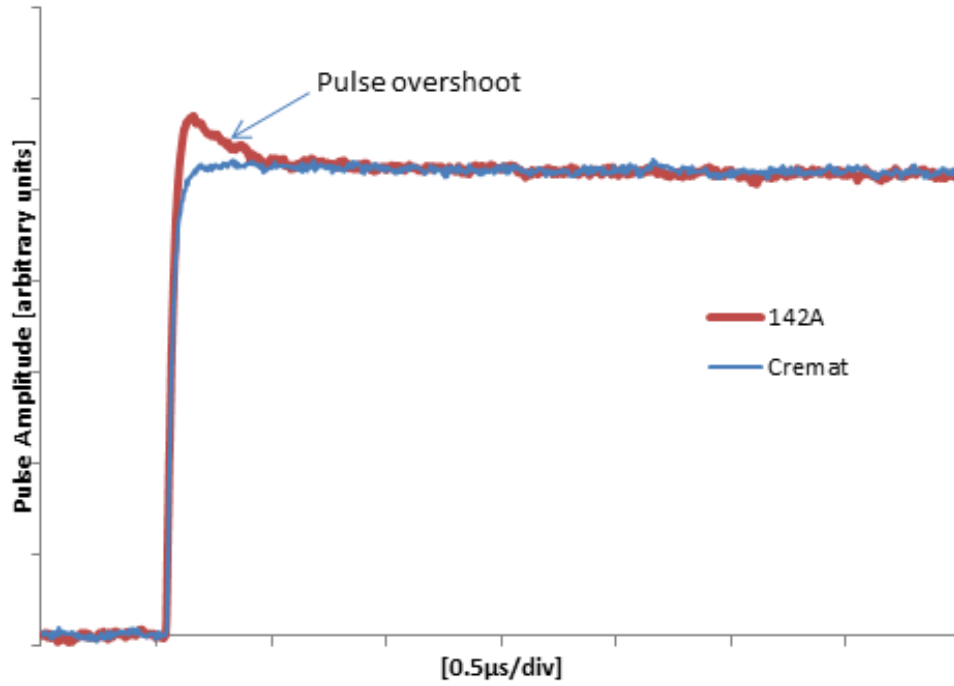


Figure 14: Preamplifier pulse comparison

Overall these results showed significant improvement from having the preamplifier installed inside the sample chamber. As far as the specifications are concerned, both preamplifiers should have similar response and noise characteristics and should be equally suitable for the NDP application. However, due to the size limitations of the sample chamber, the CR-110 was a much better choice for this application.

5. Signal Processing

A standard analog radiation detection system consists of radiation detectors (these are charged particle detectors in the case of NDP) and the rest of the signal processing chain. The signal processing chain consisted of analog signal processing to shape and measure the response from the detector. For most NDP systems currently in operation, the signal processing chain consists of a charge-sensitive preamplifier, amplifier, analog-to-digital converter (ADC), and a multichannel analyzer (MCA). The diagram in Figure 15 illustrates the basic components of this system.

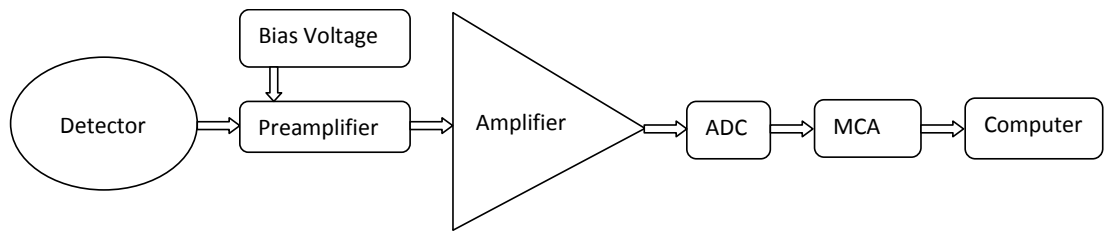


Figure 15: Basic components of a standard analog radiation detection system

The preamplifier, which acts as a charge-to-voltage converter, amplifies the signal typically on the order of a couple of volts per pC of charge. The preamplifier typically contains the circuitry to provide the operating bias to the detector. The detector is then closely coupled to the preamplifier to minimize noise and interference. Additional amplification and shaping are done with a shaping amplifier, which usually has user-selectable shaping parameters such as the gain and the shaping time. The ADC and MCA are used to produce a histogram of the amplitude of the shaping amplifier response and the resulting histogram is recorded to the computer. This system works

very well for standard radiation measurements in which the energy deposited in the detector is the only information of interest and for count rates where pileup effects are of little concern.

However, as analog-to-digital converters have increased in resolution and speed, many detection systems are drifting towards digital signal processing for which the detector response from the preamplifier is digitized with a high speed, high resolution ADC and then processed with digital filters. The digital filters provide all the necessary shaping and filters to increase the signal-to-noise ratio and are implemented entirely through software programming. The basic components of a digital signal processing system are illustrated in Figure 16.

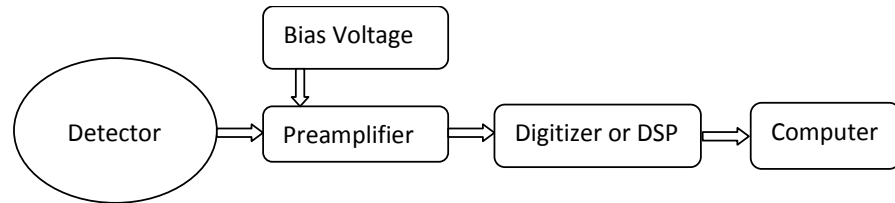


Figure 16: Basic components of a digital radiation detection system

Digital data acquisition has many advantages over analog systems. With advances in technology, modern digitizers have reached a speed and resolution such that they can replace many analog systems with equivalent signal shape and energy resolution and can improve detection capabilities with appropriate digital data processing. Also, due to the nature of the data processing for spectroscopy applications, considerably higher count rates can be handled by digital systems in comparison to analog systems, and can offer great improvements in system dead times. For this reason the focus of the detection system for the new NDP setup has been towards developing digital signal processing capabilities designed specifically for NDP analysis in order to

improve detection capabilities and the versatility of the system. During the development of this system, a standard off-the-shelf ORTEC multichannel analyzer was used for initial measurements and system verification, and a high-speed digitizer was used for advanced data analysis.

5.1 ORTEC DSPEC Pro

The DSPEC Pro, which was used for the initial data acquisition on the NDP system and for characterization of the digital system, is one of the standard spectrometers used for gamma spectroscopy with HPGe detectors. This is the same system which is used for the HPGe detector on the PGNAA facility and has proven to be very reliable and consistent. One of the advantages of this system is that it implements some digital pulse processing to correct for electronic noise and low-frequency periodic noise [26], making it ideal for an HPGe detector, especially for high count rate applications.

Although this system is very good for gamma spectroscopy, in which only a measurement of the pulse amplitude is necessary, for particle energy spectroscopy it does not have the capability or the time resolution to measure differences in detector response such as the rise time. In addition, although it does have the capability to obtain timing measurements for the individual pulse responses when operating in List Mode, this feature is somewhat limited, difficult to use and requires post processing the data after the acquisition before any analysis of the data. It is also not possible to make significant changes to the internal filters or to obtain the raw waveform from the individual pulse responses from the detector.

Because of these limitations, and the versatility of a detection system in which all the signal processing after digitization of the preamplifier signal is done entirely through user programmable software, a digital signal processing system has been

implemented for the analysis of the detector response from the surface barrier detectors.

5.2 High Speed Digitizer for Digital Data Acquisition

Since the development of high-speed analog-to-digital converters, digital signal processing with the ability to digitally capture the behavior of high-frequency analog signals has rapidly been replacing the standard analog signal processing systems. These digital systems can be easily changed for experimental conditions since all the data processing is implemented through software programming. In addition they reduce the number of components found in a standard analog signal processing chain through which noise can be induced or other factors affecting the measurement can result in poor data.

There are several digitizer companies manufacturing NIST traceable calibrated digitizers with a wide range of specifications and capabilities that are suitable for spectroscopy. Virtually all of these digitizers implement hardware triggering, and many of them have the ability to continually stream data to the computer, allowing the entire data stream to be processed by the computer CPU. In addition, some more recent high-speed digitizers have the ability to digitally process the data in real time through a Field Programmable Gate Array (FPGA). The advantage of the FPGA, especially for the case of spectroscopy in which digital filters are used for triggering, is that the computer overhead is greatly reduced since only the data of interest is transferred to the host PC.

Hardware triggering has the same effect as FPGA on board triggering in that only the section of the waveform response of interest from individual events is transferred

to the computer. The disadvantage of hardware triggering is that it is limited in its ability to reliably trigger at very low threshold levels, owing to the base-line noise, and it cannot detect a pulse that occurs before the previous pulse response amplitude has decayed below the trigger threshold.

Because the count rates for the NDP facility were expected to be relatively low, and due to the high intensity background in the very low energy range, it was assumed that hardware triggering would be sufficient for most applications for which this facility would be used.

In addition to the initial data processing such as triggering and data transfer, perhaps some of the most important parameters of the digitizer are the bandwidth, sample rate which determines the resolution in the time domain, and the number of bits of vertical resolution for the ADC. For digital signal representation these are chosen based on the characteristics of the signal to be processed.

The sample rate of the digitizer must be frequent enough to reconstruct the signal shape to extract the necessary information. As a general rule the sample rate should be at constant intervals, and be at least twice that of the highest frequency component of the signal to be processed. This is known as the Nyquist sample rate, after Harry Nyquist who developed it for use in telegraph transmission systems in 1924 [27].

For the NDP charged particle spectroscopy application with surface barrier detectors, the signal rise times are in the range of 20-80 ns. For a step response such as the signal observed in radiation spectroscopy, the bandwidth of the signal can be approximated as shown in Equation 5.1 [28],

$$\text{Signal bandwidth} = \frac{0.35}{\text{Rise time of the signal}} \quad (5.1)$$

Thus, the signal bandwidth for the surface barrier detector will be in the range of 17 MHz. According to the Nyquist sample rate, the digitizer should have a sample rate of at least 34 MS/s in order to accurately reconstruct the frequency characteristics of the signal. However, at this sample rate, even though the frequency is preserved, the sample rate is still too low to accurately reconstruct the amplitude behavior of the signal for its highest frequency component. For pulse shape analysis applications for which an accurate measurement of the rise time of the signal is required, the sample rate should be at least 4 or 5 times greater than the Nyquist sample rate, which would record ~10 samples in the rising edge of the fastest pulses expected from the surface barrier detectors. For this reason the digitizers considered for this project were in the range of 180 to 200 MS/s.

After determining the needed sample rate of the digitizer, it was necessary to look at the required resolution. The maximum vertical resolution of standard high-end digitizers in this range for most of the manufacturers was 14 to 16 bits. For spectroscopy measurements this could be interpreted as 16,384 channels for the 14-bit digitizer and 65,536 channels for the 16-bit digitizer. However, since the signals generally have a steady baseline near zero and the pulses from the detector have only positive step responses, only half of the vertical depth of the digitizer would be utilized, which would translate into about 8,000 and 32,000 channels for the 14 and 16 bit digitizers respectively.

For NDP the energy range for most measurements is typically no more than 3000 keV, which would mean that with the 14-bit digitizer there would be approximately 0.5 keV per channel, and since the resolution of the standard surface barrier detectors used in the facility are around 15 keV FWHM this would be more than adequate.

However, since this facility is designed to perform both NDP and PGNAA analysis separately or simultaneously there is the possibility that the digitizer may be used for the PGNAA prompt gamma spectroscopy as well. For PGNAA the energy range of interest is from a few keV up to about 10 MeV, which would mean that there would be approximately 1.25 keV and 0.31 keV per channel for the 14 and 16 bit digitizers respectively. The HPGE detector used for the prompt gamma spectroscopy has a resolution of 1.75 keV FWHM, which means that if the 14-bit digitizer were used for this system it could potentially reduce the overall resolution of the counting system. For this reason the 16-bit digitizer was chosen so that the system would be more versatile for possible future experiments involving use of the digitizer for both PGNAA and NDP analyses.

During the development of this system two different digitizers were evaluated and tested with the facility, one from AlazarTech and one from GaGe. For the initial setup and preliminary measurements an ATS9462-PCI Express 16-bit digitizer with a maximum sample rate of 180 MS/s was obtained from AlazarTech [29].



Figure 17: ATS9462 digitizer board

This is a dual-channel digitizer which has the capability of operating in continuous streaming mode as well as operating with a hardware trigger. The rearm time of the board is about 700 ns at 180 MS/s, which is insignificant for NDP spectroscopy since the decay time for the preamplifier is several hundred microseconds, meaning that the board will be ready to trigger long before the signal has crossed back down below the trigger threshold level.

For the hardware trigger the board can return a time stamp for each trigger event as well as post and pre-trigger samples. Custom programming of the board can be implemented with software development kits for C++, C, Matlab, and LabVIEW.

The data transfer to the computer can operate in dual port memory mode, which allows the data to be transferred to the computer during the data acquisition. The advantage of this is that trigger events will not be missed during transfer to the host PC, providing the overall transfer rate does not exceed the maximum speed at which the computer can write the data to the hard drive. If the maximum rate dose exceed the

maximum transfer rate for an extended period of time and the digitizer onboard memory is filled, the board will stop acquiring data and return a buffer overflow error.

For Matlab, initial measurements demonstrated that this board would operate continuously without overflowing the buffer at 900 counts per second while implementing a trapezoidal filter in Matlab to calculate pulse amplitudes and update a plot of the pulse height energy histogram in real time. The limitation in speed for this case is entirely due to Matlab overhead and the speed of the computer processor used for the data acquisition. However, these speeds are more than adequate since the count rates for the NDP facility are not expected to be over a couple hundred counts per second. In C++ speeds considerably higher than this on the order of several thousand counts per second can be achieved.

For reasons that were not fully understood and were not solved by the manufacturer, the board was somewhat unreliable in Matlab although it seemed to work perfectly in C++. Ultimately the board did work well for data acquisition using an optional FIFO memory mode with Matlab in which each record of data was transferred to the computer individually as it was acquired. However, in this Mode Trigger time stamping was not available. Even though the product support from AlazarTech is excellent, they were unable to reproduce the problem, so the board was sent back to the manufacturer and a new board from GaGe Applied Technologies, Inc., was obtained [30].

The digitizer board from GaGe Applied Technologies, which is now the dedicated digitizer board for the NDP facility data acquisition, is a dual-channel PCI-Express

16-bit digitizer with a maximum sample rate of 200 MS/s. It also has hardware triggering as well as some advanced hardware triggering capabilities that were not available from the ATS9462 AlazarTech board. Dual-port memory mode is also available for C++ programming but it is not available in Matlab. The GaGe digitizer used in this work is pictured in Figure 18 installed in the PCI express slot of the computer.

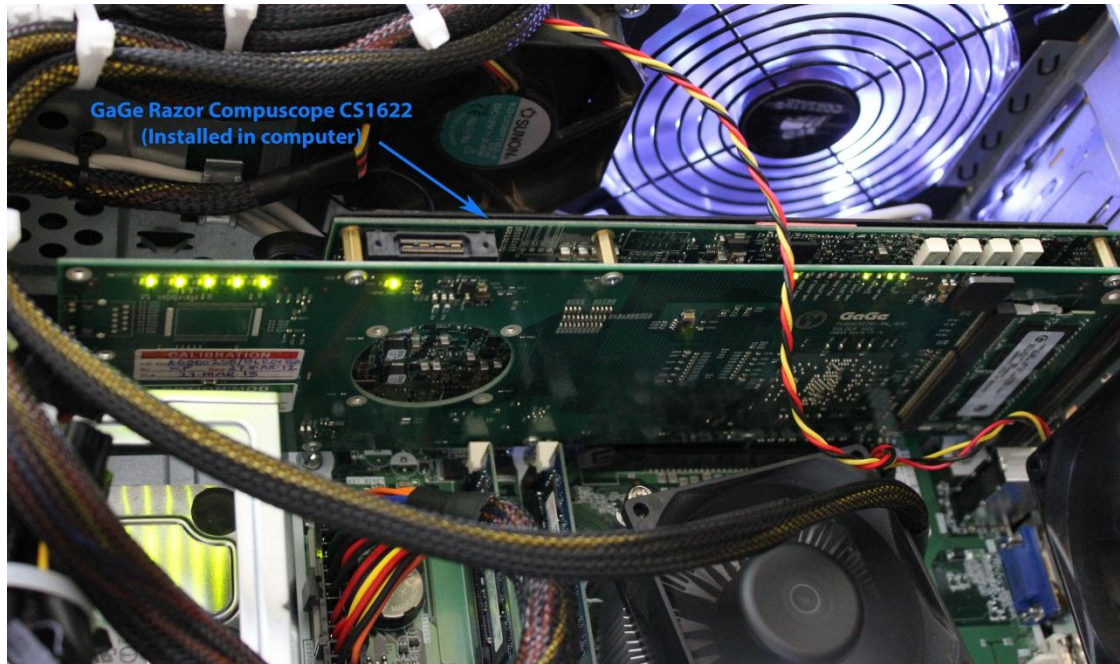


Figure 18: GaGe Razor Compuscope CS1622 digitizer board

For Matlab applications multiple records can be captured with a rearm time of less than 2 μ s continuously until the on-board memory on the digitizer is filled. If it is necessary to capture more data than can be stored on the on-board memory there is a short pause in the data acquisition while the data is transferred to the PC. During the development of the Matlab code for the data acquisition it was found that this results

in dead times of about 3% for a count rate of 150 counts per second for which the pulse record length is 2,048 samples and the digitizer is set to 200 MS/s.

For these measurements the transfer rate to the PC was optimized by saving the data to a variable matrix, which was saved to a file on the computer while additional records were being stacked in the digitizer on-board memory. For future applications in which dead times could become large enough to significantly limit the NDP measurement, or for measurements for which the pause in data acquisition is unacceptable, any codes developed in Matlab can be transferred to C++. This would allow the board to operate in dual-port memory so that the data could be transferred to the computer simultaneously during the data acquisition. However, for this to work with some of the data processing functions available in Matlab and for simplicity, all of the data acquisition programs were written in Matlab.

5.3 Pulse Shape Discrimination

The main reason to move towards digital signal processing for the NDP system was to provide a system for which techniques such as pulse shape discrimination, data filtering, and coincident measurement could be easily configured and implemented with minimal hardware adjustments for any type of signal received from the charged particle detection system. There were several steps in the development of this system.

The first were preliminary measurements of rise times with some of the surface barrier detectors used for the charged particle collection for the NDP system. Based on previous research there is reason to believe that there may be slight differences in the rise times and shape of the detector signal depending on the type of particle interaction in the detector for the particles of interest during an NDP analysis. The rise time for a typical surface barrier detector is usually in the range of 10-20 ns for the measurement of charged particles impacting the front side of the detector. The main factors that contribute to the rise time are the “charge transit time” and the “plasma erosion time.” In addition, in partially depleted regions of the detector, trapping and de-trapping and recombination can affect the shape of the detector response as well as the resolution of the detector.

The charge transit time is the time it takes for the electrons and holes to migrate across the depleted region of the detector. The plasma erosion time, which is observed only with heavy charged particles and fission fragments, is caused by a high density of electron-hole pairs created along the path of the particle. Because of the high-density

cloud of electron-hole pairs the electron-hole pairs within the interior of the cloud are shielded from the electric field by those on the outer edges. The result is that electron-hole pairs are gradually eroded away until those on the interior are subject to the electric field. The result of this is an increase in the charge collection time and therefore an increase in the rise time and possibly a change in the shape of the detector response.

Assuming that effects from trapping, de-trapping, plasma erosion, and recombination are insignificant, the charge transit times are dependent on the depth of the depletion region in the detector. Derivation of this leads to Equations 5.2-5.4, which describe the charge collection as a function of time [31]. This result is presented in three equations because the charge collection time depends on whether the electrons and/or holes have been collected. Where $Q(t)$ is the charge collected as a function of time, q_0 is the total charge to be collected, v_e and v_h are the electron and hole drift velocities, d is the depletion depth and x is the position within the depletion depth.

While both electrons and holes are drifting,

$$Q(t) = q_0 \left(\frac{v_e}{d} t + \frac{v_h}{d} t \right) \quad (5.2)$$

If electrons are collected but holes are still drifting,

$$Q(t) = q_0 \left(\frac{x}{d} + \frac{v_h}{d} t \right) \quad (5.3)$$

If holes are collected but electrons are still drifting,

$$Q(t) = q_0 \left(\frac{v_e}{d} t + \frac{d-x}{d} \right) \quad (5.4)$$

It can be seen from these equations that the effect on rise time is dependent on the distance the electron-hole pairs have to travel in the x direction. In addition, since the drift velocity for holes is generally slower than the drift velocity of electrons, the collection time is dependent on where the electron-hole pairs are created within the detector [32].

Trapping can degrade the resolution of the detector as well as the shape of the detector response. Ideally the pulse response from the detector should have a constant slope until the maximum height of the pulse is reached. For the case of trapping alone, the result is a pulse with reduced amplitude and a curvature to the slope that decreases near the top of the pulse. The initial rise time for this case should be the same as that of the case in which there is no trapping. Providing recombination does not occur and the trap is shallow, the trapped electrons will eventually be released by thermal excitation. This will result in a pulse with a fast component and a slow component for the electrons released from thermal excitation.

Of the effects mentioned above, de-trapping and the plasma erosion time all lead to increased rise times for the detector response. Prior to this work, rise time measurements and pulse shape discrimination had not been implemented in surface barrier detectors in an NDP configuration. The main reason for this is that with the standard analog systems implementation of rise time measurements required a great deal of instrumentation, expense, and were not easily modified for changing experimental conditions.

5.4 Digital Signal Processing

As mentioned in Section 5.2, an ATS9462 AlazarTech digitizer and a GaGe Razor Compuscope CS1622 digitizer were used for digital data acquisition. These digitizers provide a raw digitized signal from the input of the preamplifier, which was then analyzed by digital signal processing through software programming.

In some experiments, especially for the case with the AlazarTech digitizer, it was necessary to install an amplifier between the preamplifier and the digitizer. This was because for very low-level signals within about 5% of the input range of the digitizer, the hardware trigger in the digitizer was not sensitive enough to trigger and reliably capture all the data in this range. The amplifier which was chosen for this application was a FEMTO Voltage-Amplifier (DHPVA -200). This amplifier is pictured in Figure 19.



Figure 19: FEMPTO (DHPVA-200) Voltage-Amplifier

The specifications for this amplifier are presented in Table 4. This amplifier was chosen because it is strictly a high-frequency voltage amplifier with low noise characteristics. As a result, the output signal from the amplifier will preserve the

signal shape and relative amplitudes of the original signal. This is especially important for digital pulse shape analysis in which the signal must be characteristic of interaction mechanisms within the detector.

Table 4: Voltage Amplifier Operating Specifications[33]

Model	DHPVA-200
Lower Cut-Off Frequency	DC/10 Hz
Upper Cut-Off Frequency	20/200 MHz, Switchable
Gain Flatness [dB]	± 0.15
Gain [dB]	10/20/30/40/50/60
Input Noise Voltage	2.5 nV/Hz
Input Voltage Drift	0.6 μ V/ $^{\circ}$ C
Input/Output	50 Ω , BNC
Output Voltage (Power)	± 1 V (+10 dBm)
Monitor Output	DC - 100 kHz
Digital Control	TTL, CMOS, Opto-Isolated

Other than the preamplifier and the amplifier, all signal processing for the digital system is done through data processing algorithms that implement digital filters. These algorithms are used to analyze the various characteristics of the digitized signal from the high speed digitizer.

As mentioned in Section 5.2, the digitizer is implemented with the built-in hardware trigger. The hardware trigger, as well as all other user adjustable parameters that control the digitizer functionality such as the input gain, impedance, data handling, and channel input parameters, are programmed through C/C++, Matlab, and LabVIEW with software development kits provided by GaGe. These kits provide all the necessary software drivers to communicate with and program the board.

For data acquisition the digitizer is designed to operate in several modes depending on the type of data and the duration for which the data must be captured. These modes

include the ability for the digitizer to operate in dual-port memory mode as well as continuous data streaming.

For the case of charged-particle spectroscopy, the continuous streaming mode could be used to transfer the entire digitized data stream from the digitizer to the computer in which it could be processed through a digital filter with software programming such as a trapezoidal filter, to extract and save to disk only the data that are characteristic of individual particle interactions within the detector. There are several advantages to this method over hardware triggering. Two of these are listed below.

- (1) The pulses that would ordinarily be missed by a hardware trigger due to pulse pile-up are easily separated with a digital filter, such as a trapezoidal filter, greatly reducing missed pulses and eliminating system dead time.
- (2) Pulses that the hardware trigger threshold is unable to capture due to fluctuations in the base-line noise are also easily separated and analyzed with digital filters.

The disadvantage of the data-streaming method, especially for sample rates of 200 MS/s, is that a very large amount of computer overhead is necessary to process the data. In addition, all the data-processing algorithms would need to be written in C++ in order to achieve the speeds necessary to keep up with the data flow.

Alternatively, in order to reduce computer overhead, the board can be operated in dual-port memory mode with a hardware trigger. The hardware trigger would be set to trigger when the signal rose above a specific trigger threshold. The specified number

of pre-trigger and post-trigger samples would be saved to a memory buffer on the digitizer board and then transferred to the computer. With this method, the rearm time for the digitizer trigger engine is very low (about 2 μ s) because the data can be transferred to the dual-port memory from the digitizer simultaneously while the previous data are being transferred to the computer. Also, since the decay time for the preamplifier is generally much larger than the rearm time it does not have any effect on system dead time. Therefore pulses that occur immediately after the decay of the previous pulse and have decayed below the trigger threshold will not be missed, providing the overall transfer rate to the computer is not exceeded.

The advantage of these two modes is that it is not necessary for the digitizer to stop acquisition to transfer the data to the computer. This greatly reduces system dead time for long continuous data acquisition.

Because of the increased computer overhead required for processing the entire data stream in real time, and since the count rates for NDP are not high enough to result in a large effect on dead time due to pile-up pulses, it was decided that the digitizer would be implemented with the hardware trigger for the NDP application.

Because of past experience and the available programming resources, Matlab was used for the data processing and programming of the digitizer. The disadvantage with using this programming language is that Matlab is an interpreted programming language, making it considerably slower than compiled codes such as C++. Also for the case of the GaGe digitizer the Matlab driver did not allow full functionality of the dual-port memory. Instead, the data acquisition had to stop temporarily to allow the

data to be transferred from the on-board memory to the computer. However, since more than 10,000 pulses could be stacked in the on-board memory and the transfer rate was fairly fast, it was found that for long continuous data acquisitions with count rates of about 200 counts per second this only introduced about a 2-3% transfer dead time.

5.4.1 Pulse Acquisition

As mentioned in the previous section, the individual pulses for each particle interaction above a specified trigger level were acquired from the high-speed digitizer which was triggered through the built-in hardware trigger engine. The hardware trigger threshold was set so that it was just high enough to eliminate trigger events from base-line fluctuations and random noise.

For the case of the GaGe digitizer the data was sampled at 200 MS/s with 1024 samples recorded before and after each trigger event. Provided in Figure 20 is an example of a digitized pulse from the NDP charged particle system for an alpha-particle incident on the front side of the surface barrier detector.

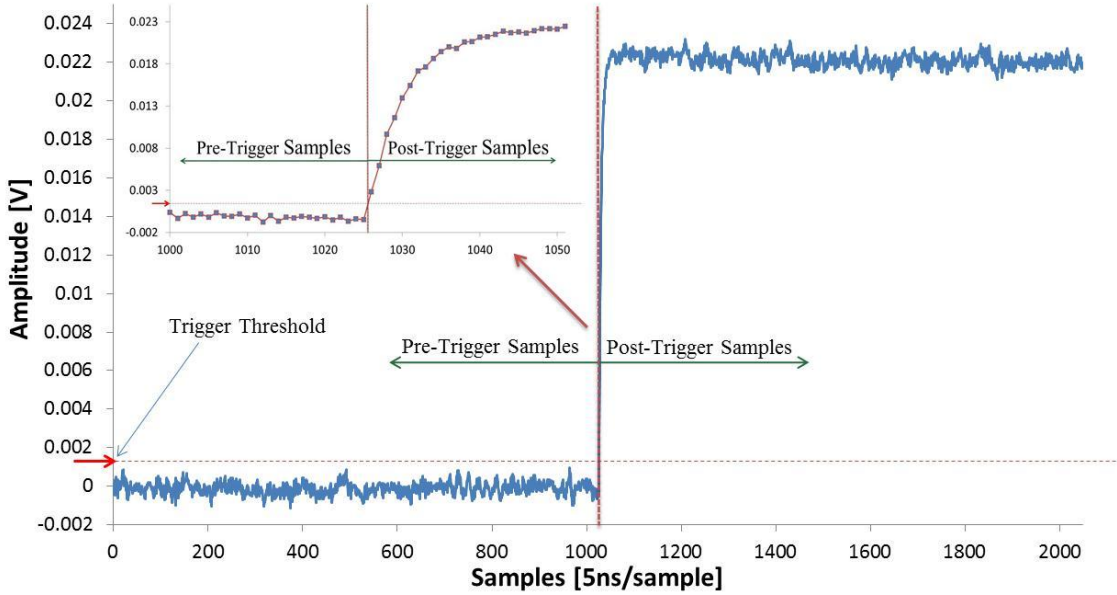


**Figure 20: Digitized pulse for a single alpha interaction from the NDP surface barrier detector
(Data taken with GaGe digitizer)**

This pulse has a sufficient number of samples before and after the trigger to accurately reconstruct the entire waveform detector response, especially in the rising edge of the pulse which is important for rise-time pulse shape analyses.

Because of the number of samples recorded and the sample rate of the digitizer this pulse does not include the decay of the pulse back down to the baseline. This however is not important for pulse shape analysis since the rate of decay is dependent on the charge-sensitive preamplifier and therefore will be the same for every pulse.

For a continuous data acquisition as the data are ported from the digitizer to the computer, processing can be done during the acquisition. Also, if the entire waveform is saved to a file it can be post-processed after the acquisition. Since some of the data analysis required a large amount of computer processing time, which would have increased the system dead time, each individual raw pulse was saved to a binary file. This not only increases the possible processing that could be done on the data without increasing the experiment run time, but it makes each measurement much more versatile in that the data can be analyzed as many times as necessary to optimize the analysis. For the acquisition system developed for the NDP application, the only parameter calculated during the acquisition was the amplitude measurement for each pulse which was plotted in real time. This was done so that the user would have the ability to monitor data during the acquisition.

In addition to the raw data, a file can also be saved with the time stamp for each trigger event, which is especially useful for coincidence measurements in which more than one detector is used.

5.4.2 Pulse Amplitude Measurements.

For most charged particle measurements, the amplitude of the detector signal response is necessary to determine the energy deposition within the detector. For this measurement both the base level of the signal and the peak amplitude of the signal are needed. A common way of doing this is with a trapezoidal filter.

The trapezoidal filter used for pulse triggering is a type of convolution, which is represented by the Equation 5.5, where y is the filter output, h are the filter coefficients, z is the raw input data, n are the index values for filter output and input data, and N is the number of filter coefficients.

$$y(n) = \sum_{i=0}^N h(i) \cdot z(n-i) \quad (5.5)$$

The trapezoidal filter subtracts the average of certain data points in the original data from the average of another set of data points. This difference becomes part of the convoluted data set. This is demonstrated in Figure 21. Each data point in the filtered data set is constructed by subtracting a set of points of length Δt_L from another set of points also of length Δt_L . The two sets of points are separated by a gap of length Δt_G . The gap length Δt_G must be longer than the time scale of the change in amplitude being measured. The result of this filtering operation is to remove random fluctuations and give the magnitudes of distinct changes in the data. The output pulse has the trapezoidal shape which gives it its name.

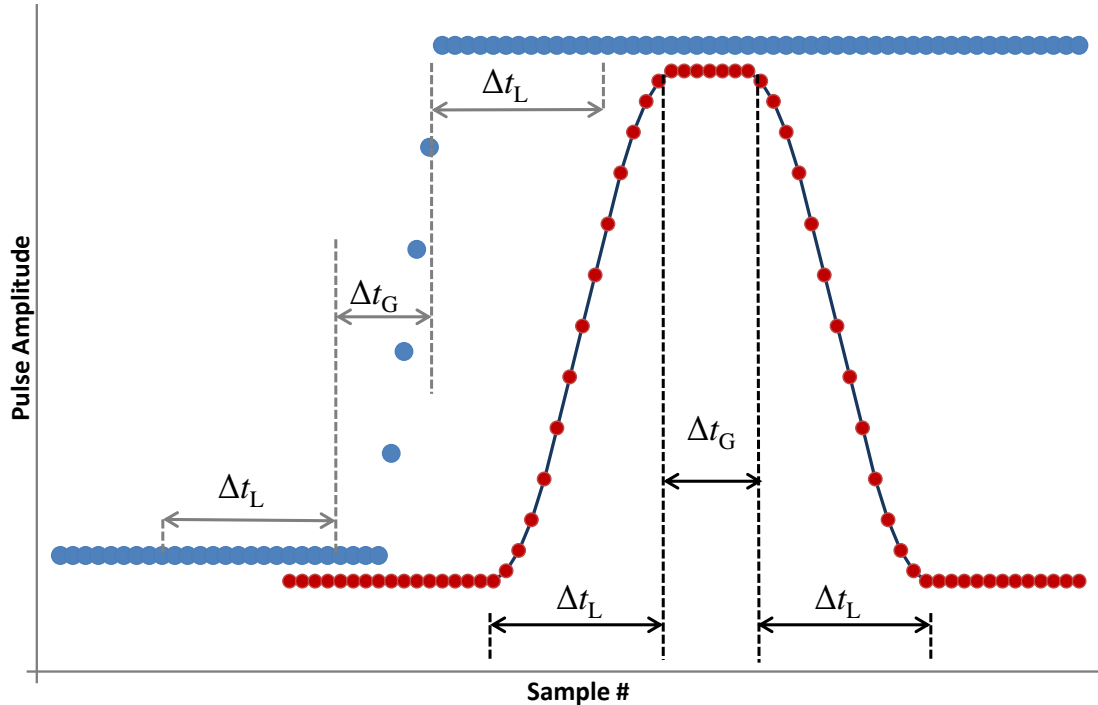


Figure 21: Trapezoidal filter. The filter generates a trapezoidal shape with a height that matches the step change in the data, and filters out random fluctuations.

The advantage of using this type of filter is that for changes in the signal with a relatively long time scale the filter returns a signal with a zero baseline. An example of this would be the decay signal from the preamplifier. As a result, pileup events are easily separated into distinct peaks for which the amplitude is proportional to the maximum amplitude of the individual signals. An example of this is demonstrated in Figure 22. In this figure, three pulses from individual detection events are shown on top of each other. This is common for high count rate applications where pulses occur before the previous pulse has decayed.

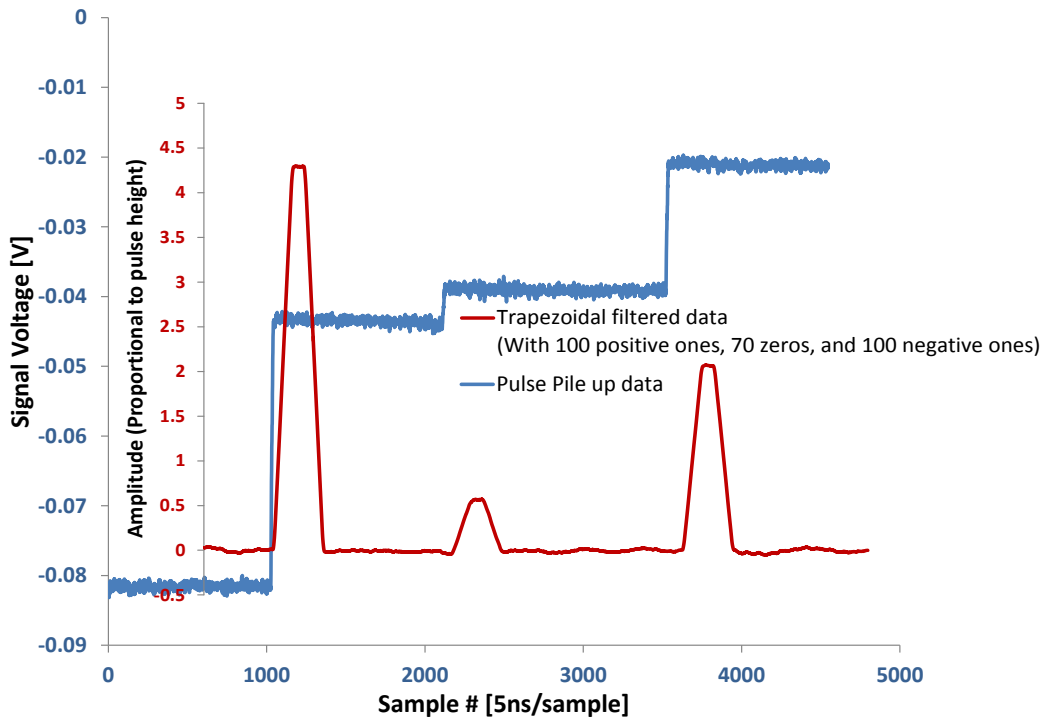


Figure 22: Example of pileup events separated using a trapezoidal filter.

Also, since the trapezoidal filter has a zero base level, any DC offset in the signal is effectively subtracted out of the signal. Therefore it is only necessary to measure the maximum value of each trapezoidal filter event to get the relative amplitudes of each detection event.

Trapezoidal filters are also ideal for applications for which software triggering is implemented. For this case the entire data stream from the ADC is filtered through a trapezoidal filter, and a trigger threshold is set on the filtered data to record segments of the data for which the filtered data exceeds the threshold. This type of triggering is much preferred over hardware triggering because it is not sensitive to fluctuations in the baseline and it can be used to detect low-level signals for which the hardware trigger cannot be set low enough to detect. Applications that are well-suited to this type of analysis are digitizers for which the computationally extensive data analysis

can be implemented with an onboard FPGA. Alternatively, the entire data stream can be streamed to the computer; however, depending on the digitizer sample rate the computational overhead may be too great for the computer.

For this work, since most of the programming was implemented in Matlab and since the digitizer used did not have an on-board FPGA, pulses were detected through hardware triggering and a specified number of pre-trigger and post-trigger data points were captured. The amplitudes were then measured by filtering the resulting data through a trapezoidal filter implemented in Matlab. The only limitation this placed on the system was an increase in dead time for high count rate applications and a higher limit on the detectable pulses. This however was determined not to be a problem since the count rates for the NDP application were relatively low and the trigger level was sufficient to capture all pulses within the energy range of interest.

5.4.3 Rise Time Measurements with Wavelet De-noising

The pulse shape analysis technique used in this work was based on measuring the individual rise times for each of the digitized detector pulse responses and looking for differences between pulses that could give information about the particles interacting within the detector.

The rise time for an electrical signal is often defined as the time it takes for the signal to go from 10% to 90% of its maximum amplitude. Algorithms for calculating the rising time for a signal are straightforward; however, for signals with a high background noise it becomes more difficult to reliably measure the rise time of the signal. For this reason several methods of smoothing the data before calculating the rise time were tested to determine the best smoothing method to increase the sensitivity of the measurement. This is especially important for signals that have amplitudes close to the magnitude of the baseline noise fluctuations.

The biggest challenge in smoothing the data for the NDP application was finding a smoothing technique that would take out the noise in the signal and at the same time preserve the shape of the signal in the time domain. This was especially challenging because of the step response for the initial rise of the signal. It was also important that the smoothing method used would be able to handle a wide variety of pulse characteristics.

Many methods are used to eliminate unwanted features in signals and plots. These include fitting functions with the same characteristic shape as the data or passing the data through a filter to remove unwanted features of the signal.

Fitting functions to data works very well, providing a function can be found that can accurately reconstruct the shape of the data. One commonly used method is least-squares polynomial curve fitting. Polynomials are often used when the shape of the function is irregular and does not have any sharp changes such as would be the case for a step function. The data in Figure 23 demonstrate a digitized signal from the NDP detection system that has been fitted with a 10th and 20th order polynomial.

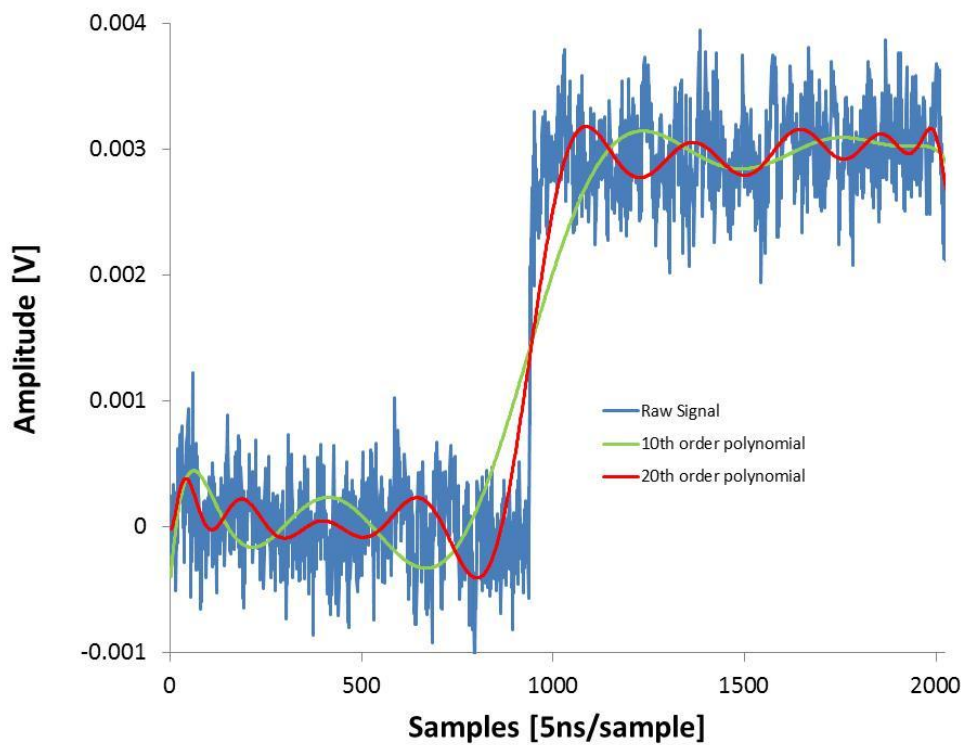


Figure 23: De-noised digitized pulse using polynomials

It can be seen from these data that high-order polynomial functions do not provide enough smoothing, nor are they able to preserve the time domain characteristics of the signal. This is because of the fast step response of the initial rise of the signal. One way around this would be to treat the signal as a piece-wise function and fit the data with separate functions.

A common way of doing this is cubic splines in which the data are divided into even intervals and fitted to many cubic polynomials. The mesh size or spacing between the polynomials would determine the amount of detail preserved within the original signal. An example of this is demonstrated in Figure 24 for several cubic splines with different fitting parameters.

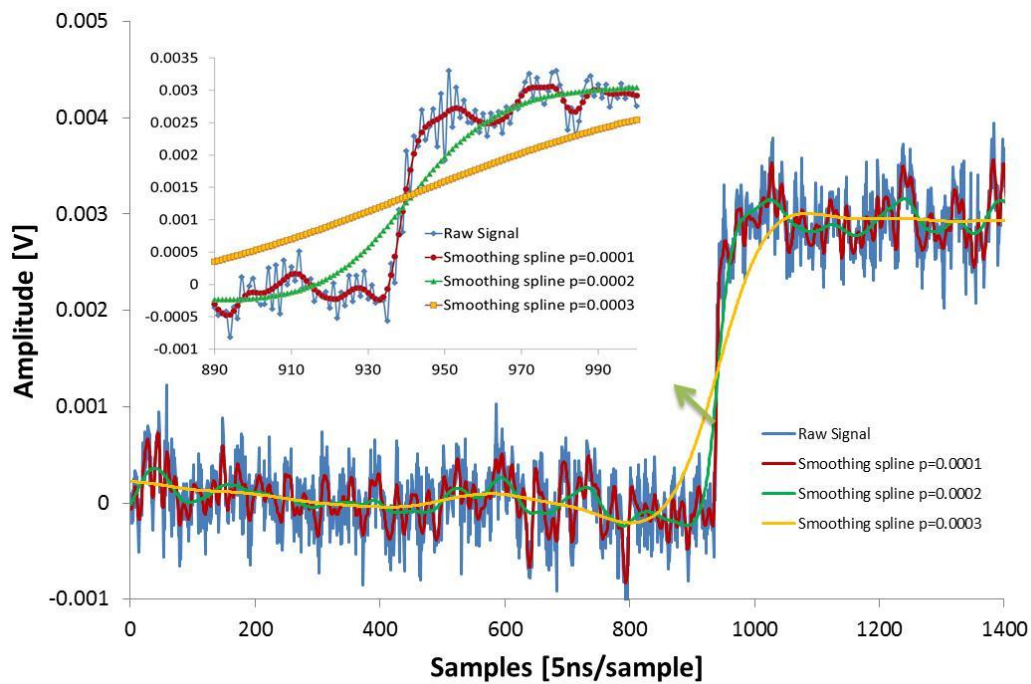


Figure 24: Data smoothing with cubic splines

It can be seen from these data that cubic splines do work to smooth data and with the appropriate smoothing parameter the rising step response of the signal is preserved in the time domain. The problem with this method, which can be seen between the spline with smoothing parameters of 0.0001 and the one with 0.0003, is that there is a tradeoff between preserving the time characteristics of the signal and the amount of noise that can be removed from the signal. As a result, only a limited amount of noise can be removed from the signal without losing the signal shape characteristics.

The method that was ultimately used to remove noise from the data and found to work considerably better than the previous methods was wavelet de-noising with Haar wavelets. Haar wavelets have proven to be effective in taking out random fluctuations of noise from data, while preserving the actual characteristics of the data [34].

The first step in wavelet de-noising is to perform a wavelet transformation of the original data set. Preferably the vector of original data has a length from the dyadic sequence 2^j , where j is an integer. The first scale of wavelet transformation is obtained from a set of differences that represents the variation of the data vector at various locations. The data points are paired together and one member of each pair is subtracted from the other member of the pair to obtain a data vector that is half the length of the original data set. The members of this vector are referred to as first scale wavelet coefficients. The data pairs are also added together to produce a vector referred to as the father wavelet coefficients. This first set of coefficients is referred to as the first scale Haar wavelet coefficients and are calculated by Equations 5.6 and 5.7 where y is the original data set.

First Scale Haar Wavelets,

$$d_{j-1,k} = \alpha(y_{2k} - y_{2k-1}) \quad (5.6)$$

First Scale Haar Father Wavelets,

$$c_{j-1,k} = \alpha(y_{2k} + y_{2k-1}) \quad (5.7)$$

The factor α is a multiplier to conserve energy in the equations so that the norm of the fully scaled vector is the same as the original data vector. The second scale of the wavelets is obtained by using the first scale father wavelets. These are calculated by Equations 5.8 and 5.9.

Second Scale Haar Wavelets,

$$d_{j-2,k} = \alpha(c_{j-1,2k} - c_{j-1,2k-1}) \quad (5.8)$$

Second Scale Haar Father Wavelets,

$$c_{j-2,k} = \alpha(c_{j-1,2k} + c_{j-1,2k-1}) \quad (5.9)$$

This method can be continued until the highest scale possible is reached and the wavelet and the last vector contain only one element.

To do the inverse transform, the process is reversed to go from one scale to the previous scale of father wavelets until the original data is obtained. This process is shown by equations 5.10 and 5.11.

$$c_{j-1,2k} = (c_{j-2,k} + d_{j-2,k})/2\alpha \quad (5.10)$$

$$c_{j-1,2k-1} = (c_{j-2,2k} - d_{j-2,k})/2\alpha \quad (5.11)$$

For example, if we take a data vector with eight members (1,1,3,4,9,5,1,0), we can do a complete wavelet transform and obtain eight wavelet coefficients that can be used to reconstruct the original set. For energy conservation, a multiplier $\alpha = 2^{-1/2}$ is used. The wavelet coefficients vector obtained would be $(0, \sqrt{2}/2, -2\sqrt{2}, -\sqrt{2}/2, 5/2, -13/2, 3\sqrt{2}/2, 12\sqrt{2}/2)$. Both the vectors have a norm of 134 which confirms the conservation of energy in the transform is correct. A graphical representation of the wavelet transform is presented in Figure 25.

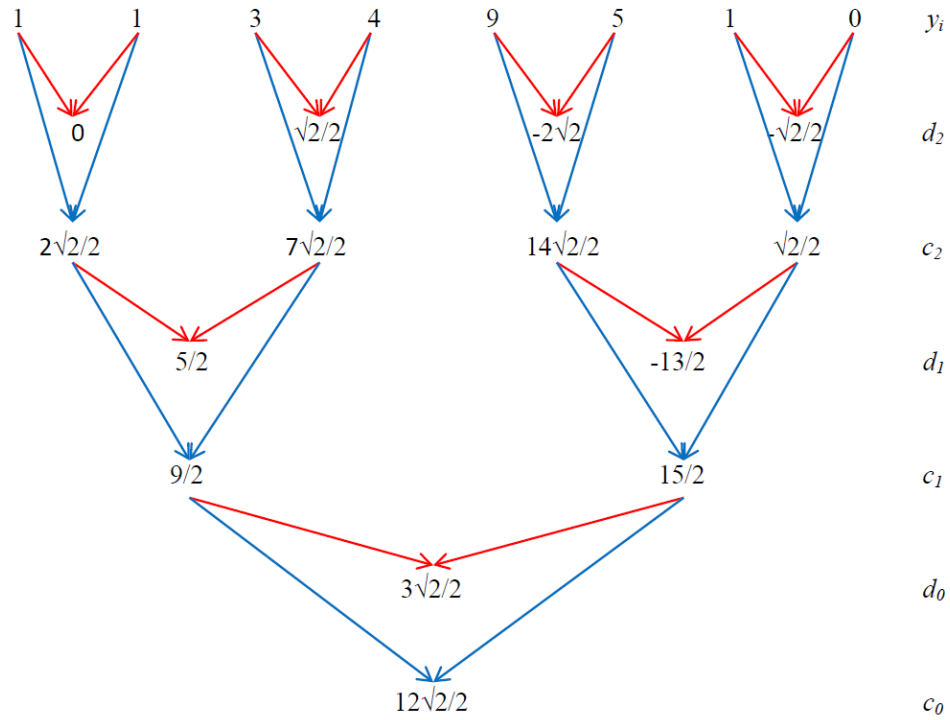


Figure 25: Graphical depiction of wavelet transform. Red arrows denote a subtraction, while blue arrows denote an addition.

In order to de-noise the data after the forward wavelet transform has been applied to the data, a filter is used to remove coefficients above a specified threshold. The coefficients are then adjusted, based on either a hard or a soft threshold. With a hard threshold, the coefficients that fall below the threshold are set to zero. For a soft threshold, coefficients that fall below the threshold are also set to zero, but in addition wavelet shrinkage is used to decrease coefficients that are outside the threshold by the amount of the threshold. Hard and soft thresholding are represented by Equations 5.12 and 5.13, where d_k denotes the wavelet coefficients and λ denotes the threshold.

$$d_{k \text{ hard}}(d_k, \lambda) \equiv \begin{cases} d_k & \text{if } |d_k| > \lambda \\ 0 & \text{otherwise} \end{cases} \quad (5.12)$$

$$d_{k \text{ soft}}(d_k, \lambda) \equiv \begin{cases} \text{sign}(d_k)(|d_k| - \lambda) & \text{if } |d_k| > \lambda \\ 0 & \text{otherwise} \end{cases} \quad (5.13)$$

The modified wavelet coefficients are then used in the reverse transform to obtain the de-noised data set.

For the wavelet de-noising applied to the digitized data for the NDP detection system, the Matlab wavelet analysis program was used to determine appropriate threshold values for the coefficients of a representative pulse and then to generate a function, which was applied to the entire data set.

The data presented in Figure 26 show the effectiveness of wavelet de-noising for removing the noise from a signal.

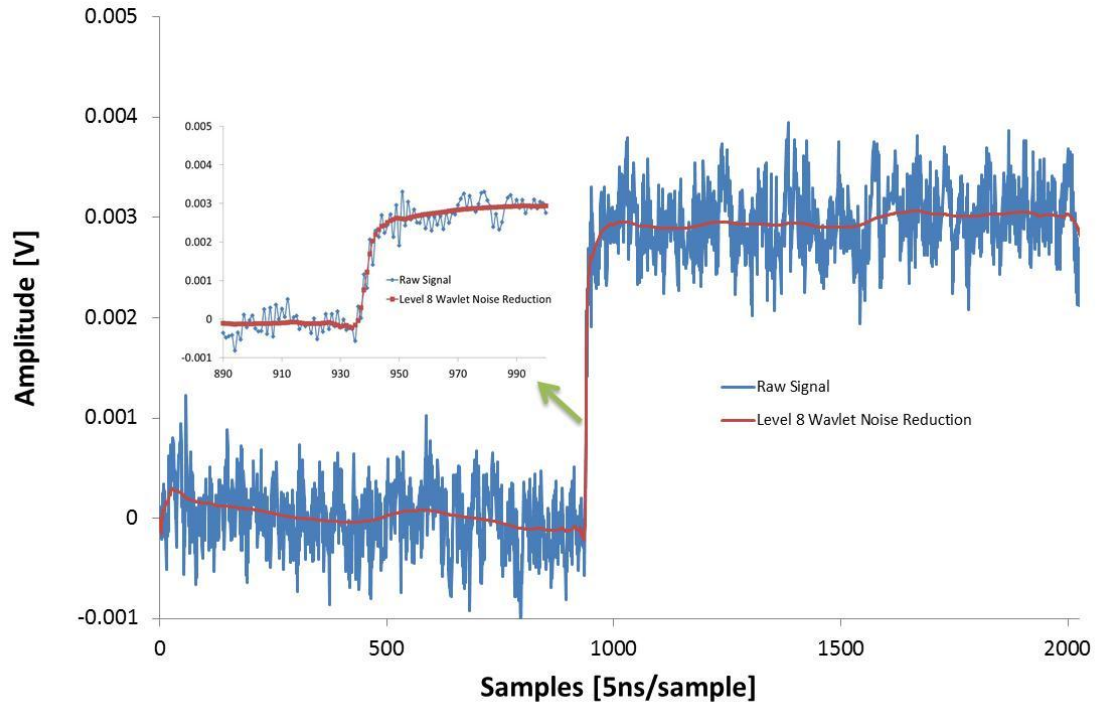


Figure 26: De-noised digitized pulse using level 8 Haar Wavelets with hard thresholds optimized to remove random noise.

An important result from these data is that unlike the smoothing that was done through the previous methods, the characteristics of the signal in the time domain have been preserved. This makes it possible to determine much more accurately the true shape characteristics of the signal.

After the wavelet de-noising, rise-time measurements were performed on the conditioned data. For illustrative purposes it will be assumed that the rise time is the time it takes for the signal to go from 10 to 90 percent of its maximum amplitude, although depending on the data it may be useful to use different values.

The algorithm used in this work was based on calculating the 10 and 90 percent levels from the baseline value and the peak value for the signal. Using these values, the corresponding (x,y) data in the signal were determined and the time difference was calculated.

Because the data are discretized, the calculated 10 and 90 percent levels usually did not fall on actual data points in the signal and it was therefore necessary to extrapolate between the two nearby data points to achieve a more accurate estimate.

The rise-time algorithm was programmed in Matlab using the steps listed below. The Matlab code is presented in the Appendix.

- 1) Find the minimum and maximum values for the signal, and calculate 10% and 90% values between minimum and maximum.
- 2) Start at beginning of signal and step forward through the data iteratively until a point that is equal or greater than 90% value is found. If the point is greater than the 90% value linearly extrapolate between it and the previous data point to find the corresponding index value for 90% of maximum; otherwise use the index of the point for 90% value.
- 3) Start at the data point found in step 2 near the 90% value and step backward until a point that is less than or equal to 10% value is found. In a manner analogous to that in step 2, extrapolate to find corresponding index for the 10% value.
- 4) Take the difference between the 90% and 10% value corresponding indices and calculate time difference. For the case of the GaGe Digitizer the sample

rate was 200MS/s. Therefore the time between consecutive samples is 5 ns, so to find the rise time in ns multiply the difference by 5.

The process used to determine the rise time is illustrated in Figure 27. The reason the 10% value is skipped while stepping forward and then found by stepping backward from the 90% level is to increase the accuracy of the measurement for low-level signals with a large signal-to-noise ratio.

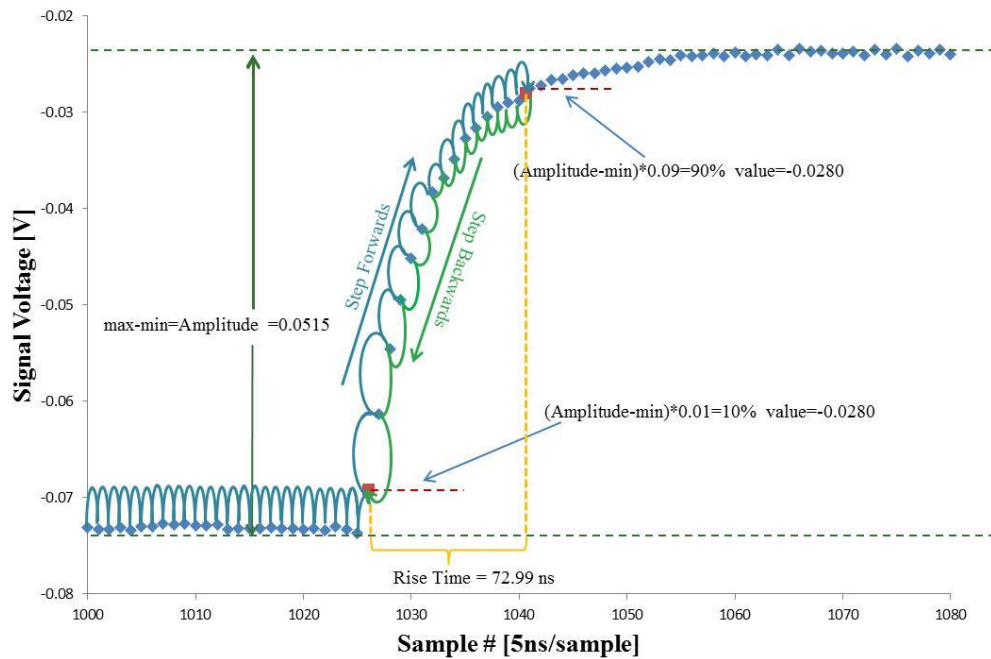


Figure 27: Rise time measurement

5.4.4 Dead Time Correction

For a detection system to make quantitative measurements it is essential that dead-time effects are properly understood and accounted for in the overall measurement. Two simple models are usually used to describe dead-time effects in a counting system. These are referred to as paralyzable and non-paralyzable detector response. For the simplest case it is assumed that there is a fixed time during each detector event for which the detection system is unable to capture an event that occurs within this time period. This is usually a combination of the detector and the rest of the signal processing chain.

For a non-paralyzable detection system the detector is unable to capture a new event for a fixed amount of time after each event. A Geiger tube is an example of a detector that has this response characteristic. Therefore any events that occur during this period are lost.

With a paralyzable system, there is also a dead period between detector events, but in addition if an event occurs during this period the dead time is increased for an additional amount of time as a result of the second event.

For both models, if the dead time associated with each event is fixed, the dead time as a function of count rate can be easily determined by Equations 5.14 and 5.15, where n is the true interaction rate, m is the measured count rate, and τ is the dead time associated with each individual event.

Non-Paralyzable,

$$n = \frac{m}{1-m\tau} \quad (5.14)$$

Paralyzable,

$$m = ne^{-n\tau} \quad (5.15)$$

For the NDP spectroscopy system with the digitizer and hardware triggering, the fixed trigger threshold value of the digitizer board is unable to trigger until the previous pulse has decayed below the threshold. There can also be pile-up pulses that occur during the decay of the previous pulse. The signal will not decay below the threshold until these additional pulses have decayed as well.

Since the decay time is dependent on the preamplifier, the initial assumption was that this system should follow a paralyzable model; however, experimental data showed that this was not the case. An examination of individual pulses showed that the high-intensity, low-level background inherent in the NDP facility resulted in a large number of trigger events from pulses that were just below the trigger threshold. Because of the random noise fluctuations in the signal, a large number of the pulses that are below the threshold are captured when the noise level momentarily spikes above the threshold. Since the peak of these pulses is already below the threshold, and the rearm time for the board is less than 2 μ s, the board is almost instantaneously ready to trigger again. This leads to a large deviation from the paralyzable detection model, in which all pulses are assumed to have the same decay constant, and therefore

a determination of dead time based on decay time and the number of pulses observed was not possible.

Instead, the dead-time correction was determined from individual measurements on a pulse-by-pulse basis, which was made possible by the complex trigger and time-stamp capabilities of the digitizer. The complex trigger capabilities on the GaGe digitizer consist of two trigger engines per channel which can be set independently to trigger on a specified trigger threshold, with a rising or falling slope, and can be set to trigger on either or both input channels. In order to use the trigger capabilities to measure the decay time for each pulse, one trigger engine was set to trigger on a rising slope to capture the start of the pulses, and another trigger engine was set to trigger at the same level only with a negative slope to capture the tail of the pulse as it decayed below the threshold. Using the differences in the trigger time stamp for the start and end of decay, the decay of each pulse was accurately measured.

In addition, a small adjustment was made for pulses that did not result in a significant decay time, and also for each negative trigger event. For these pulses there is a small amount of time lost due to the number of samples collected for each trigger event and the trigger rearm time, which had to be added into the overall system dead time.

Because the digitizer board did not have any way to distinguish between trigger events it was necessary to analyze the data from each trigger event to determine whether it was from a rising slope or a falling slope. This was done by taking an average of the digitized signal for some of the pre-trigger and post-trigger data and

then taking a difference. Therefore, if a positive trigger event was followed by another positive trigger event, this would mean that the previous trigger event did not result in a signal above the trigger threshold after the specified number of pre-trigger and post-trigger samples had been collected. In this way, these pulses could easily be separated from those that increase the dead time due to their decay time.

In order to verify that the dead time measurement was accurate, the output from the preamplifier was connected to both the DSPEC and the digitizer simultaneously during the series of measurements.

The first measurements were taken with a $^{239}_{94}\text{Pu}$ source in front of the surface barrier detector. A series of 10 measurements was taken, counting 400 seconds for each. This was sufficient time to obtain approximately 11,000 counts in the $^{239}_{94}\text{Pu}$ peak. The data for these measurements are presented in Figure 28.

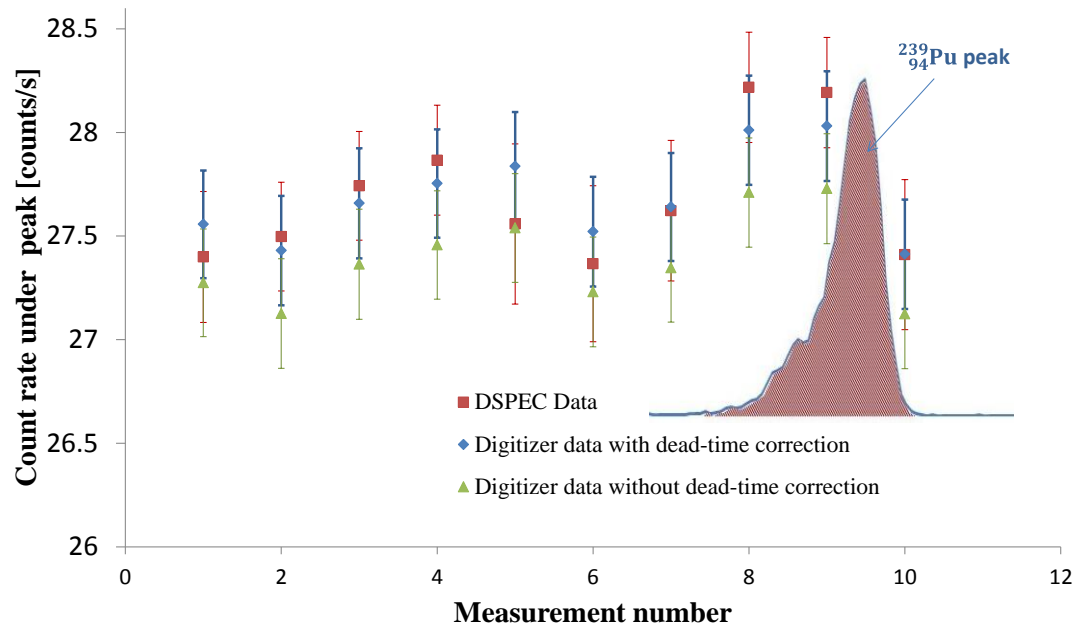


Figure 28: Dead time verification using $^{239}_{94}\text{Pu}$ check source (Real time was 400 s)

From these measurements it was clear that the dead time correction matched the DSPEC data within the uncertainty of the measurements.

Since the count rate of the $^{239}_{94}\text{Pu}$ source was relatively low and this was not an NDP measurement, the correction was small and it was not necessary to sort out many of the low-level pulses with short decay times. Therefore, to verify that the dead time measurement was accurate for higher count rate NDP applications, a series of measurements was performed on a large boron-implanted silicon wafer. To maximize the count rate the wafer was placed in the beam without a Teflon aperture. Similar to the $^{239}_{94}\text{Pu}$ source a series of 10 measurements was taken counting for 400 seconds each. This was sufficient time to obtain approximately 27,000 counts in the main alpha peak. The data for these measurements are presented in Figure 29. Again these data matched well with the DSPEC data even though the pulse decay dead-time correction was fairly significant for these measurements. For most NDP measurements the dead-time would likely be significantly less and therefore this method of determining the dead time should be sufficient.

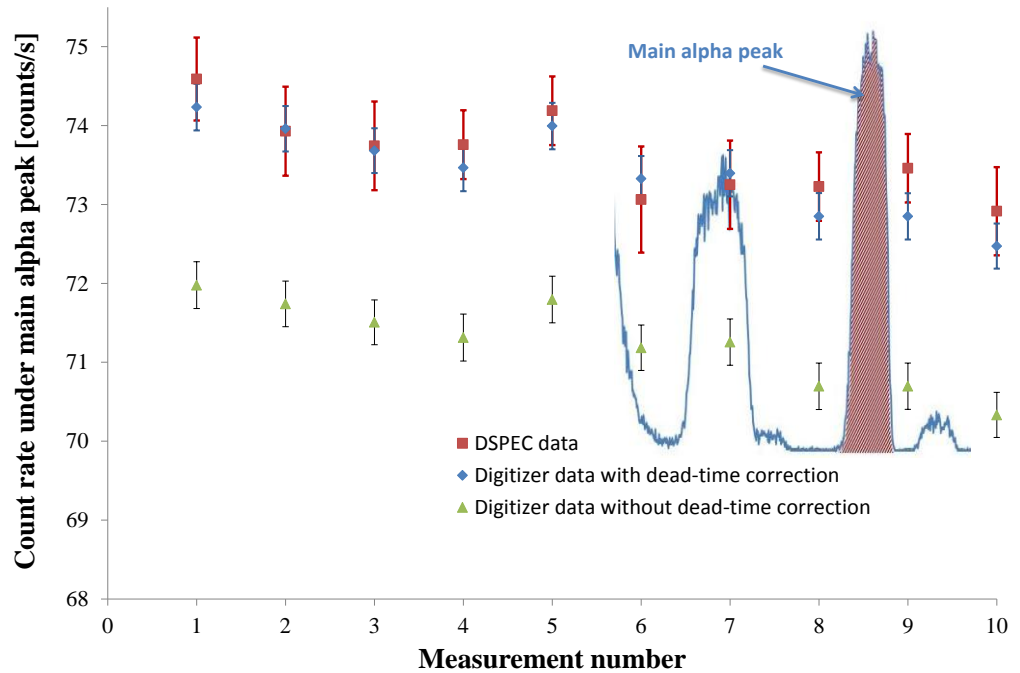


Figure 29: Dead time verification using boron implanted silicon wafer (Real time was 400 s)

6. Results and Data Analysis

6.1 Energy Calibration

In order to accurately determine the concentration as a function of depth for an NDP analysis it is essential to have a correct energy calibration. Because the energy calibration is dependent on many factors within the NDP facility, especially the detectors, it is important that this be done on a regular basis, as well as whenever system changes are made such as changing detectors or other components in the spectroscopy chain.

One of the standard ways of performing the energy calibration is by use of a NIST reference standard in which an NDP analysis is performed on the standard and based on the features in the resultant energy spectrum the energy calibration is calculated. For this facility, the NIST Standard Reference Material 93a (Borosilicate Glass 12.5% B_2O_3) [35] was used by measuring the energy of the ${}^4_2\text{He}$ and ${}^7_3\text{Li}$ particles produced from neutron capture in ${}^{10}_5\text{B}$. The standard procedure when using this for NDP calibration is to break the glass so that the surface exposed to the beam facing the detector is very smooth. This ensures that the concentration is uniform on the surface and that irregularities in the surface do not affect the analysis.

Because the concentration is uniform throughout the sample and the sample is much thicker than the mean free path of the ${}^4_2\text{He}$ and ${}^7_3\text{Li}$ particles, and since these particles originate with discrete energies, the resulting spectrum has a step shape with a constant height all the way back to the lowest energy measured by the detector.

These step shapes correspond to the discrete energy of the charged particles produced within the sample.

Since the charged particles are emitted at equal energies, the steps are a result of charged particles produced from all different depths within the sample. If, for example, all the charged particles were produced at the surface of the sample, the energy deposited in the detector would correspond to the initial energy of the charged particles. The result would be a spectrum with peaks associated with the discrete energies of the charged particles. We know from counting statistics that for a sample size greater than 20, the shape of each peak should fit a Gaussian distribution due to the random fluctuations in the energy deposited within the detector. Thus, for the case of a sample in which particles are emitted evenly throughout the sample, the ideal spectrum should be a sum of an infinite number of infinitely closely spaced Gaussian shapes resulting from the emission of particles at different depths within the sample.

A plot of this is depicted in Figure 30.

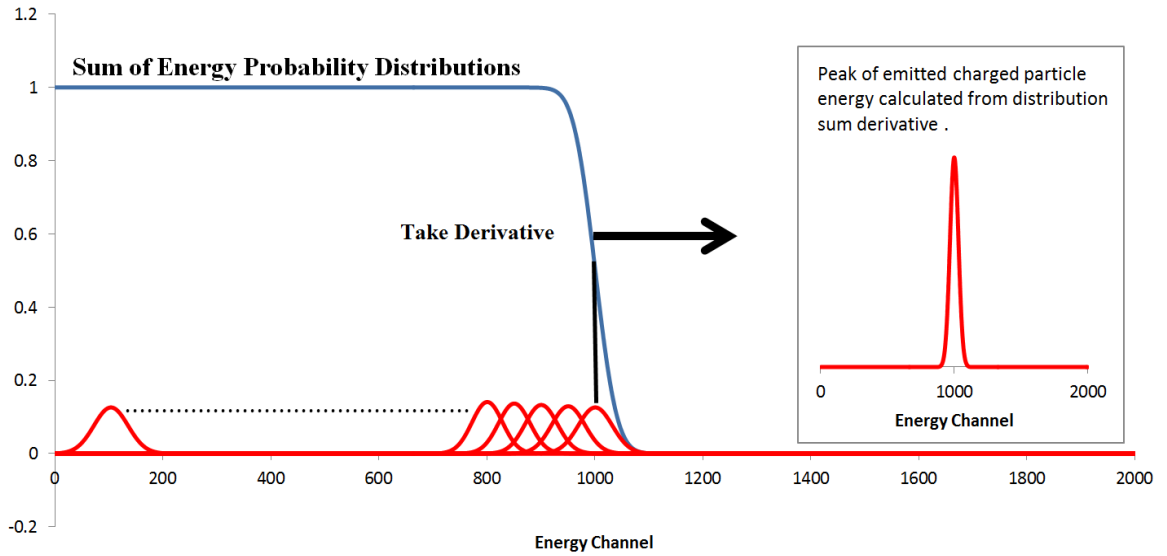


Figure 30: Energy distribution for a single charged particle energy emitted uniformly throughout a thick sample.

It can be shown that for a spectrum as described in Figure 30 the maximum energy corresponds to an inflection point of the step function. Therefore, since this is also the point with the steepest slope, the absolute value of the derivative of this function will result in a peak that corresponds to the maximum energy of the particles as demonstrated to the right of the figure.

When performing the energy calibration for the new NDP facility, it was found that to accurately choose the inflection point it was necessary to smooth the data or fit a function to the data, which could then be used to find the inflection point. One function which fits this shape fairly well is a sigmoid function [36]; however this requires a separate fit to be made for each step in the spectrum.

An improved method of finding this inflection point was developed in this work. First Haar Wavelet smoothing was used to smooth the data. An example of this is shown in Figure 31.

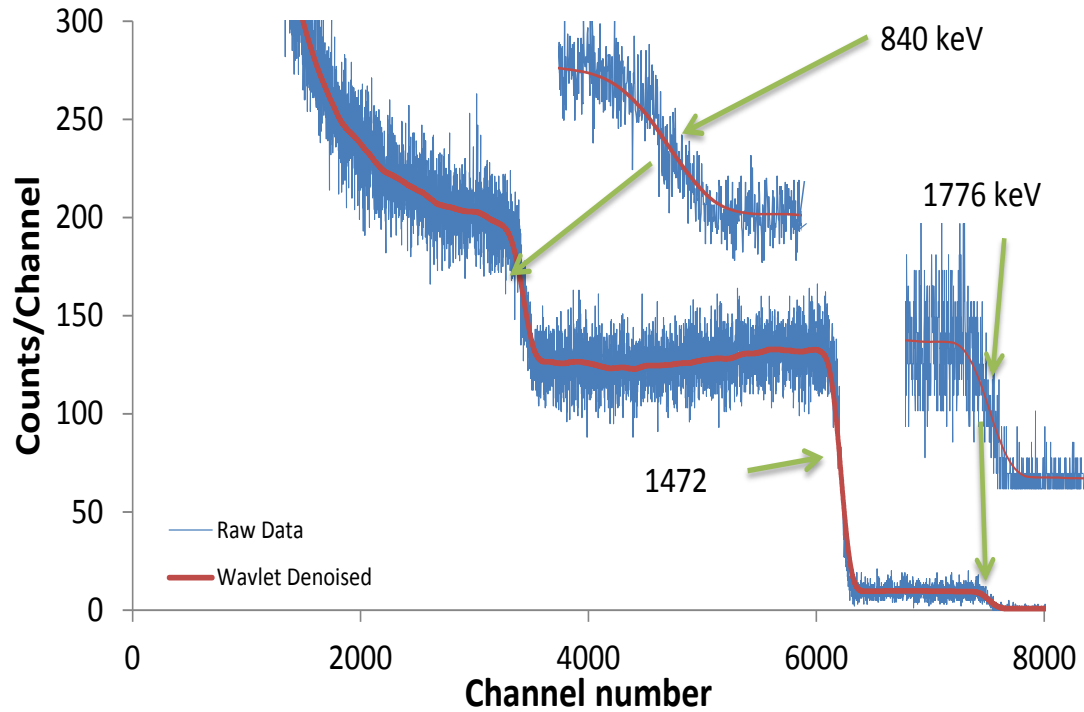


Figure 31: NIST Reference Standard 93a NDP spectrum taken with the OSTR NDP Facility (Real time 10800 s)

Even though the above spectrum was counted for only 3 hours, it is a good demonstration of how well wavelet transforms work to smooth data with large amounts of random noise. After smoothing this data with the wavelet transforms, a derivative was approximated by taking the difference between successive data points. The result of this is presented in Figure 32.

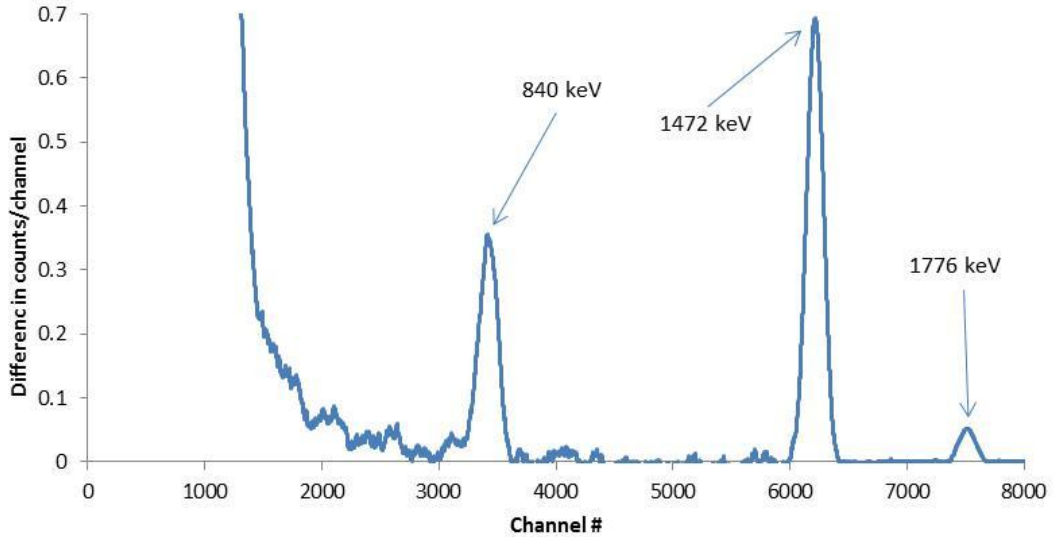


Figure 32: Approximated derivative of wavelet smoothed data from Figure 31

Using the peak values from Figure 32 as the maximum energy for the alpha and ${}^7_3\text{Li}$ particles, an energy calibration as a function of channel number was calculated from a least-squared linear fit. The resulting energy calibration is presented in Figure 33.

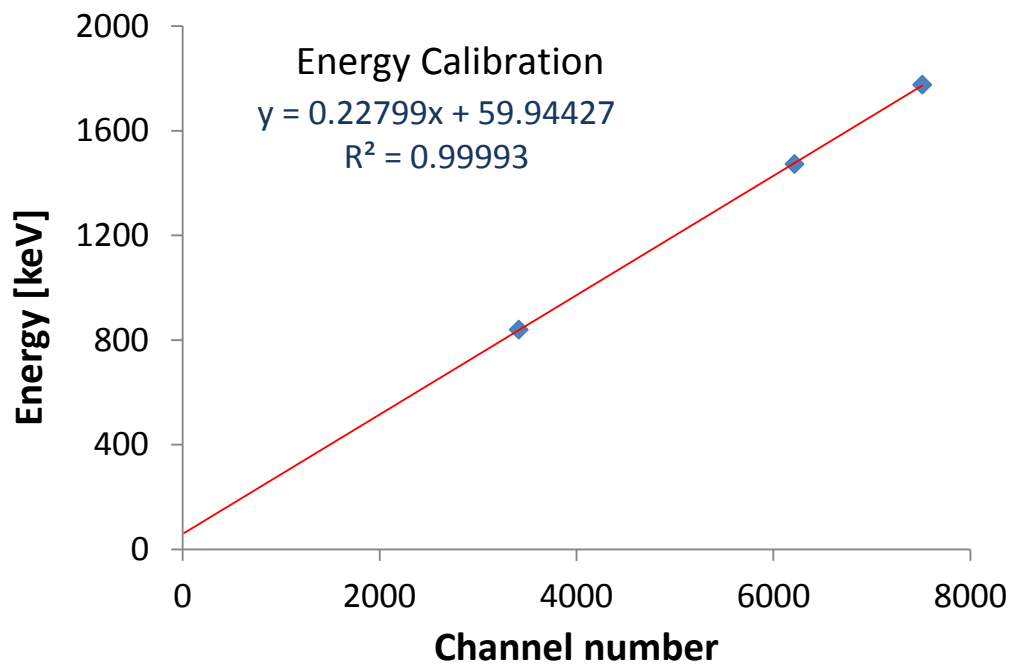


Figure 33: NDP energy calibration obtained from NIST 93a reference standard

One of the advantages of using this method over other methods, such as manually fitting a sigmoidal function to the step curves, is that a program can easily be developed that will automatically do the wavelet smoothing, calculate the differences between the smoothed data, calculate the peaks and determine the energy calibration fit.

6.2 NDP-PGNAA Measurements

One of the unique capabilities of the OSTR NDP-PGNAA facility is its ability to perform both NDP and PGNAA analysis simultaneously. This is the first facility in which this capability has been implemented.

The advantages of this facility over other PGNAA and NDP facilities is the synergy between the two methods, which can increase the information obtained during a measurement, as well cross-calibration techniques which can increase the accuracy of the measurement and reduce the need for specialized NDP standards.

A good example of this is the energy calibration used for the NDP measurement. In the past with other facilities it has been necessary to have a specialized NDP standard with a known concentration of the isotope of interest in the near surface regions of the sample. A common standard would be boron implanted in a single-crystal silicon wafer for which a NDP analysis is performed and the observed count rate is used to calibrate the facility for counts per concentration per cubic volume of boron.

Some of the challenges with this type of analysis are obtaining the needed standards and the need to recalibrate the system when facility changes are made, such as changing or moving the position of the detectors relative to the sample. However, with the PGNAA capability built into the same facility, depending on the sample characteristics, the quantitative concentration can be determined from a PGNAA measurement and the concentration profile can be determined with a NDP measurement. An example that was performed with this facility was the concentration

profile in a small single-crystal silicon wafer with boron deposited in the first micrometer of the surface.

In preparation for this measurement the PGNAA facility was calibrated with a filter-paper boron standard. The filter-paper standard was prepared by dripping a liquid boron standard with a known amount of boron onto the filter paper and sealing it in a Teflon pouch. The Boron standard was then used to determine the correct count rate relative to boron concentration for the PGNAA facility by taking a series of PGNAA measurements and averaging the results. The results from these measurements are presented in Figure 34.

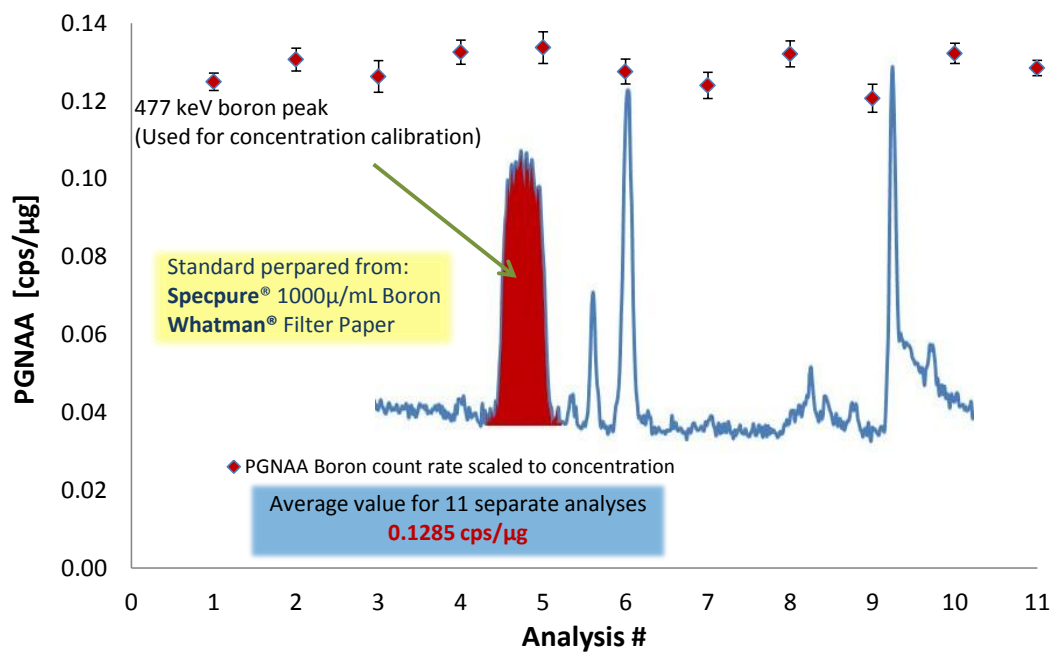


Figure 34: PGNAA boron standard calibration

After the PGNAA facility was calibrated a PGNAA and NDP combined analysis was performed on the boron-implanted (1.3 cm by 1.5 cm) silicon wafer. Because the

goal of this measurement was to determine the correct scaling factor between the NDP and PGNAA spectroscopy measurements, the sample was placed in the neutron beam without a Teflon aperture so that the NDP counts and PGNAA counts would be proportionally correct.

The resulting PGNAA spectrum was then used along with the data from the calibration standard to determine the overall concentration of boron in the silicon wafer, and the NDP spectrum was used to determine the concentration profile of boron within the silicon wafer.

The stopping power data for the concentration profile were calculated using SRIM (Stopping and Range of Ions in Matter) [37], and a polynomial fit of this data was used to determine the depth range for each discretized energy level from the NDP spectrum. The data calculated from SRIM are presented in Figure 35.

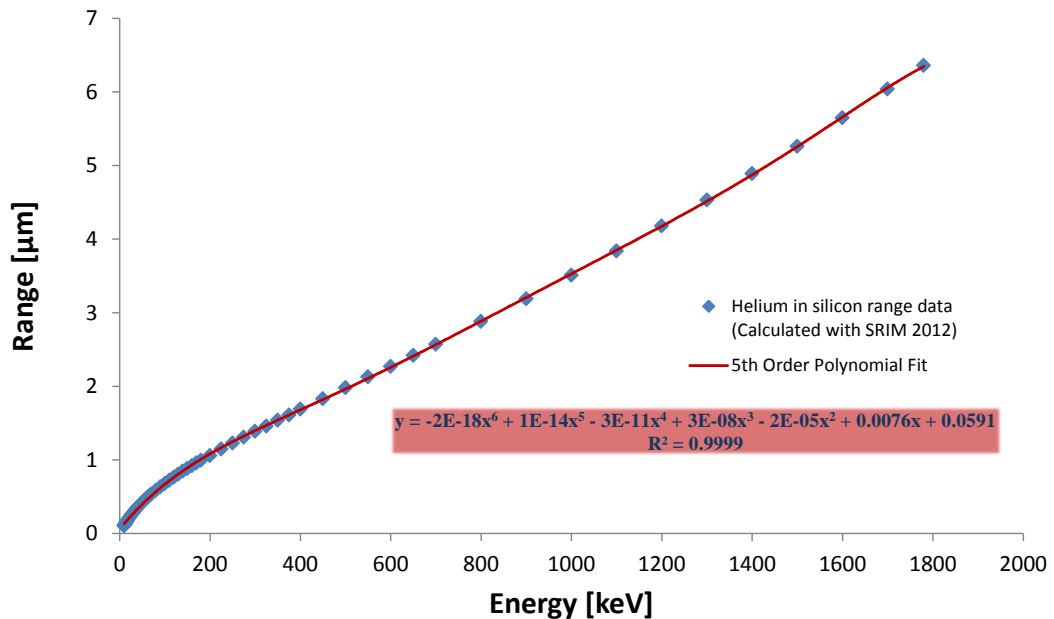


Figure 35: Helium in silicon stopping power data (calculated with SRIM 2012)

The boron concentration as a function of depth for the sample was calculated using the total boron concentration measured with the PGNAA facility, the stopping power profile calculated from the SRIM data and the NDP spectra.

To verify the calibration, the resulting data were compared with an analysis of the same sample which was performed with the NDP facility at the National Institute of Standards and Technology (NIST). The data for both of the measurements are presented in Figure 36.

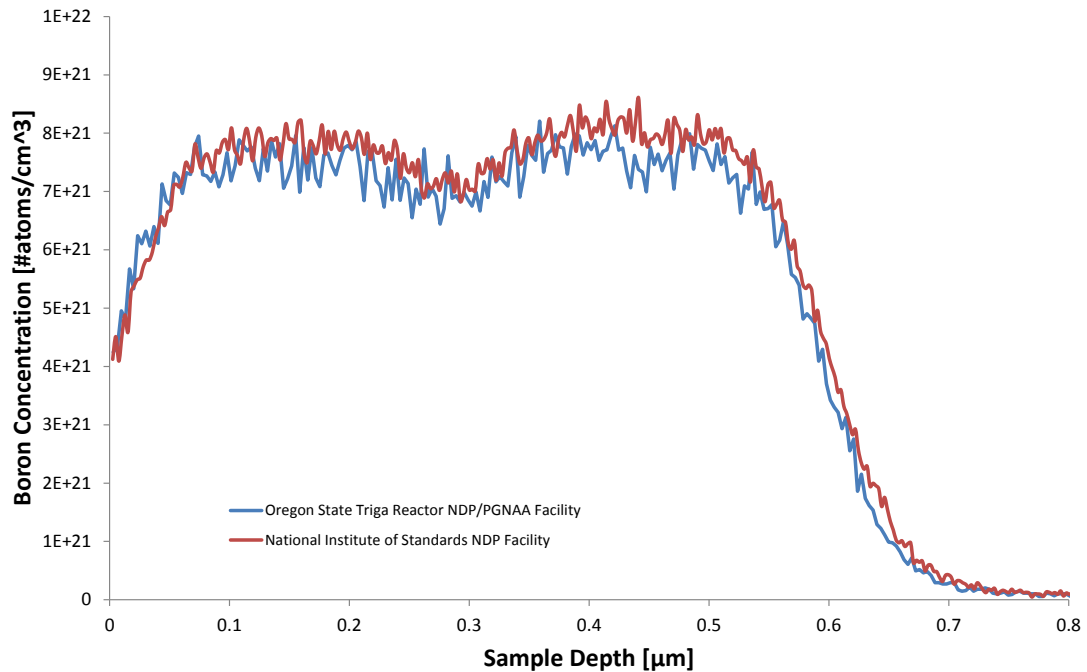


Figure 36: Boron implanted silicon NDP measurement. Measurement was performed at the NIST NDP facility and the OSTR NDP/PGNAA facility.

The results from the two measurements demonstrated good agreement between the NIST NDP facility and the OSTR NDP/PGNAA facility. The difference between the two measurements was about 4%, with the measured concentration from the OSTR facility lower than the result of the NIST measurement. Many factors could lead to this

difference; however, since the boron standard measurements presented in Figure 34 fluctuate by as much as 8%, the difference is well within the expected precision for the measurement.

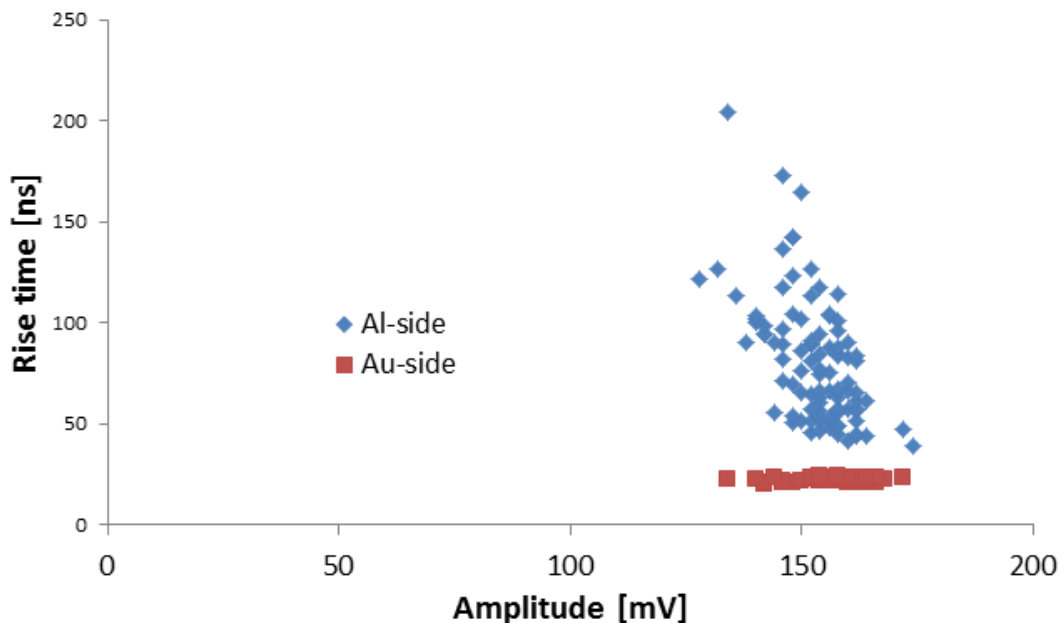
6.3 Rise-Time Analysis

As mentioned in the Section 5.3, the main factors that contribute to the rise-time response of surface-barrier detectors are electron and hole drift velocities, plasma effect, trapping, de-trapping, and recombination. To explore the effects of these mechanisms and to analyze their possible benefits to NDP based on rise time criteria, they were studied in a series of measurements which is presented below.

For standard charged-particle detection, the detectors are oriented so that the incident particles interact with the side of the detector that has the rectifying contact. This is the side with the heavily doped layer, which is either p-type or n-type depending on whether the silicon is weakly n-type or p-type. This occurs because the depletion region extends into the detector wafer from the rectifying contact, and for the case of a fully depleted detector this depletion region extends completely across the detector. Since the electric field strength falls off linearly moving away from the rectifying contact, we should expect an increase in the rise time for particles interacting on the backside of the detector, assuming the voltage is low enough [31]. In addition the rise time can also be effected by the difference in the electron and hole drift velocities. Since holes drift through the detector at roughly half the speed of electrons if the electron hole pairs are created close to the negative side of the detector as opposed to the positive side of the detector, the charge collection time will be increased because of the slower drift velocities of the holes.

The application this could have for an NDP analysis would be to filter out the detector response from particle interactions with the detector side away from the sample or in the weakly depleted regions of the detector. For example since heavy charged particles will deposit energy over a short range as opposed to gamma rays which have a much longer range in materials, depending on the side of the detector for which the radiation is incident on, there may be differences in the rise times for the different radiation types.

Using a Tektronix TDS 220 oscilloscope, initial measurements of rise time were measured of alpha emissions from $^{239}_{94}\text{Pu}$. The results from this measurement are presented in Figure 37. The detector used was the TP-50-50-15-NH, the specifications of which are given in Table 1, operating at a bias voltage of 35 volts. These preliminary measurements showed there was a considerable difference in rise times for alpha particles striking the rear side of this detector.



Based on the results above, it was concluded that there may be a reduction in the high count rate of the background if all pulses with rise times greater than the standard rise times were rejected for a standard NDP analysis, especially if neutron and gamma rays interacting in the far side of the detector have the same effect. To explore this hypothesis and to provide rise time analysis capabilities to the facility, a code was written using Matlab to measure the rise times for each detector response of the digitized data from the digital signal processing system discussed in Section 5.2. Due to reactor scheduling and the fact that this system took considerable time to setup, testing of this system was done outside of the NDP facility and later added to the facility.

The initial spectral measurements were carried out with the AlazarTech digitizer mentioned in Section 5.2. The digitizer was programmed and configured with Matlab to operate with characteristics similar to a standard oscilloscope to trigger if the input signal connected to the output of the amplifier rose above a specified level. This trigger level chosen was just above the noise level or fluctuations in the baseline to prevent false trigger events. When a trigger event occurred, 2,048 samples of the input signal were recorded, with 1024 of these being pre-trigger events. The AlazarTech digitizer operating at 180 MS/s was enough to capture 5.7 μ s before and after the trigger, which was enough to resolve the detail of the rising edge of the pulse, as well as enough to average the base level and peak level of the pulse in order to accurately measure the pulse amplitude.

The system was tested with both ^{226}Ra and ^{241}Am sources. The ^{226}Ra was placed facing the front side of the detector and the ^{241}Am was placed facing the back side of the detector. The measured rise-time for each pulse was recorded and used to generate a plot of rise-time versus count rate. The plot revealed two distinct regions of differing rise time. The region with the longer rise times came from particles interacting on the back side of the detector. This effect is most likely due to the plasma erosion time resulting in a momentary breakdown of the potential within the detector.

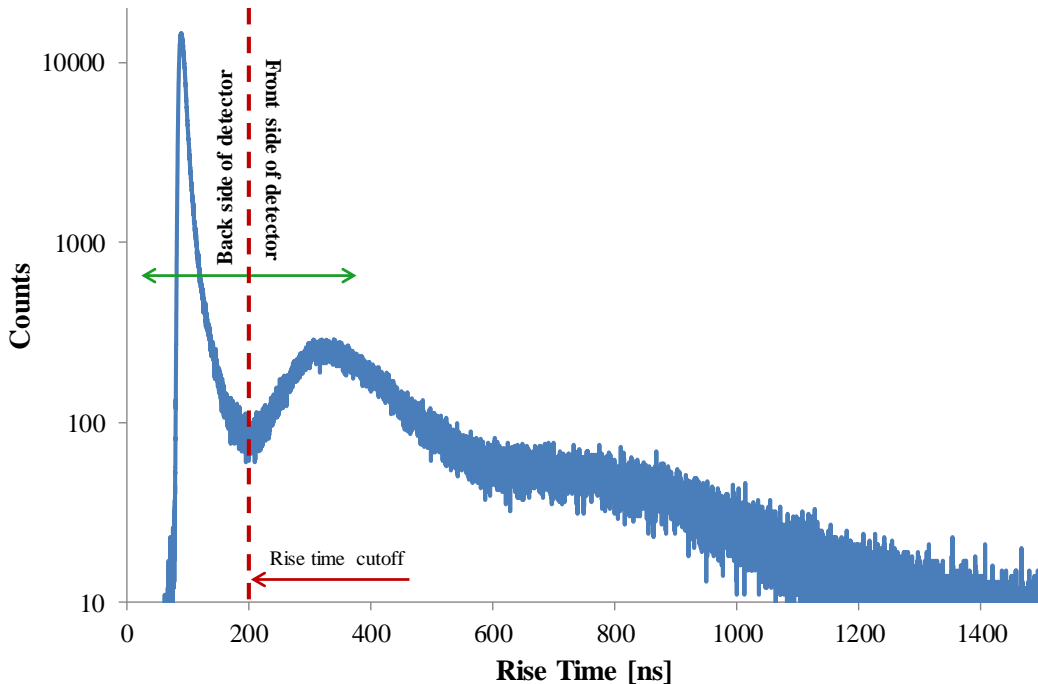


Figure 38: Pulse rise time measurement for surface barrier detector. This data was taken with ^{226}Ra source facing the front side of the detector and ^{241}Am source facing the back side of the detector. The longer rise times are due to alpha particles incident on the back side of the detector.

Based on the plot shown in Figure 38 a threshold was used to identify pulses that had a rise time above the threshold level. Using the threshold level determined from Figure 38, separate pulse amplitude histograms were generated for pulses with rise-

times above the threshold and those with rise times below the threshold. The results for these both with and without the rise-time discrimination are presented in Figure 39. These results showed a clear separation between the $^{241}_{95}\text{Am}$ alpha particles from the front side and the $^{226}_{88}\text{Ra}$ particles from the back side of the detector.

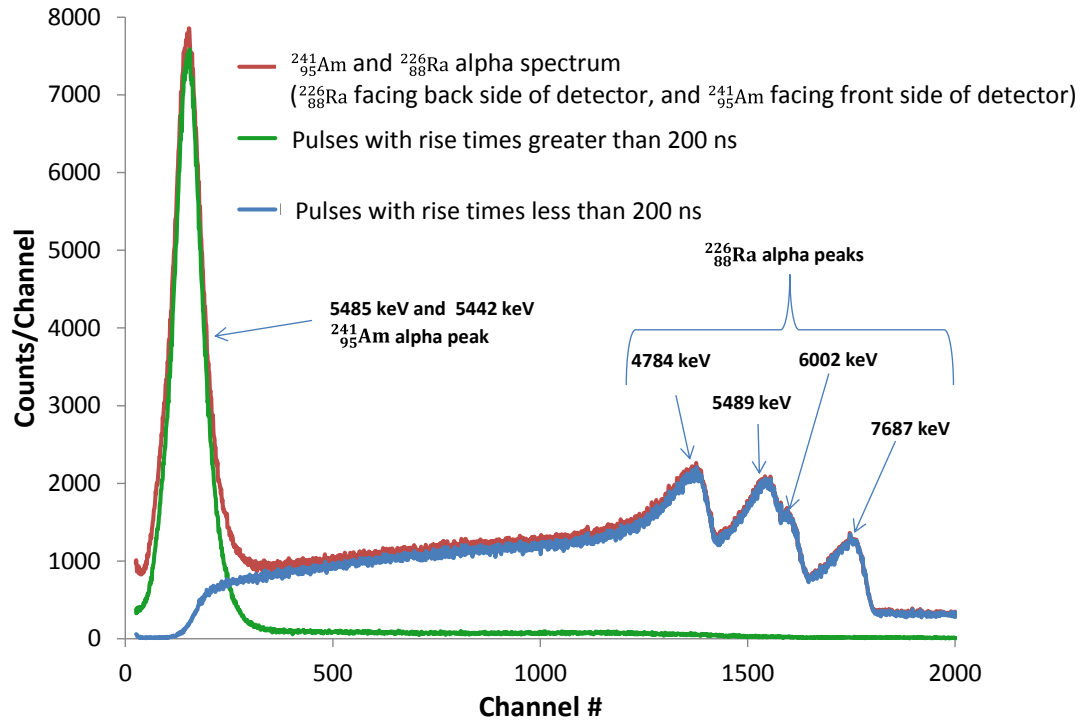


Figure 39: Pulse height histogram for surface barrier detector with rise time discrimination. This data was taken with $^{226}_{88}\text{Ra}$ source facing the front side of the detector and $^{241}_{95}\text{Am}$ source facing the back side of the detector.

The results from these data verified the rise time measurement with the digitized system work correctly for pulse rise time analysis. However, additional measurements with this detector for NDP analysis did not reveal any significant differences in rise times for NDP measurement for which both gamma and charged particles are incident on the detector. The results from these measurements are presented Figures 40 and 41. The data in Figure 40 demonstrate the effectiveness of wavelet smoothing to increase

the accuracy of the rise time measurement. The smoothing is especially important for low amplitude signals with a low signal to noise ratio.

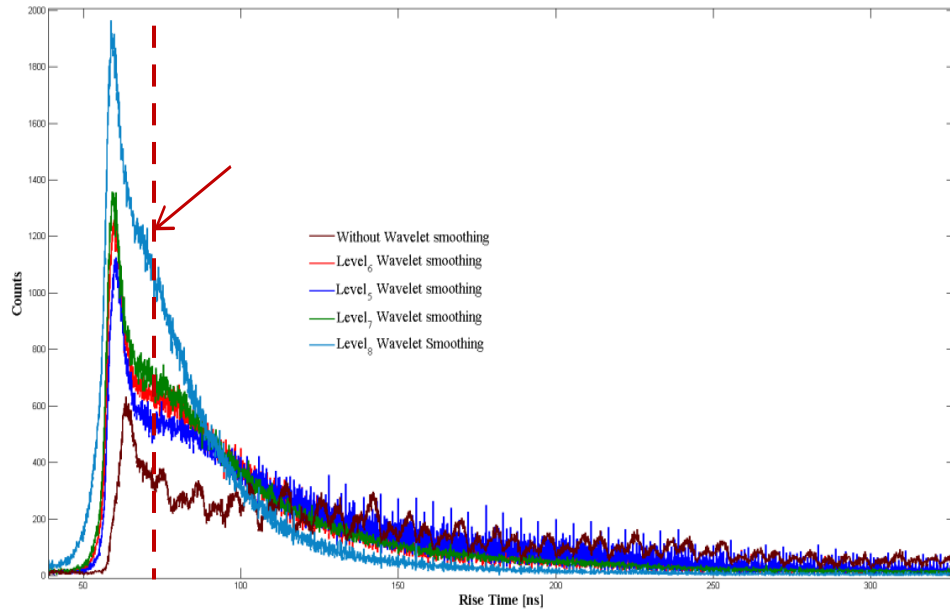


Figure 40: Rise time measurements for boron implanted silicon wafer with surface barrier detector TP-50-50-15-NH

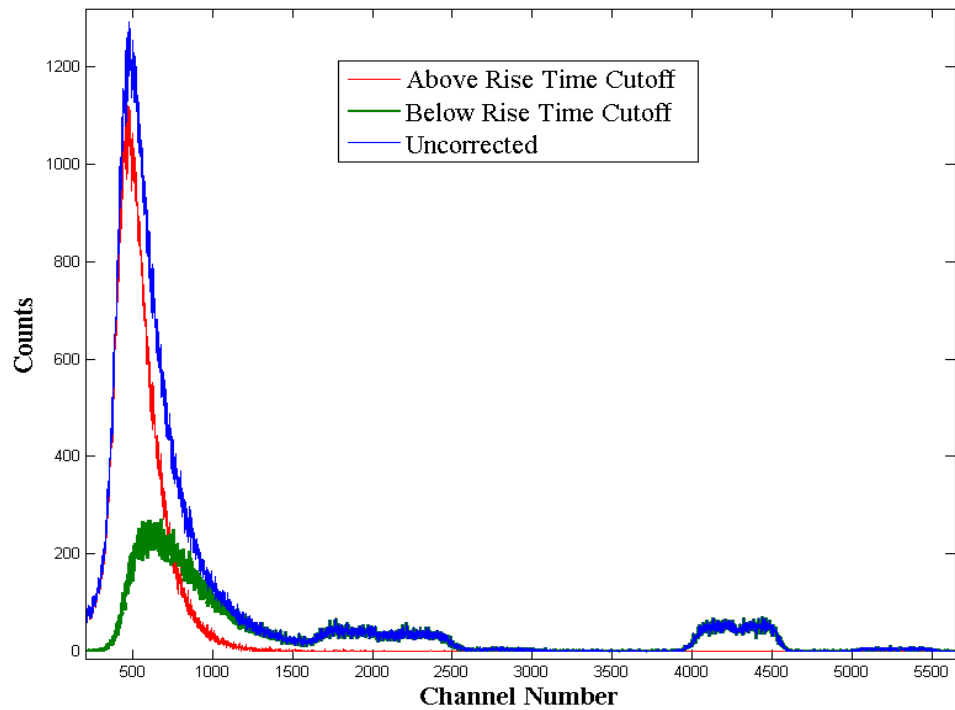


Figure 41: Rise times discrimination of boron implanted silicon wafer with surface barrier detector TP-50-50-15-NH

Also, no significant difference in rise times were observed until the operating potential was decreased to the point that the resolution of the detectors was not suitable for energy spectroscopy. As a result it was concluded that the plasma effect was not great enough to distinguish between the different types of radiation incident on the detector during a NDP measurement at the operating potentials required for the necessary energy resolution.

From these measurements it can be concluded that if there is any rise time effect useful for NDP measurements it would be due to the difference in the charge collection time of the electrons and hole-pairs.

The surface-barrier detectors used were made from n-type silicon with a p-type contact and are only partially depleted detectors. As a result the front side of the detector is the positive contact and the back side is the negative contact. Therefore particles that deposit energy near the front side of the detector should result in longer rise times as opposed to particles that deposit energy in the back side of the detector. This is because the holes created on the front side will have to travel the full thickness of the detector. In addition, since the detectors are only partially depleted, particles depositing energy in the back side in the partially depleted regions will also have longer rise times due to trapping and the slower drift velocities due to the reduced potential in this region. Therefore, as a result of the type of surface barrier detector and the depletion characteristics it is understandable that rise time separation was not successful with these detectors. However if the detector were made of p-type silicon with a n-type contact, the holes created from short range particles on the front side would be expected to have shorter rise times providing plasma effects are minimal and all other interactions deeper into the detector would be expected to have longer rise times. Also, if the detector was fully depleted particles incident on the back side would result in good energy resolution as well as shorter rise times. This was verified with Passivated Ion Planer (PIP) silicon detector.

The PIP detector (model: FD 50-14-300 RG) was obtained from CANBERRA Industries. This detector was 300 microns thick and is fully depleted at the manufacture specified operating bias of 70 volts. NDP measurements were made on lithium film and a boron implanted silicon wafer. The results from these measurements are presented in Figures 42-46. For both samples the pulse rise time

histogram resulted in two peaks. The narrow peak on the left is due to the charged particles striking the detector and the peak on the right is from all other radiation striking the detector which penetrated further into the detector. These rise time plots were used to determine an appropriate rise time cutoff window to separate out the charged particles from other interfering radiation.

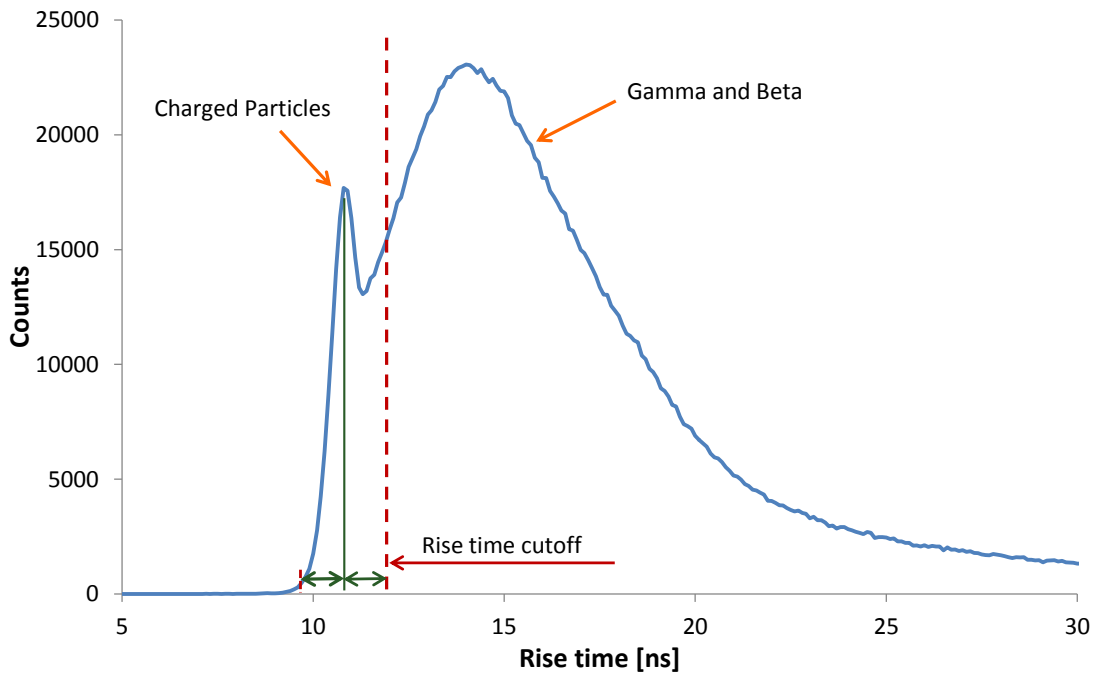


Figure 42: Pulse rise time measurements of boron implanted silicon with detector FD 50-14-300 RG

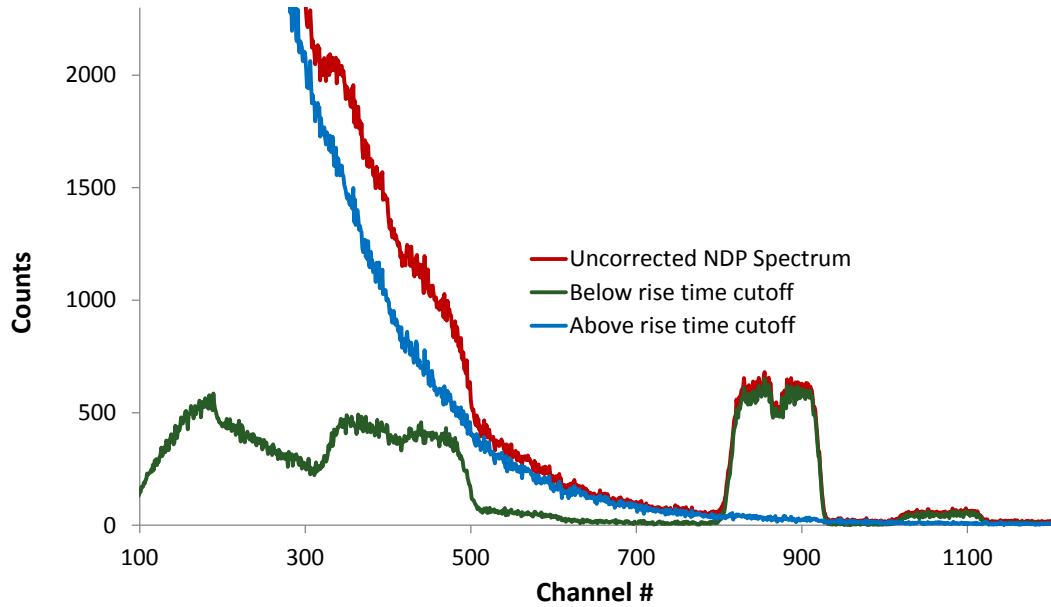


Figure 43: Rise time discrimination of boron implanted silicon energy spectrum with detector FD 50-14-300 RG

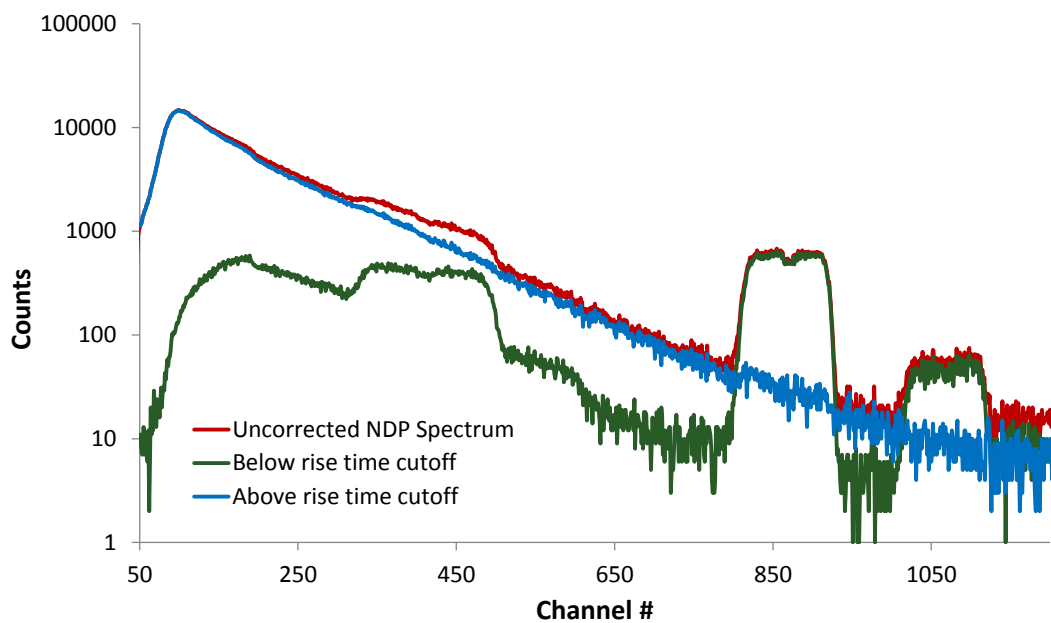


Figure 44: Pulse rise time discrimination of boron implanted silicon energy spectrum with detector FD 50-14-300 RG

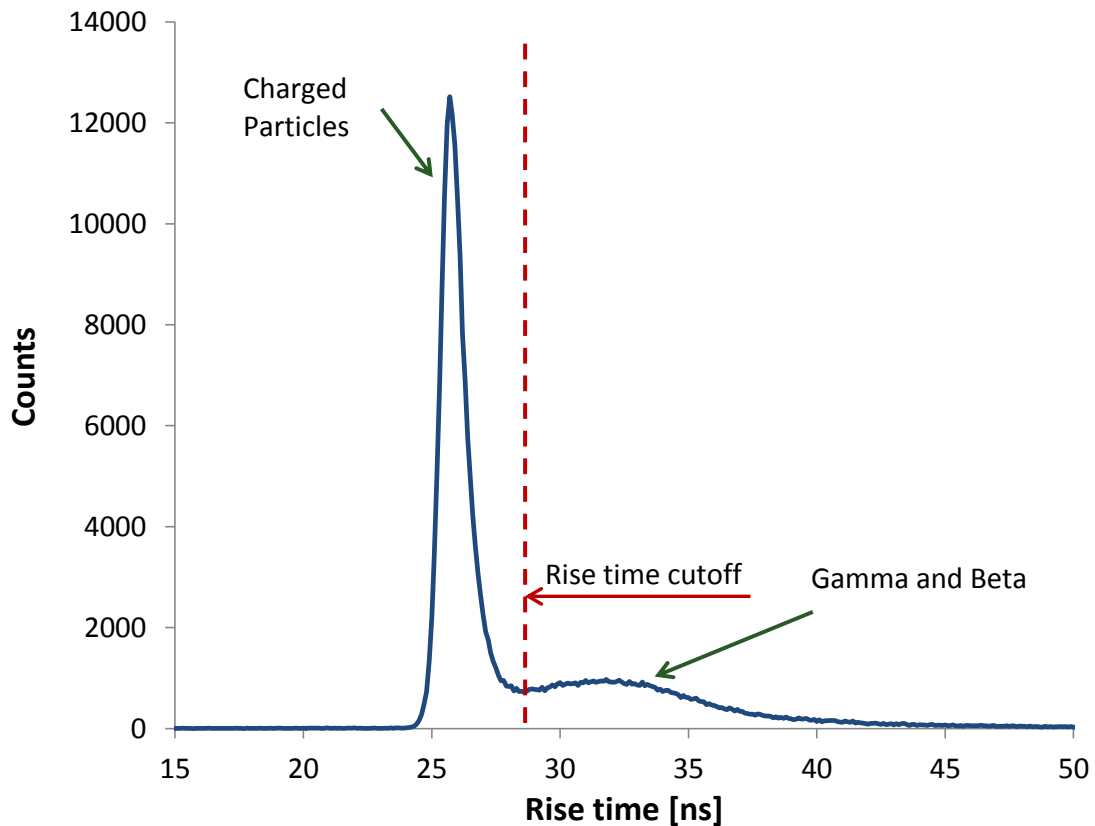


Figure 45: Rise time measurements of LiF film with detector FD 50-14-300 RG

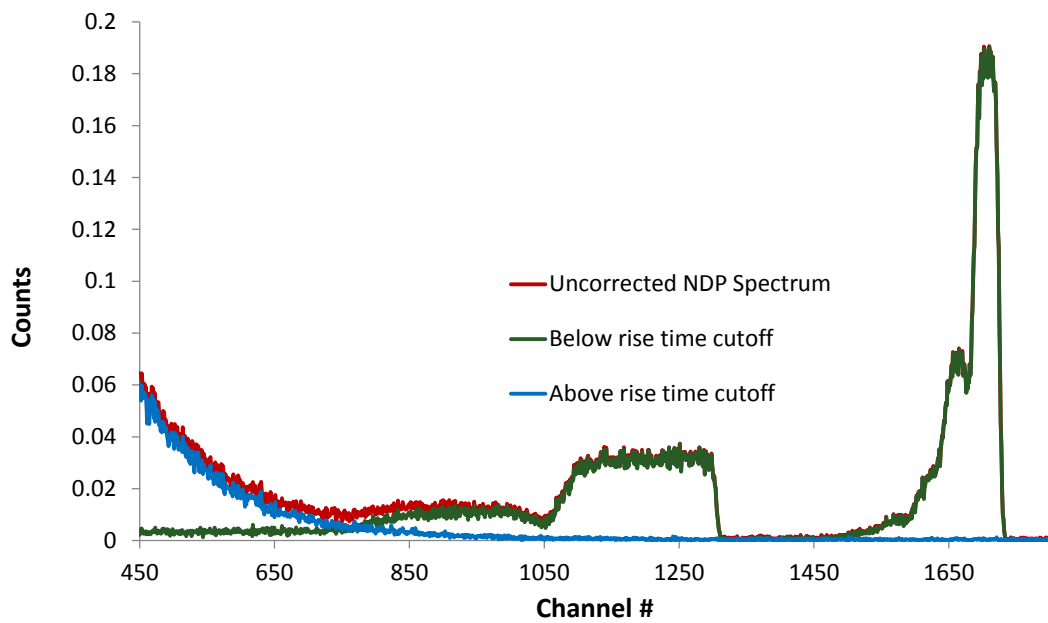


Figure 46: Rise time discrimination of LiF film energy spectrum with detector FD 50-14-300 RG

When determining the rise-time cut off, it was assumed that the charged particle rise-time peak was symmetric. For the boron implanted silicon it was not obvious that this was the case because it is merged with the gamma/beta peak. However, for the LiF film because the signal-to-background ratio was much greater it was obvious that this was a good assumption.

The resulting rise-time discriminated energy spectra for both samples resulted in a significant reduction in the low-energy background. Because the PIP detector was thicker than the surface barrier detectors used previously the background in the original spectra was significantly greater than was observed with the surface-barrier detectors. As, a result the spectra with rise time discrimination were comparable in their signal to noise ratio to the surface-barrier detectors.

These measurements demonstrate that a significant amount of the low energy background can be reduced in a NDP measurement with fully depleted PIP detectors. In the past these detectors would not have been used for low energy NDP measurements because they are much more sensitive to beta and gamma resulting in a much higher low-energy background than surface-barrier detectors. However with rise time discrimination they are comparable to surface-barrier detectors. In addition the PiPS detectors have the following advantages compared to surface-barrier detectors [38]:

1. Entrance window more stable and rugged
2. Leakage currents are 8 to 100 times smaller
3. Dead layer window thickness is thinner

4. Detectors can withstand much higher temperatures up to 100 °C

These advantages make them more durable and result in improved energy resolution over standard surface-barrier detectors. Therefore with rise-time discrimination they are a better choice for most NDP measurements. The increased energy resolution is demonstrated in Figure 47. The better resolution of the OSTR spectra with the PIPS detector resulted in better resolved features, especially for the decreased boron concentration midway through the deposition depth.

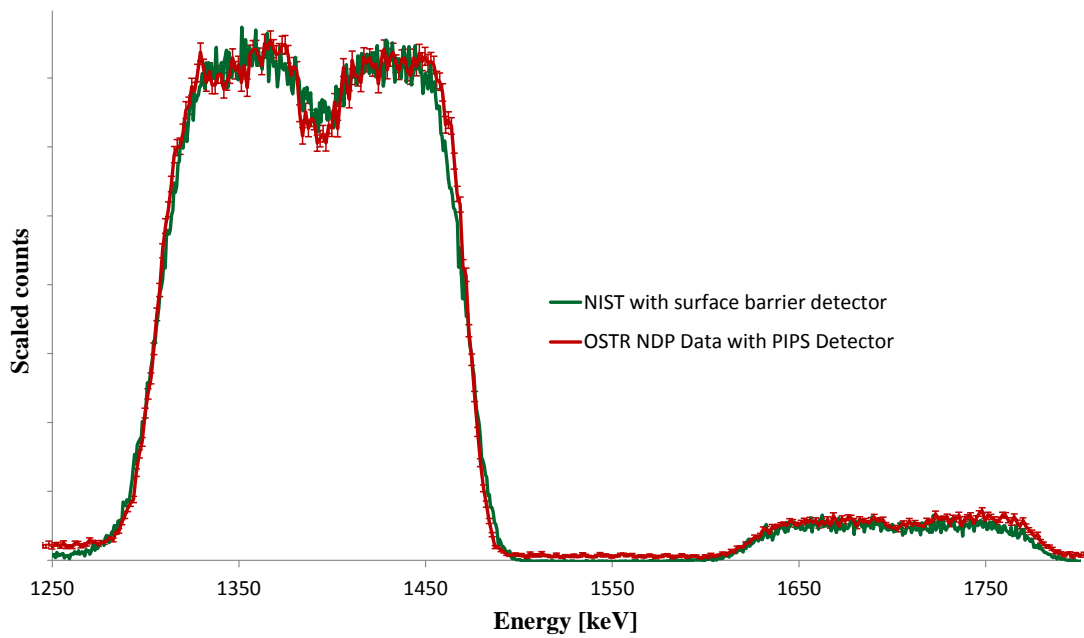


Figure 47: Comparison of OSTR NDP facility with PIPS detector to NIST NDP facility with surface barrier detector. Sample is a boron implanted silicon wafer.

6.4 Coincidence Measurements with LiF Film

Coincidence NDP measurements were performed with the facility on LiF film. The LiF film was obtained from and was certified to be 1- μm thick by Lebow Company [39]. This was thin enough so that both the alpha and triton particles emitted from neutron capture by ^6Li would be able to escape the sample. The LiF film as mounted in the sample chamber for the NDP coincidence measurements is shown in Figure 48.

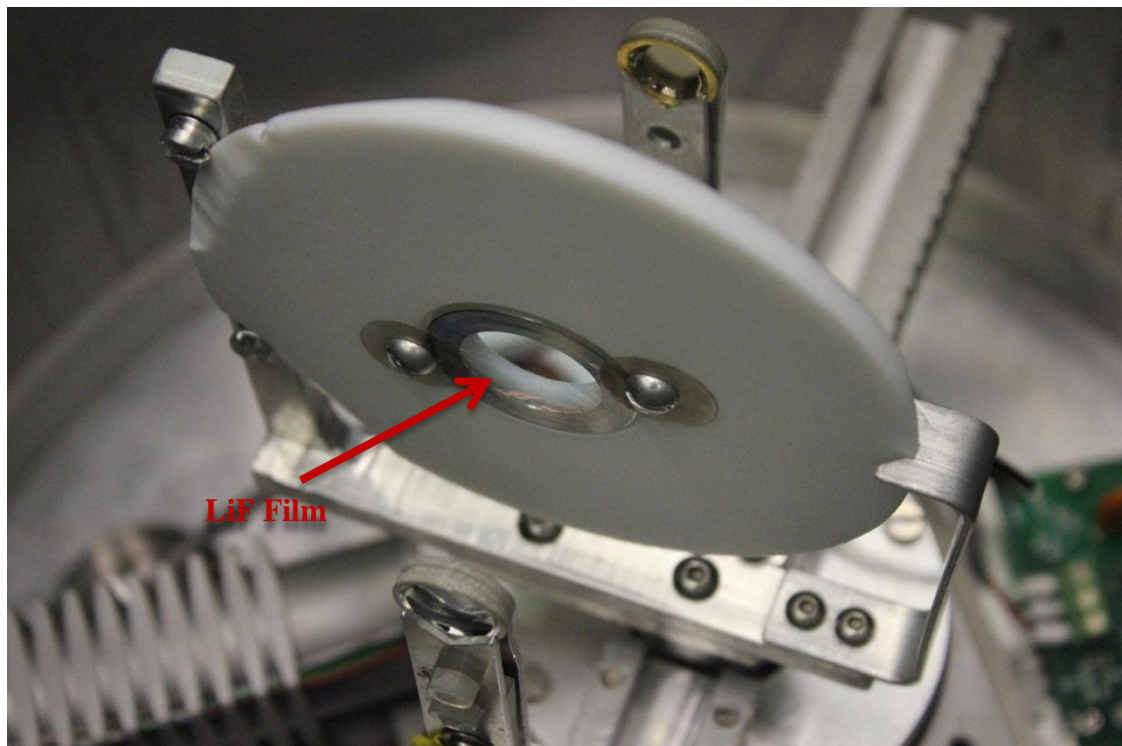


Figure 48: LiF film mounted in Teflon sample holder. Detectors are setup for coincidence NDP measurements.

Because the alpha particle and the triton are emitted at 180° to each other, a surface-barrier detector was placed on each side of the LiF film. Each detector was configured with its own preamplifier with the output from the preamplifiers connected to each of the 2 inputs on the digitizer. The data from this measurement are shown in

Figure 49. Count rates in detectors 1 and 2 differ because the trigger is set to channel 1. Therefore all counts observed in channel 1 are captured and only those events with a coincidence pulse in channel 2 are observed in the spectrum of channel 2.

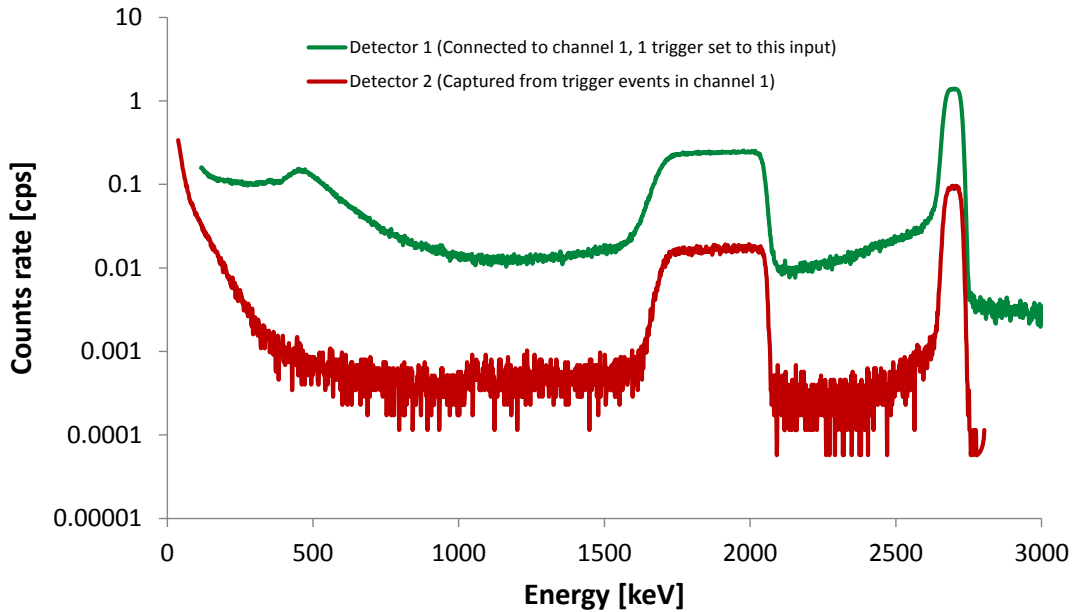


Figure 49: Raw spectrum from channel 1 and channel 2 with detectors on opposite sides of LiF film with the trigger set to channel 1.

Because the triton and alpha particle are both emitted at 180° to each other, true coincidence counts of the alpha peak in channel 1 should result only in counts in the triton peak for channel 2. This was demonstrated by setting an energy discrimination window in Matlab to accept only counts in channel 2, if the measured peak in channel 1 lies within one or the other of the two peaks. In addition since the digitizer was set to capture 2,048 samples for each pulse, there will be some events between the channels that are due to pile-up instead of coincidence. This was handled by using a trigger filter to test each pulse and make sure the time between the pulses in each channel was less than 500 ns. The results from this analysis are presented in Figure 50 and 41.

These figures show that the count rate is reduced a little in the separated pulses for each channel, because the trigger filter removed events recorded in channel 2 that were not true coincidence events. It also can be noted that the background is significantly reduced, resulting in approximately an order of magnitude reduction in the background level.

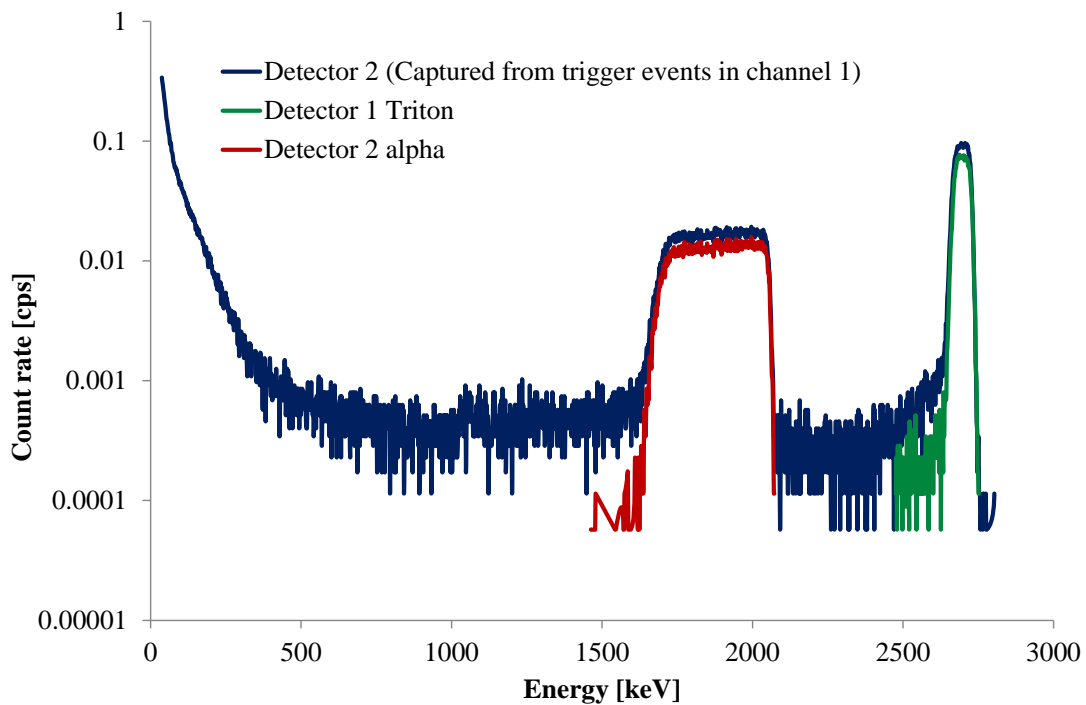


Figure 50: Coincidence measurements of LiF film. Energy level discriminator on channel 1 was set to accept only the pulse from detector channel 2 if the energy was within the triton peak.

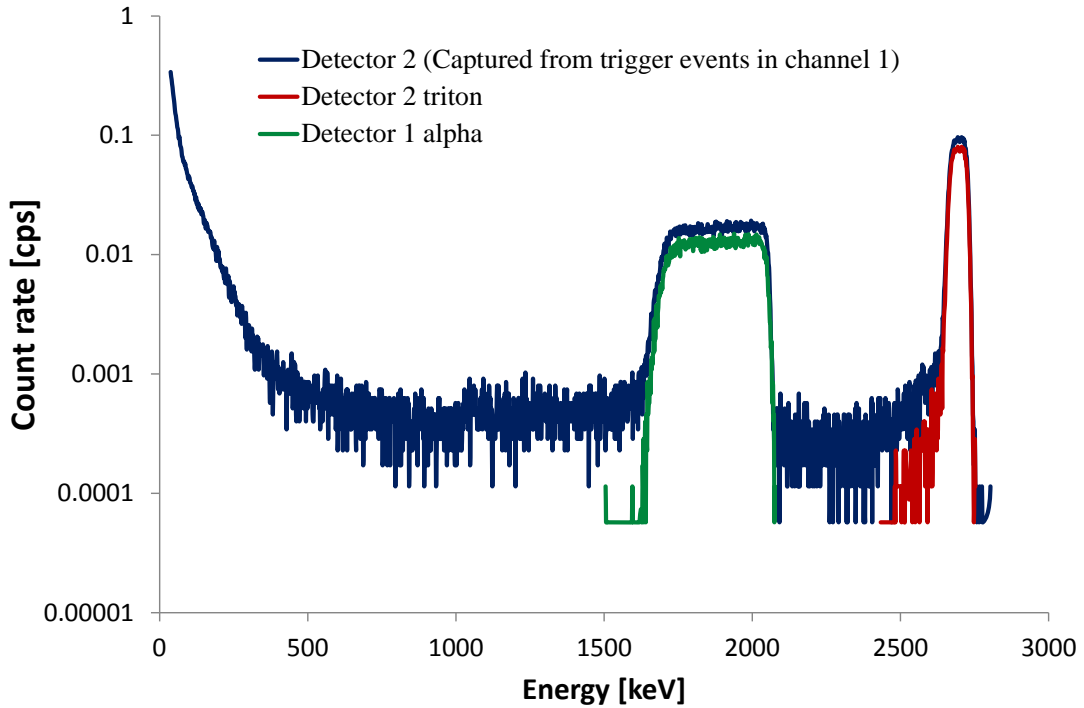


Figure 51: Coincidence measurements of LiF film. Energy level discriminator on channel 1 was set to accept only the pulse from detector channel 2 if the energy was within the alpha peak.

The LiF film was certified by the manufacturer to be $1\mu\text{m}$ thick. This was verified to be correct from the NDP measurement along with range data from alpha particles in LiF. The ranged data as well as the calculated depth distribution are presented in Figure 52 and 53.

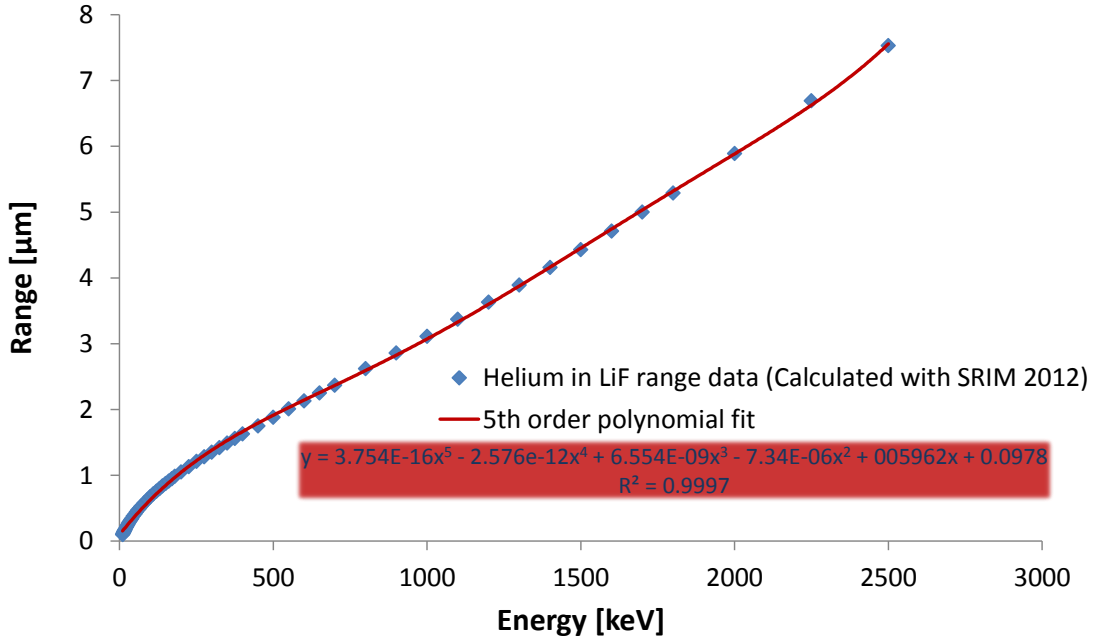


Figure 52: Helium in LiF stopping power data (Calculated with SRIM 2012)

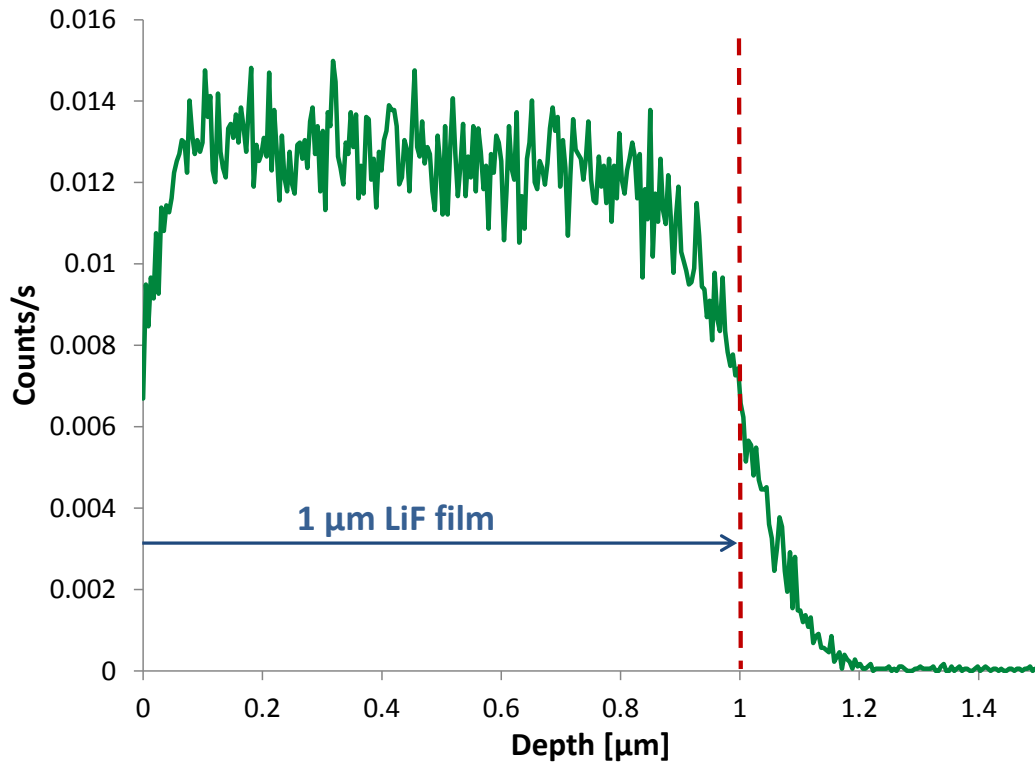


Figure 53: NDP measurement of LiF film thickness

6.5 NDP Analysis With Wavelet Smoothing

The wavelet smoothing method used for rise time analysis presented in section 5.5.3 also has applications for NDP spectrum analysis. Because wavelets can preserve many of the features in signals with sharp spikes and discontinuities, it can preserve many of the important features of the spectra while removing random fluctuations from poor statistics. Wavelet de-noising is often used in NMR spectroscopy, especially in cases where low signal-to-noise ratios are a problem [40].

For NDP facilities installed on low power research reactors the flux may be too low to obtain satisfactory statistics in a reasonable time. For these cases wavelet smoothing can be used to help separate the correct depth profile from the random noise in the spectra. This is demonstrated in Figure 54.

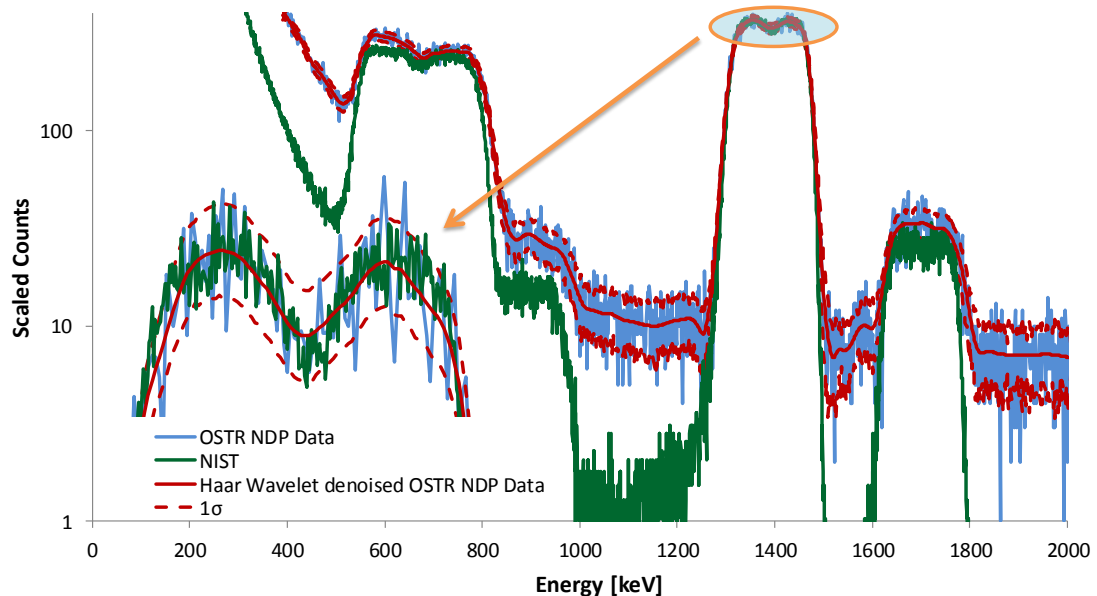


Figure 54: Wavelet de-noising applied to NDP spectroscopy. The wavelet de-noised data collected with the OSTR NDP facility is compared to a spectrum of the same sample analyzed with the NIST NDP facility.

The data from the OSTR facility had much poorer statistics because it was counted for about 1/10th of the time of the NIST data and the neutron beam in the OSTR NDP facility is considerably lower in intensity. Even with these poor statistics the wavelet de-noised data matched the NIST data fairly well. Therefore, for NDP facilities with lower sensitivities and limited reactor time this method can be used to provide a better representation of the true composition profile within the sample for data with poor statistics.

7. Additional Facility Modifications

PGNAA Fast Shutter System

An additional modification which has been added to the PGNAA/NDP facility during this work is a fast shutter system. The fast shutter system was designed to accommodate a series of experiments for Pacific Northwest National Laboratory (PNNL) for which they were modeling the decay gammas from short lived fission products in uranium and plutonium foils. Some examples of these were $^{139}_{52}\text{Te}$, $^{106}_{43}\text{Tc}$, $^{97}_{39}\text{Y}$, and $^{90}_{37}\text{Rb}$. The OSTR PGNAA facility along with the custom built fast shutter system was used to benchmark some of their models [41]. Because the half-life for the fission products of interest ranged from a couple seconds to about 30 seconds, in order to obtain sufficient statistics it was necessary to take repeated measurements and tally the results. These measurements required an automated shutter system which was able to open and close in less than 100 ms in order to obtain the required timing.

The shutter system consisted of 1.9 cm of borated aluminum mounted on a dual air cylinder. The shutter was installed on the facility between the sample station and the bioshield. In order to accommodate the shutter it was necessary to remove and replace the beam tube attached to the sample chamber entering the bioshield with an aluminum-thin-window. Solid works drawings illustrating the changes to the beam flight tube are presented in Figure 55 and 56.

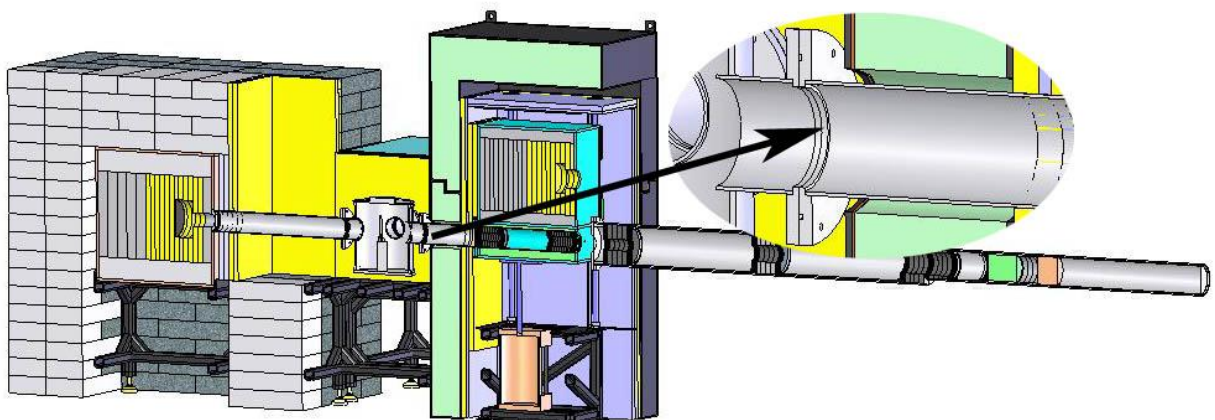


Figure 55: PGNAA Facility with sample chamber shutter beam tube.

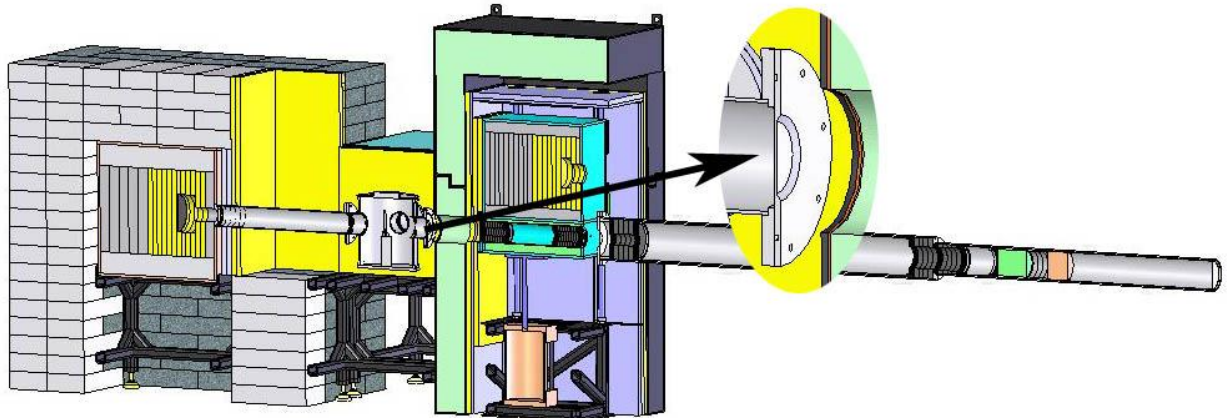


Figure 56: PGNAA Facility with sample chamber shutter beam tube replaced with aluminum-thin-window to accommodate the Fast Shutter for PNNL experiments.

After installation measurements were taken to determine the precise open and close time of the shutter using 70 psi air to drive the shutter. The resulting shutter transit times to open and close were 98.16 ± 0.09 ms and 86.82 ± 0.22 ms respectively as shown in Figure 57.

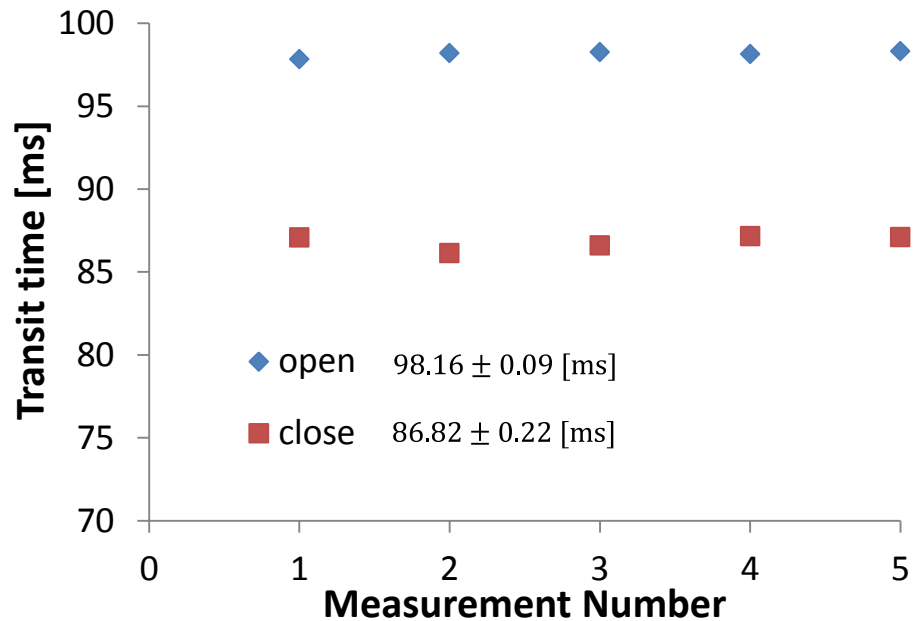


Figure 57: PGNAA/NDP Fast shutter system shutter open and close transit time

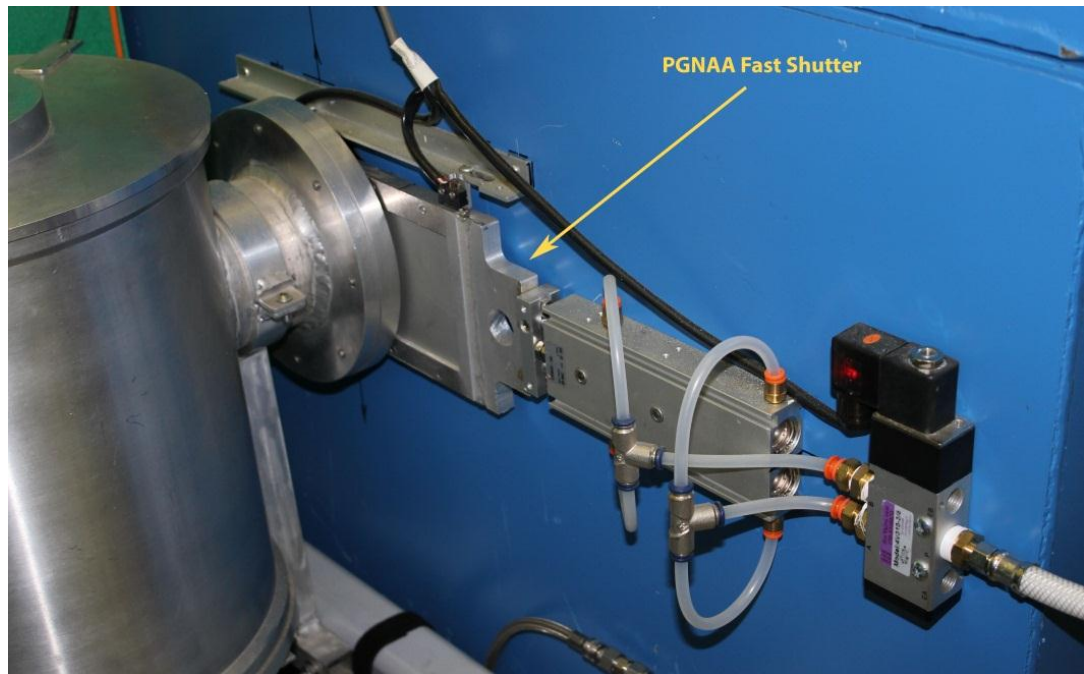


Figure 58: PGNAA Fast Shutter (Designed for PNNL experiments)

8. Conclusions and Future Work

Neutron depth profiling capabilities have been added to the Oregon State University PGNAA facility along with an advanced digital spectroscopy system and coincidence measurement capabilities. This added capability will permit many types of materials analysis that have not previously been available.

The combined NDP/PGNAA capability is unique and has not been previously implemented at a reactor facility in that both analysis techniques can be performed on a sample simultaneously. This is advantageous in that information which may be necessary for the NDP measurement, such as bulk elemental compositions, can be obtained from the PGNAA measurement. Also both techniques can be easily used to cross calibrate each other. The cross-calibration technique is most useful for the NDP analysis. This is because a proper NDP standard needs to be a sample with a known depth concentration of the isotope of interest, and it has to be deposited in the near surface layer of the sample. The problem with this is that such a sample may not be readily available for some isotopes.

Alternatively, the total concentration of the isotope of interest can be determined from PGNAA spectroscopy and the depth profile can be determined from NDP spectroscopy. The data from the two analysis techniques can then be combined to obtain the concentration as a function of depth. This works providing the isotope of interest is near enough to the surface of the sample or the sample is thin enough so that the isotope is within the range of the NDP measurement.

The digital spectroscopy system, which has been designed and built into the facility, is more versatile and is capable of a more in-depth analysis of the data on a pulse-by-pulse basis than standard radiation spectroscopy systems. In addition it is capable of coincidence measurements, as well as pulse-shape analysis. Both of these are not usually available with standard spectroscopy systems.

This digital system has been benchmarked with an ORTEC® DSPEC Pro spectrometer, a standard radiation spectroscopy system. These measurements demonstrated that the digital system is equivalent to the ORTEC® DSPEC Pro in resolution and that the dead-time correction used in the digital system is accurate.

The coincidence capabilities were demonstrated with a LiF film by measuring both the alpha particle and the triton emitted at opposite directions to each other from the neutron capture reaction in lithium. These measurements verified that in coincidence mode a majority of the unwanted background can be removed from the spectrum. This capability is especially useful when the detectors need to be moved closer to the sample to increase the geometric efficiency of the detector. For this case both the unwanted background is increased and the resolution of the spectra is decreased from charged-particles striking the detectors which are not emitted normal to the sample surface. In coincidence mode very little of the unwanted background is detected, as well as some particles emitted at a great enough angles to the surface normal that both emitted particles do not reach the detectors. In addition, if both particles are measured it is possible to determine the total distance travelled by the particles and correct for the decreased energy

resolution. This capability will likely be very useful for the analysis of lithium, especially for lithium ion battery research under way at NIST.

The rise-time discrimination capabilities were demonstrated with several different detectors. For standard surface-barrier detectors normally used in NDP measurements there was no significant benefit observed. However with PIPS detectors, which are more sensitive to gamma and beta radiation, a significant amount of the unwanted background could be removed by rise-time difference measurements. With this method the PIPS detector resulted in comparable background levels to the surface barrier detectors. However, since PIPS detectors have several advantages, including slightly better energy resolution, with the rise time measurement they are a better choice for many NDP applications.

The digital system also has time-stamping capabilities for which the precise timing of individual detection events can be recorded. These capabilities were designed with future real-time measurements of lithium ion battery research in mind. However, they would be valuable for measuring decay rates of isotopes and for other time sensitive experiments.

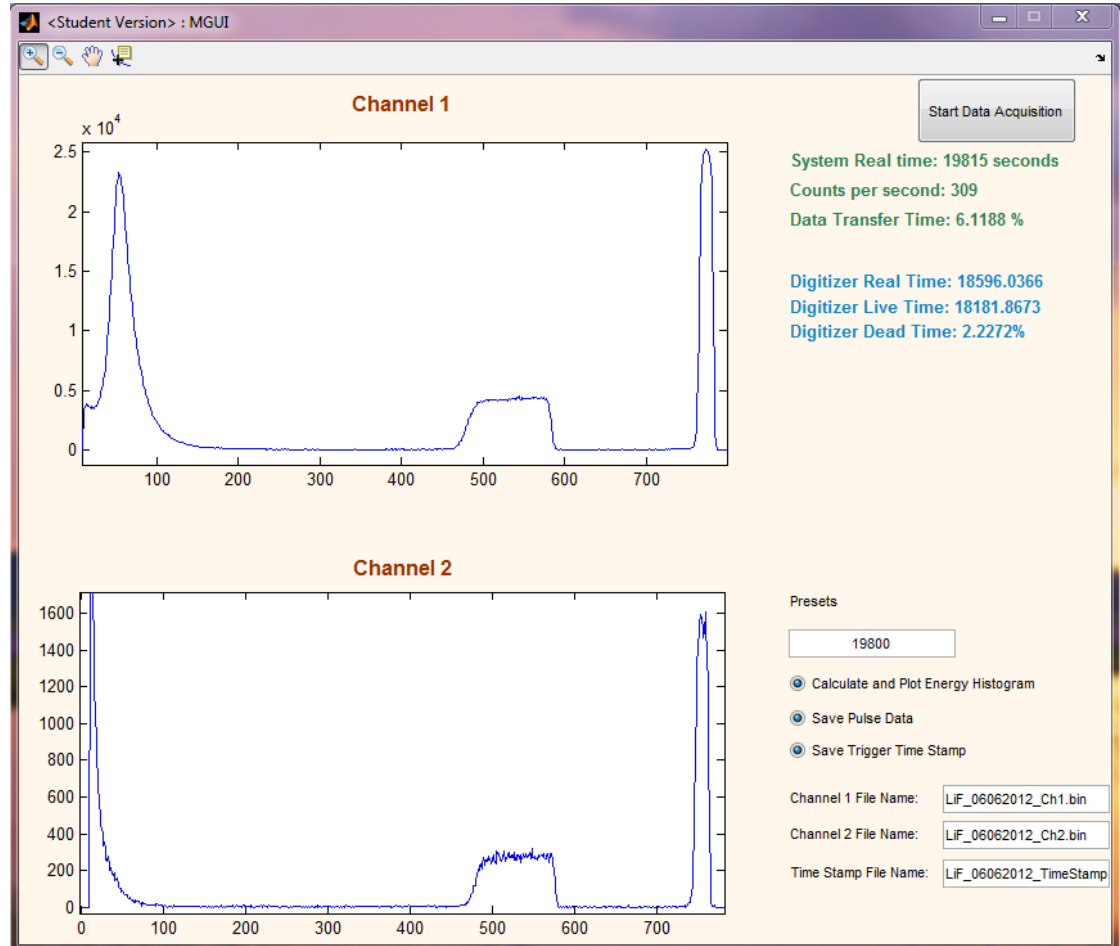
With the improvements in this system over past NDP and PGNAA facilities, especially with the digital spectroscopy system, this facility is far more versatile than most NDP facilities. In addition these combined capabilities make the facility applicable for a wide range of neutron-beam experiments, which will likely result in many improvements and additions to the facility over the years.

Since the digital spectroscopy data analysis is almost entirely based on software programming it is easily adaptable to a wide range of experimental needs. One disadvantage of the digitizer implemented in this facility design, is the lack of an on board FPGA. As a result, all the calculation intensive analyses of the data must be handled by the computer.

For this work the hardware trigger mode was used to capture only the data of interest, greatly reducing the amount of data which had to be processed by the computer. The disadvantage of this mode is that low-energy pulses will be missed and dead-time effects will be greater for high count rate applications. Also, signal base-level shifts will affect the trigger sensitivity. All of these disadvantages associated with hardware triggering can be eliminated by using software triggering with a trapezoidal trigger. For this the data must be processed through a trapezoidal filter implemented by an onboard FPGA or streamed to the computer and processed by the computer CPU. Since the digitizer used in this facility does not have an onboard FPGA, and since Matlab which was used for programming the digitizer was not capable of handling a high enough data throughput, this method was not used. However, with extensive programming involving multithreaded calculations with C++ programming and a reasonably fast multicore processor computer it is possible to perform the necessary calculations to implement software triggering with computer processor. Since this digital system would be beneficial to experiments being conducted at NIST, future work with this facility will involve implementing software triggering and increasing the software programmable capabilities of the spectroscopy system.

9. Appendix

9.1 Data Acquisition Code for GaGe Digitizer



```

function varargout = MGUI(varargin)
% Joshua Robinson 5/13/2012
% MGUI MATLAB code for MGUI.fig
%     MGUI, by itself, creates a new MGUI or raises the existing
%     singleton*.
%
% H = MGUI returns the handle to a new MGUI or the handle to
% the existing singleton*.
%
% MGUI('CALLBACK',hObject,eventData,handles,...) calls the
% local function named CALLBACK in MGUI.M with the given input
% arguments. MGUI('Property','Value',...) creates a new MGUI
% or raises the existing singleton*. Starting from the left,
% property value pairs are applied to the GUI before
% MGUI_OpeningFcn gets called. An unrecognized property name

```

```

%      or invalid value makes property application stop. All
%      inputs are passed to MGUI_OpeningFcn via varargin.
%      *See GUI Options on GUIDE's Tools menu. Choose "GUI allows
%      only one instance to run (singleton)".
%
% See also: GUIDE, GUIDATA, GUIHANDLES

% Edit the above text to modify the response to help MGUI

% Last Modified by GUIDE v2.5 13-May-2012 17:17:48

% Begin initialization code - DO NOT EDIT
gui_Singleton = 1;
gui_State = struct('gui_Name',         mfilename, ...
                   'gui_Singleton',   gui_Singleton, ...
                   'gui_OpeningFcn',  @MGUI_OpeningFcn, ...
                   'gui_OutputFcn',   @MGUI_OutputFcn, ...
                   'gui_LayoutFcn',   [] , ...
                   'gui_Callback',    []);
if nargin && ischar(varargin(1))
    gui_State.gui_Callback = str2func(varargin(1));
end

if nargout
    [varargout(1:nargout)] = gui_mainfcn(gui_State, varargin{:});
else
    gui_mainfcn(gui_State, varargin{:});
end
% End initialization code - DO NOT EDIT

% --- Executes just before MGUI is made visible.
function MGUI_OpeningFcn(hObject, eventdata, handles, varargin)
% Choose default command line output for MGUI
handles.output = hObject;

% Update handles structure
guidata(hObject, handles);

% --- Outputs from this function are returned to the command line.
function varargout = MGUI_OutputFcn(hObject, eventdata, handles)
varargout(1) = handles.output;

% --- Executes on button press in pushbutton1.
function pushbutton1_Callback(hObject, eventdata, handles)

% Digitizer acquisition Code+++++=====
%clear;

% User input
data=====
```

```

%JAR input data
capture_time = str2double(get(handles.edit1,'String')); % Acuisition
% time
plotamp = get(handles radiobutton1,'Value');
saveData = get(handles radiobutton2,'Value'); % saveData=true-->save
% data to .bin file,
% otherwise false
saveTStamp = get(handles radiobutton3,'Value');
%plotamp=true; % Calculate and plot pulse hight histogram
=====
====

%Add Path to Matlab
directory!!!!!!!!!!!!!!!!!!!!!!!!!!!!!!!!!!!!!!!
csml=getenv('CsMlDir');
pp=strcat(csml,pathsep);
pp=strcat(pp,csml);
pp=strcat(pp,'Main');
pp=strcat(pp,pathsep);
pp=strcat(pp,csml);
pp=strcat(pp,'CsMl');
pp=strcat(pp,pathsep);
pp=strcat(pp,csml);
pp=strcat(pp,'Adv');
pp=strcat(pp,pathsep);
path(pp, path);
clear csml;
clear pp;
%!!!!!!!!!!!!!!!!!!!!!!!!!!!!!!!!!!!!!!!!!!!!!!!
!!!
% Initialize Digitizer Board and variables for multiple records and
data
% time stamp
@oooooooooooooooooooooooooooooooooooooooooooo

systems = CsMl _Initialize;
CsMl_ErrorHandler(systems);
[ret, handle] = CsMl _GetSystem;

CsMl_ErrorHandler(ret);

[ret, sysinfo] = CsMl _GetSystemInfo(handle);

s = sprintf('-----Board name: %s\n', sysinfo.BoardName);
disp(s);

%-----SetupMultipleRecord
%(handle);

```

```
% Set the acquisition, channel and trigger parameters for the system
and
% calls ConfigureAcquisition, ConfigureChannel and ConfigureTrigger.

[ret, sysinfo] = CsM1_GetSystemInfo(handle);
CsM1_ErrorHandler(ret, 1, handle);

acqInfo.SampleRate = 200000000;
acqInfo.ExtClock = 0;
acqInfo.Mode = CsM1_Translate('Single', 'Mode');
acqInfo.SegmentCount = 4000;
acqInfo.Depth = 1024;
acqInfo.SegmentSize = 2048;
acqInfo.TriggerTimeout = 10000000000000000000;
%acqInfo.TriggerTimeout = 10000;
acqInfo.TriggerHoldoff = 1024;
acqInfo.TriggerDelay = 0;
acqInfo.TimeStampConfig = 0;

[ret] = CsM1_ConfigureAcquisition(handle, acqInfo);
CsM1_ErrorHandler(ret, 1, handle);

% Set up all the channels even though
% they might not all be used. For example
% in a 2 board master / slave system, in single channel
% mode only channels 1 and 3 are used.
for i = 1:sysinfo.ChannelCount
    chan(i).Channel = i;
    chan(i).Coupling = CsM1_Translate('DC', 'Coupling');
    chan(i).DiffInput = 0;
    chan(i).InputRange = 200;
%chan(i).Impedance = 1000000;
    chan(i).Impedance = 50;
    chan(i).DcOffset = 0;
    chan(i).DirectAdc = 0;
    chan(i).Filter = 0;
end;

[ret] = CsM1_ConfigureChannel(handle, chan);
CsM1_ErrorHandler(ret, 1, handle);

trig(1).Trigger = 1;
trig(1).Slope = CsM1_Translate('Positive', 'Slope');
trig(1).Level = -65; %Addjust to apropritate trigger level
trig(1).Source = 1;
trig(1).ExtCoupling = CsM1_Translate('DC', 'ExtCoupling');
trig(1).ExtRange = 200;

trig(2).Trigger = 2;
trig(2).Slope = CsM1_Translate('Negative', 'Slope');
trig(2).Level = -65; %Set to the samme trigger level as trig(1)
trig(2).Source = 1;
trig(2).ExtCoupling = CsM1_Translate('DC', 'ExtCoupling');
trig(2).ExtRange = 200;
```



```
% Save time stamp to .bin file
if saveTStamp
    filenameTstp = get(handles.edit4, 'String');
    fidT = fopen(filenameTstp, 'w');
    if fidT == -1
        fprintf('Error: Unable to create dataT file\n');
    end
end

% Buffer variables#####
BuffChA=zeros(acqInfo.SegmentCount,acqInfo.SegmentsSize);
BuffChB=zeros(acqInfo.SegmentCount,acqInfo.SegmentsSize);
%#####

% Variables for calculating and displaying amplitude
histogram^^^^^^^^^
if plotamp
    aray_A_length=2000;
    E_Hist_A=zeros(1,aray_A_length);
    aray_B_length=2000;
    E_Hist_B=zeros(1,aray_B_length);
    L_E_reject=10; %Reject low energy counts
    %filter
    pos_ones=200;
    neg_ones=200;
    Zeros=200;
    pulseData=zeros(1,1024+1024);
    % double(pulseData);

    % Amplitude filter coefficients
    for i_pos_ones = 1:pos_ones
        h(i_pos_ones)=1/pos_ones;
    end
    for i_zeros = 1:Zeros
        h(i_pos_ones+pos_ones)=0;
    end
    for i_neg_ones = 1:neg_ones
        h(i_neg_ones+pos_ones+Zeros)=-1/neg_ones;
    end
    double(h);
end
%^^^^^^^^^^^^^^^^^^^^^^^^^^^^^^^^^^^^^^^^^^^^^^^^^^^^^^^^^^^^^^^^^

%Datal capture loop*****
while toc(startTickCount)<capture_time;
    if Calculated == 0
        % Obtain handle and status of digitizer board
        [ret, acqInfo] = CsM1_QueryAcquisition(handle);
        ret = CsM1_Capture(handle);
        CsM1_ErrorHandler(ret, 1, handle);
        status = CsM1_QueryStatus(handle);
    end
    dtwrng=0;
    while status ~= 0 % Wait till memory buffer is
filled#####
```

```

dtwrng=dtwrng+1;
pause(.0000000001); % pause is used to reduce Matlab overhead
% but should only be used when SegmentCount
% is large.
status = CsM1_QueryStatus(handle);
end
%%%%%%%%%%%%%%%%%%%%%%%%%%%%%%%%%%%%%
StartTransferTime = toc(startTickCount); % start time for data
if dtwrng < 2

    set(handles.text12, 'string', 'Count rate is too high for
processor speed');
end
% transfer
% Get timestamp information
transfer.Channel = 1;
transfer.Mode = CsM1_Translate('TimeStamp', 'TxMode');
transfer.Length = acqInfo.SegmentCount;
transfer.Segment = 1;
[ret, tsdata, tickfr] = CsM1_Transfer(handle, transfer);

transfer.Mode = CsM1_Translate('Default', 'TxMode');
transfer.Start = -acqInfo.TriggerHoldoff;
transfer.Length = acqInfo.SegmentSize;

MaskedMode = bitand(acqInfo.Mode, 15);
ChannelsPerBoard = sysinfo.ChannelCount / sysinfo.BoardCount;
ChannelSkip = ChannelsPerBoard / MaskedMode;
xaxis = MaskedMode; %JAR
yaxis = sysinfo.BoardCount; %JAR

for channel = 1:ChannelSkip:sysinfo.ChannelCount
    transfer.Channel = channel;
    for i = 1:acqInfo.SegmentCount
        transfer.Segment = i;
        [ret, data, actual] = CsM1_Transfer(handle, transfer);
        CsM1_ErrorHandler(ret, 1, handle);
%?????????????????????????????????????????????????????????????
%           Uncomment to plot each record, this is used for %
%           testing only!
%           plot(handles.axes1, data);
%           pause(1);
%?????????????????????????????????????????????????????????????

% Adjust the size so only the actual length of data is
%saved to the file
length = size(data, 2);
if length > actual.ActualLength
    data(actual.ActualLength:end) = [];
    length = size(data, 2);
end;

```

```

Calculated = Calculated+1; % Number of records processed

if channel==1
    BuffChA(i,:)=data;
end

if channel==2
    BuffChB(i,:)=data;
end

end
end % End of transfer Loop

% --- Executes on button press in pushbutton3.

%Update text output
%Datal transfer complete start digitizer Acquisition->->->->->-
%Obtain handle and status of digitizer board
[ret, acqInfo] = CsM1_QueryAcquisition(handle);
ret = CsM1_Capture(handle);
CsM1_ErrorHandler(ret, 1, handle);
status = CsM1_QueryStatus(handle);
%->->->->->->->->->->->->->->->->->->->->->->-
StopTransferTime = toc(startTickCount);

TotalTransferTime=(StopTransferTime - StartTransferTime) ...
+ TotalTransferTime;

#####
% Update waitbar progress
waitbar(toc(startTickCount) / capture_time, ...
    waitbarHandle, ...

```



```

if saveData==1
    fclose(fid2);
end

if saveTStamp==1
    fclose(fidT);
end

delete(waitbarHandle);
ret = CsM1_FreeSystem(handle);

% Save the transfer time

fprintf('Dead Time due to data Transfer %u ', TransferDeadTime);
fprintf('Captured %u Records in %g sec (%g Records per sec)\n',...
    Calculated, RealTime, RecordsPerSec);
fprintf('Transfer time %u ', TotalTransferTime);

TotalSystemRealTime
TotalDecayDeadTime

filetxt = fopen('BSW_06292012(2).txt','wt');
fprintf(filetxt,'Dead Time due to data Transfern %u \n' , ...
    TransferDeadTime);
fprintf(filetxt,...
    'Captured %u Records in %g sec (%g Records per sec)...%n',...
    Calculated, RealTime, RecordsPerSec);
fprintf(filetxt,'Transfer time %u \n' , TotalTransferTime);
fprintf(filetxt,'Digitizer Dead time %u \n' , TotalDecayDeadTime);
fprintf(filetxt,'Digitizer Real Time %u \n' , TotalSystemRealTime);
fclose(filetxt);

function edit1_Callback(hObject, eventdata, handles)

% --- Executes during object creation, after setting all properties.
function edit1_CreateFcn(hObject, eventdata, handles)

if ispc && isequal(get(hObject,'BackgroundColor'), get...
    (0,'defaultUicontrolBackgroundColor'))
    set(hObject,'BackgroundColor','white');
end

% --- Executes on button press in radiobutton1.
function radiobutton1_Callback(hObject, eventdata, handles)

```

```
% --- Executes on button press in radiobutton2.
function radiobutton2_Callback(hObject, eventdata, handles)

function radiobutton3_Callback(hObject, eventdata, handles)

function edit2_Callback(hObject, eventdata, handles)

function edit2_CreateFcn(hObject, eventdata, handles)

if ispc && isequal(get(hObject,'BackgroundColor'), get(0, ...
    'defaultUicontrolBackgroundColor'))
    set(hObject,'BackgroundColor','white');
end

function edit3_Callback(hObject, eventdata, handles)

function edit3_CreateFcn(hObject, eventdata, handles)

if ispc && isequal(get(hObject,'BackgroundColor'), get(0, ...
    'defaultUicontrolBackgroundColor'))
    set(hObject,'BackgroundColor','white');
end

function edit4_Callback(hObject, eventdata, handles)

function edit4_CreateFcn(hObject, eventdata, handles)

if ispc && isequal(get(hObject,'BackgroundColor'), get(0, ...
    'defaultUicontrolBackgroundColor'))
    set(hObject,'BackgroundColor','white');
end
```

9.2 Dead-Time Measurement Function

```
% Joshua Robinson 6/8/2012
%This function is used to measure pulse-decay time and dead-time
%effects when operating in complex trigger mode. Trigger engine
%1 is set to trigger on a positive slope and trigger engine 2 set
%to trigger on a negative slope. Both trigger engines are set to
%the same trigger level. Trigger 1 triggers when a pulse occurs
%with amplitude greater than the trigger threshold and trigger 2
%triggers when the pulse decays below the trigger threshold. The
%time difference between the two events is used to calculate the
%dead time for each measured pulse.

function [SystemRealTime, DecayDeadTime]=DeadTimeCorrection(...
    SegmentCount,BuffChA,tsdata)

DecayDeadTime=0;
SystemRealTime=tsdata(SegmentCount)*0.000001;

for k=1:SegmentCount-1

    if (mean(BuffChA(k,1:1024)))-(mean(BuffChA(k, (1025:2048)))) ...
        < 0 && (mean(BuffChA(k+1,1:1024)))-(mean(BuffChA(k+1, ...
        1025:2048))) > 0

        tDecay=(tsdata(k+1)-tsdata(k))*0.000001;
        DecayDeadTime=DecayDeadTime+tDecay;
    else
        DecayDeadTime=(2048/200000000)+(0.000002)+DecayDeadTime;
    end
end
```

9.2 Rise-Time Measurement Function

```
%Joshua Arthur Robinson 2/18/2012
%This function calculates and outputs rise time in ns

function[r_time]=risetime(z,z_length,sample_rate)
%Rise time function -----
%Rise time
z_max=max(z(500:1500));
z_min=min(z(500:1500));
%z_med=median(z);
%z_amp=z_max-z_min;
aprox=[0,0];
%At 90% and 10%
z_nty=((z_max-z_min)*0.60)+z_min;
z_ten=((z_max-z_min)*0.20)+z_min;
%Determine value near 90%-----

%Determine value near 90%-----
i_z_nty=1;
nty_srch=z(i_z_nty);
while nty_srch<z_nty && i_z_nty<z_length
    nty_srch=z(i_z_nty);
    i_z_nty=i_z_nty+1;
end
if nty_srch ==z_nty && i_z_nty~ =1
%Extrapolate to improve result if necessary
t_h=((z_nty)-z(i_z_nty-2))/(z(i_z_nty-1)-z(i_z_nty-2))+(i_z_nty-1)-1;
else
    t_h=i_z_nty-1;
end
%Determine value near 10%-----

i_z_ten=i_z_nty;
ten_srch=z(i_z_ten);
while ten_srch>z_ten && i_z_ten>1
    ten_srch=z(i_z_ten);
    i_z_ten=i_z_ten-1;
end
if ten_srch ==z_ten && i_z_ten+2<2048
%Extrapolate to improve result if necessary
%t_h=((z_nty-1)-z(i_z_nty-2))/(z(i_z_nty-1)-z(i_z_nty-2))+(i_z_nty-1)-1;
t_L=((z_ten)-z(i_z_ten+1))/(z(i_z_ten+2)-z(i_z_ten+1))+(i_z_ten+1);
else
    t_L=i_z_ten+1;
end
%D %
%DCalculate rise time
r_time=(t_h-t_L)*(1/sample_rate)*1e+9;
%
```


9.3 Peak Amplitude Measurement Function

```
%Joshua Arthur Robinson 2/17/2012
function[amp]=PeakAmplitude(pos_ones,Zeros,neg_ones,Record_length,z)
%Enter Record Info.
%Record_length=2048;
%Trapezoidal Filter coefficients
% pos_ones=200;
% neg_ones=200;
% Zeros=200;
%Sum of filter coefficients: used to subtract filter response at the
%beginning of filter array
filter_start=pos_ones+neg_ones+Zeros;
% Make Trapezoidal Filter
for i_pos_ones = 1:pos_ones
    h(i_pos_ones)=1/pos_ones;
end
for i_zeros = 1:Zeros
    h(i_pos_ones+pos_ones)=0;
end
for i_neg_ones = 1:neg_ones
    h(i_neg_ones+pos_ones+Zeros)=-1/neg_ones;
end
%Filter result
y=conv(double(h),double(z));
%PEAK AMPLITUDE-----
-----
%calculate Amplitude of Peak
amp=max(y(filter_start:Record_length));
end
```

9.4 Haar Wavelet De-noising Code Generated with Matlab Wavelet Package

```
%Joshua Arthur Robinson 5/25/2012
function [sigDEN,wDEC] = func_denoise_sw1d_BSW4302012(SIG)
% FUNC_DENOISE_SW1D Saved De-noising Process.
% SIG: vector of data
%
% sigDEN: vector of de-noised data
% wDEC: stationary wavelet decomposition

% Auto-generated by Wavelet Toolbox on 27-May-2012 10:53:00

% Analysis parameters.
%-----
wname = 'haar';
level = 7;

% Denoising parameters.
%-----
% meth = 'sqtwolog';
% scal_OR_alfa = mln;
sorh = 'h'; % Specified soft or hard thres holding
thrSettings = (...
    [
        ...
        1.0000000000000000 2048.0000000000000000 0.004503290854993;
    ...
    ];
    ...
    [
        ...
        1.0000000000000000 2048.0000000000000000 0.002763225885010;
    ...
    ];
    ...
    [
        ...
        1.0000000000000000 2048.0000000000000000 0.003812435536062;
    ...
    ];
    ...
    [
        ...
        1.0000000000000000 2048.0000000000000000 0.006039637985230;
    ...
    ];
    ...
    [
        ...
        1.0000000000000000 2048.0000000000000000 0.002419331659164;
    ...
    ];
    ...
    [
        ...
        1.0000000000000000 2048.0000000000000000 0.002377357045727;
    ...
    ];
    ...
    [
        ...
        1.0000000000000000 2048.0000000000000000 0.002108720691309;
    ...
    ];
    ...
    (
;

% Decompose using SWT.
```

```

%-----
wDEC = swt(SIG,level,wname);

% Denoise.
%-----
len = length(SIG);
for k = 1:level
    thr_par = thrSettings(k);
    if ~isempty(thr_par)
        NB_int = size(thr_par,1);
        x      = [thr_par(:,1) ; thr_par(NB_int,2)];
        x      = round(x);
        x(x<1) = 1;
        x(x>len) = len;
        thr = thr_par(:,3);
        for j = 1:NB_int
            if j==1 , d_beg = 0; else d_beg = 1; end
            j_beg = x(j)+d_beg;
            j_end = x(j+1);
            j_ind = (j_beg:j_end);
            wDEC(k,j_ind) = wthresh(wDEC(k,j_ind),sorh,thr(j));
        end
    end
end

% Reconstruct the de-noise signal using ISWT.
%-----
sigDEN = iswt(wDEC,wname);

```

9.5 Rise Time, Amplitude, Wavelet De-noising Code and Pulse Rise Time Discrimination Code

```

%Pulse height histograms-----
chn_amp=16000;                                % Number of channels
hist_amp=zeros(1,chn_amp);                      % Create array

hist_amp_low=zeros(1,chn_amp);      % Below rise time cutoff
hist_amp_high=zeros(1,chn_amp);     % Above rise time cutoff
%-----End Pulse height histogram

% Open Data File and find number of records-----
fid=fopen('BSW_04302012CH1.bin');    % Open file
fseek(fid, 0, 'eof');                % Go to end of file
position = ftell(fid);              % read pointer position
fseek(fid, 0, 'bof');                % Go to beginning of file
record_loop=position/(2*2*2*2048);   % number of records
%-----Process data-----

for k=1:record_loop
y=fread(fid, 2048, 'double');           % Read from file

%De-noising
z = func_denoise_swld_BSW4302012(y);

%%%%Save De-noised data
fwrite(fid2, z, 'double');

%Calculate rise time-----
z_max=max(z);
[r_time]=risetime(z,2048,180e+6);
int_r_time=round(r_time*10);

%
%calculate Amplitude-----
[amp]=PeakAmplitude(30,30,30,2048,z);

int_amp=round(amp*22500);

%Bin rise times
if int_r_time<chn_rise && int_r_time>0
    hist_risetime(int_r_time)=hist_risetime(int_r_time)+1;
end

%Bin Amplitude
if int_amp<chn_amp && int_amp>0
    hist_amp(int_amp)=hist_amp(int_amp)+1;
end

```

```

% Rise time discrimination histogram-----
if int_r_time< 400 && int_amp<chn_amp && int_amp>0
    hist_amp_low(int_amp)=hist_amp_low(int_amp)+1;
elseif int_amp<chn_amp && int_amp>0
    hist_amp_high(int_amp)=hist_amp_high(int_amp)+1;
end

%
% Update progress
Calculated = Calculated + 1;
if k >= record_loop
    captureDone = true;
    success = true;
elseif toc(updateTickCount) > updateInterval_sec
    updateTickCount = tic;

% Update waitbar progress
waitbar(double(Calculated) / double(record_loop), ...
    waitbarHandle, ...
    sprintf('Claculated %u peaks', Calculated));

% Check if waitbar cancel button was pressed
if getappdata(waitbarHandle,'canceling')
    break
end
end

% %Uncomment code bellow to show processed data
% % % %
%         end
%             if int_r_time>600
%                 clf;
%                 hold on;
%                 %plot(fit);
%                 plot(y);
%                 plot(z,'r');
%                 exmpl_y=y;
%                 exmpl_z=z;
%                 %plot(z(fmax_idx:2048));
%                 pause(1);
%                 elseif int_r_time<500
%                     hold on;
%                     plot(y,'y');
%                     plot(z,'g');
%                 end
%                 hold on;
%                 pause(1);
%                 plot(amp,r_time);
%                 hold on
end

delete(waitbarHandle);

```

```
fclose(fid);

% Close the data file
if fid2 ~= -1
    fclose(fid2);
end

figure(1)
plot (x_chn_rise,hist_risetime,'r');
%plot (x_chn_rise,hist_risetime,'r');
title('Histogram of Detector Rise Times');
xlabel('Rise time [nano seconds]');
ylabel('Counts');

figure(2)
hold on
plot(hist_amp);
title('Energy Spectrum');
xlabel('Channel #');
ylabel('Counts');

figure(3)
plot(hist_amp_low);
title('Energy Spectrum bellow cutoff');
xlabel('Channel #');
ylabel('Counts');

figure(4)
plot(hist_amp_high);
title('Energy Spectrum above cutoff');
xlabel('Channel #');
ylabel('Counts');

figure(2)
hold on
plot(hist_amp);
title('Energy Spectrum');
xlabel('Channel #');
ylabel('Counts');

plot(hist_amp_low,'r');
plot(hist_amp_high, 'c');
```

10. Bibliography

- [1] J.F. Ziegler, G.W. Cole, J.E. Baglin, Technique for determining concentration profiles of boron impurities in substrates, *Journal of Applied Physics*, 43 (1972) 7.
- [2] R.G. Downing, G.P. Lamaze, J.K. Langland, S.T. Hwang, Neutron Depth Profiling: Overview and Description of NIST Facilities, *Journal of Research of the National Institute of Standards and Technology*, 98 17.
- [3] G.P. Lamaze, H.H. Chen-Mayer, D.A. Becker, F. Vereda, R.B. Goldner, T. Haas, P. Zerigian, Cold neutron depth profiling of lithium-ion battery materials, *Journal of Power Sources*, 119–121 (2003) 680-685.
- [4] S. Whitney, S.R. Biegalski, Y.H. Huang, J.B. Goodenough, Neutron Depth Profiling Applications to Lithium-Ion Cell Research, *Journal of The Electrochemical Society*, 156 (2009) A886-A890.
- [5] S.C. Nagpure, R.G. Downing, B. Bhushan, S.S. Babu, L. Cao, Neutron depth profiling technique for studying aging in Li-ion batteries, *Electrochimica Acta*, 56 (2011) 4735-4743.
- [6] M. Mutterer, W.H. Trzaska, G.P. Tyurin, A.V. Evsenin, J. Von Kalben, J. Kemmer, M. Kapusta, V.G. Lyapin, S.V. Khlebnikov, Breakthrough in pulse-shape based particle identification with silicon detectors, *IEEE Transactions on Nuclear Science*, 47 (2000) 756-759.
- [7] J. Vacík, J. Červená, V. Hnatowicz, V. Havránek, J. Hoffmann, S. Pošta, D. Fink, R. Klett, Pulse-shape discrimination in neutron depth profiling technique, *Nuclear Instruments and Methods in Physics Research Section B: Beam Interactions with Materials and Atoms*, 142 (1998) 397-401.
- [8] N.R. Parikh, E.C. Frey, H.C. Hofsass, M.L. Swanson, G. Downing, T.Z. Hossain, W.-K. Chu, Neutron Depth Profiling by Coincidence Spectrometry, *Nuclear Instruments and Methods in Physics Research Section B*, 45 (1990) 5.
- [9] J.F.M. Oudenhoven, F. Labohm, M. Mulder, R.A.H. Niessen, F.M. Mulder, P.H.L. Notten, In Situ Neutron Depth Profiling: A Powerful Method to Probe Lithium Transport in Micro-Batteries, *Advanced Materials*, 23 (2011) 4103-4106.
- [10] HFBR Decommissioning, in: Brookhaven National Laboratory, 2010.
- [11] G. Downing, R. Fleming, Analytical Applications of Neutron Depth Profiling, *Journal of Radioanalytical and Nuclear Chemistry*, 112 (1986) 14.

- [12] G. Downing, G.P. Lamaze, Neutron Depth Profiling Technique and facilities, *Neutron News*, 4 (1993) 6.
- [13] D.J. Turkoglu, Design, Construction and Characterization of an External Neutron Beam Facility at The Ohio State University Nuclear Reactor Laboratory, in: *Nuclear Engineering*, The Ohio State University, 2012, pp. 132.
- [14] R.G. Downing, J.T. Maki, R.F. Fleming, Application of Neutron Depth Profiling to Microelectronic Materials Processing, *Microelectronics Processing: Inorganic Materials Characterization*, (1986) 17.
- [15] J.F. Ziegler, J.P. Biersack, M.D. Ziegler, *The Stopping and Ranges of Ions in Matter*, 5 ed., SRIM Co., Chester, Maryland, 2008.
- [16] D.I. Thwaites, Bragg's Rule of Stopping Power Additivity: A Compilation and Summary of Results, *Radiation Research*, 95 (1983) 24.
- [17] G. Both, R. Krotz, K. Lohmer, W. Neuwirth, Density dependence of the stoping cross section measured in liquid ethane, *Pysical Review A*, 28 (1983) 5.
- [18] J.F. Ziegler, M.D. Ziegler, J.P. Biersack, SRIM - The Stopping and Ranges of Ions in Matter (2010), *Nuclear Instruments and Methods in Physics Research Section B*, 268 (2010) 6.
- [19] D. Engelkemeir, Improvements of Alpha-Particle Resolution of Silicon Surface-Barrier Detectors by Cooling, *Nuclear Instruments and Methods*, 48 (1967) 6.
- [20] J.A. Robinson, Design, Construction, and Characterization of a Prompt Gamma Activation Analysis Facility at the Oregon State University TRIGA® Reactor, in: *Nuclear Engineering*, Oregon State University, Corvallis, 2009, pp. 143.
- [21] S. Binney., Radiophysics Lectrue Notes, in, Oregon State University, 2006.
- [22] W. Audi, The AME2003 Atomic Mass Evaluation, *Nuclear Physics A*, (2003) 337-676.
- [23] J.A. Robinson, M.R. Hartman, S.R. Reese, Design, construction and characterization of a prompt gamma activation analysis facility at the Oregon State University TRIGA® Reactor *Journal of Radioanalytical and Nuclear Chemistry*, 283 (2009) 10.
- [24] Ortec, Introduction to Charged-Particle Detectors, in, Ortec, Oak Ridge TN, 2012.
- [25] Cremat, CR-150 Evaluation Board, in, Watertown, MA, 2012.

- [26] M.K. Schultz, R.M. Keyser, R.C. Trammell, D.L. Upp, Improvement of spectral resolution in the presence of periodic noise and microphonic's for hyper-pure germanium detector gamma-ray spectrometry using a new digital filter, *Journal of Radioanalytical and Nuclear Chemistry*, 271 (2007) 6.
- [27] H. Nyquist, Certain Factors Affecting Telegraph Speed, *Journal of the A. I. E. E* 43 (1924) 23.
- [28] National Instruments, Using a Digitizer for Time-Domain Measurements, in, National Instruments, Austin, Texas, 2009.
- [29] alazartech, in.
- [30] GaGe, Products - High Speed Digitizer, 16 Bit Family, in, 2012.
- [31] G.F. Knoll, Radiation Detection and Measurement, 3 ed., John Wiley & Sons, Inc., Haboken, NJ, 2000.
- [32] C. Canali, G. Majni, R. Minder, G. Ottaviani, Electron and Hole Drift Velocity Measurements in Silicon and Their Empirical Relation to Electric Field and Temperature, *IEEE Transactions on Electron Devices*, (1975) 3.
- [33] FEMTO, 100/200 MHz Wideband Voltage Amplifier Series DHPVA, in, 2012.
- [34] G.P. Nason, Wavelet Methods in Statistics in Statistics with R, Springer Science and Business Media, LLC, Baltimore, MD, 2008.
- [35] W.P. Reed, Certificate of Analysis 93a Reference Material, in: NIST (Ed.), Gaithersburg, MD, 1991.
- [36] v. Seggern, CRC Standard Curves and Surfaces with Mathematics, CRC Press, Boca Raton, FL, 2007.
- [37] J.F. Ziegler, PARTICLE INTERACTIONS WITH MATTER, in, 2012.
- [38] C. Industries, Passivated Implanted Planar Silicon (PIPS) Detectors, in, 2008.
- [39] L. Company, in, 2012.
- [40] Y. Li, M.E. Lacey, J.V. Sweedler, A.G. Webb, Spectral restoration from low signal-to-noise, distorted NMR signals: application to hyphenated capillary electrophoresis-NMR, *Journal of Magnetic Resonance*, 162 (2003) 8.
- [41] L. Campbell, A. Misner, E. Smith, S. Reese, J. Robinson, High Energy Delayed Gamma Spectroscopy for Plutonium Assay of Spent Fuel, IAEA-CN-184/128, (2010).